Master of Science Thesis

An Adjoint Approach to Error Estimation for Mimetic Spectral Element Method

Navid Hermidas

December 10, 2012

Aerodynamics

Faculty of Aerospace Engineering

TU Delft

Delft University of Technology

An Adjoint Approach to Error Estimation for Mimetic Spectral Element Method

Master of Science Thesis

For obtaining the degree of Master of Science in Aerospace Engineering
at Delft University of Technology

Navid Hermidas

December 10, 2012

Faculty of Aerospace Engineering · Delft University of Technology

Delft University of Technology

DELFT UNIVERSITY OF TECHNOLOGY
DEPARTMENT OF AERODYNAMICS

The undersigned hereby certify that they have read and recommend to the Faculty of Aerospace Engineering for acceptance the thesis entitled **"An Adjoint Approach to Error Estimation for Mimetic Spectral Element Method"** by **Navid Hermidas** in fulfillment of the requirements for the degree of **Master of Science**.

Dated: December 10, 2012

Supervisors:

Dr. ir. M.I. Gerritsma

Prof. dr. ir. drs. H. Bijl

Dr. S. J. Hulshoff

Ir. A. Palha

Preface

When in the January of 2012 I returned from my internship in Belgium I had already began searching for a M.Sc. thesis topic. After talking to a number of people, I was advised to talk to Dr. ir. M. I. Gerritsma. I had already had the pleasure of knowing Marc a bit and was familiar with his style of teaching from courses Aerodynamics B, Constitutive Modeling, and CFD1. Among these courses, the reading material for constitutive modeling had struck me the most, as a very intelligent way of looking at physical phenomena. I was therefore, keen to learn more about the subjects that he was working on. After our first meeting I learned that the same concepts that I had learned from Constitutive Modeling course can be used to solve differential equations very accurately. Therefore, I was all set to take on a challenge which would last almost a year.

The subject that was proposed was construction of an adjoint error estimator for mimetic spectral element methods. These methods make use of differential geometry and algebraic topology and explicitly recognize the existence of a dual grid in the numerical computations. A consequence of this approach is the existence of two different representations of a solution. My work was initially focused on investigating whether or not these two solutions can be used for accurate *a posteriori* error estimation. However, soon I realized that this approach presents some difficulties due to the rates at which the two solutions converged. Therefore, after some discussions with my supervisor, he suggested that I would look at the already established framework of adjoint error estimation for finite element methods and specifically, goal oriented error estimation. Since h/p refinement in mimetic framework had already been achieved by another Master's student, the motivation here was to construct an adjoint error estimator that can be used for adaptive refinement. This guided me to borrow some of the basic mathematical ideas from the finite element world in order to construct an error estimation tool.

This work would not have been possible without the guidance, support, and encouragement that I have received. Therefore, I would like to first thank my father who made me the person I am today. Secondly, I would like to thank my mother and brother, for their constant love and support. Special thanks goes to Dr. ir. M. I Gerritsma for being a true mentor and for introducing me to the mimetic world and allowing me to work on such an interesting topic. I would like to thank Ir. A. Palha for his invaluable guidance and contributions to my work. Finally, I would like to thank Prof. dr. ir. drs. Bijl and Dr. S. J. Hulshoff for their guidance and support throughout my studies here at TUDelft.

Abstract

Within the field of computational fluid dynamics (CFD), approximation of integral functionals such as lift and drag are of great importance. Following the advancements made in the area of adjoint error estimation for approximating these functionals, a new application of this approach for mimetic spectral element method will be investigated. Mimetic spectral element method provides a very clear description of where error can and can not be avoided and offers a good setting for adjoint error estimation. Following this approach, an adjoint p.d.e is constructed which is used to relate the local residual error in the flow solution to the global error in the functional of interest. This information on the quantity of error can then be used to set up an adaptive mesh refinement or to improve the accuracy of the approximated target functional. Numerical results will be investigated for Poisson equation in one and two dimensions. The range of applications of this theory exceeds beyond linear p.d.e's and includes nonlinear problems in multi-dimensional domains.

Table of Contents

List of Figures

List of Tables

Chapter 1

Introduction

Modeling of physical phenomenon has introduced partial differential equations (p.d.e.'s) into our everyday lives. Despite the great efforts that have been put in the past towards finding the analytical solutions of these mathematical models, in their complete form, many of these p.d.e.'s have stood the test of time. Yet, today more than ever before in the history, man is involved in the search for finding the exact solutions of these mathematical constructs. And as is the case in any battle, once a strategy fails, another must appear.
Since the advent of the computer, numerical analysis of physical phenomenon has developed quickly and on many fronts. Some of the prominent names in this arena are *finite difference*, *finite volume*, *finite element*, and very recently *mimetic* methods. A major defect which is inherent to numerical methods is the inseparable bond they possess with their numerical error. Therefore, great efforts have been made in the past towards reducing this error. To perform this task correctly and efficiently it is paramount to first understand the exact source of the error. Following such trails can sometimes lead to a deeper understanding of the physics itself which in turn can modify the way things are modeled. It can be argued that this has been the case for mimetic methods. Although, its conception might have been a result of a completely different story, its emergence will change the outlook of engineering world towards numerical approximation of physical phenomenon in the years to come.
The outstanding characteristic of mimetic methods is their capability in making a clear distinction between where error can and where it can not be avoided. A perfect example of such a distinction is the way operators such as **div**, **curl**, and **grad** from calculus are treated in this framework. The use of differential geometry, which is a major asset to this approach, has brought with it the realization that such operators are purely topological and as such can be performed exactly irrespective of the grid used. Due to the affinities of differential geometry with algebraic topology, the continuous framework of the former is paired here with the discrete world of the latter and this has brought about an easy transference of ideas between these two mathematical disciplines. A good example of this affinity is the homomorphism that exists between the exterior derivative from differential geometry and coboundary operator from algebraic topology.
When using mimetic methods, ideas are usually framed in the language of differential geom-

etry. The objects that are used here are known as differential forms which are coordinate independent maps that accept vectors and produce real numbers. To gain a better understanding of these mathematical tools, consider the temperature field in a room. Each point in the room can be associated with a unique coordinate. A zero-form would receive the coordinates of a point and produce a real number representing the temperature at that point in space and time. Note that temperature is a physical concept and is therefore independent of any coordinate system. Now, consider a displacement vector field in that same room. Again, note that a vector is independent of any coordinate systems. It can be stated in Cartesian or Polar coordinates. However, this does not change the fact that the same physical concept is being considered. Vectors can be thought of as tangents to a line or lines and are associated with one-forms. A one-form would receive a vector and produce a real number. This number could for example represent the magnitude of displacement in the direction of that vector. Now consider flux through a surface in the same room. Flux is a physical concept which is inseparable from a surface. A two-form receives two vectors and produces a real number. This number could for instance represent the flux which is associated with the surface that can be constructed by the two vectors. Finally, consider density in a volume in that room. The concept of density is inseparable from volumes. When one talks about the density he/she is always concerned with the mass inside a volume divided by that same volume. Therefore, it is meaningless to talk about density at a point. Consequently, when density of a volume in space is considered, the volume itself must not be forgotten. A three-form would receive three vectors, which can be used to construct the volume to which the density is being attributed, and produce a real number representing the density of that volume.
In this way, differential geometry accommodates for the preservation of the geometrical attributes of partial differential equations in a way that vector calculus can not. Moreover, when a relation from differential geometry has a natural counterpart in algebraic topology it can be performed exactly. From an industrial point of view this is very appealing and although, the results maybe astounding, the battle for the elimination of error due to discretization is far from over. This is because not all continuous relations from differential geometry have a natural discrete counterpart in algebraic topology.

1.1 Problem Statement

The error in numerical computations stems from different sources. One such error is due to discretization of the partial differential equations. If the focus of error estimation is on analyzing the asymptotic behavior of the discretization error, the approximated error is *a priori* error estimate. On the other hand, if the residual of the approximate solution and stability properties of the differential equation are used to derive an actual estimate for the error in the approximate solution, then the approximated error is *a posteriori* error estimate. The former method of error estimation can be performed prior to the computation of the discrete solution, while, the latter, due to its dependence on the approximate solution, can only be used after a discrete solution has been obtained. This work is concerned with the construction of *a posteriori* error estimates for mimetic spectral element methods.
In the field of finite element methods many different strategies have been developed over the years for estimating the error due to discretization. Moreover, considering the close connection

between the mimetic and the finite element methods and following the recent advancements on the confluence of these two fields, it is now possible to incorporate some of these strategies into the field of mimetic methods. Furthermore, due to their reliability and high accuracy, this work is concentrated on *dual weighted residual* (DWR) error estimators. This strategy has been used in many different contexts in the past for deriving error bounds for linear output functionals. Since, many quantities of interest such as lift and drag are described in terms of linear functionals, this approach to error estimation has found considerable popularity in the engineering community. Moreover, the information from such error estimators are often used to steer an adaptive mesh refinement. This in turn can be used to minimize the cost of reaching a given accuracy or to produce the most accurate solution for a given cost. More on the history of error estimation and the place of dual weighted residual error estimation in this context will be covered in chapter 4.
In the next section the structure of the current work is explained.

1.2 Thesis Outline

The current work is structure as follows: Chapter 2 is dedicated to the introduction of a set of mathematical tools from differential geometry and algebraic topology. The aim here is to familiarize the reader with the concepts which will be used extensively in the proceeding chapters. Chapter 3 introduces the basis functions which are used for reconstructing differential forms and explains the quadratures used in performing integration. Chapter 4 covers a brief history of adjoint error estimation followed by an introduction to the state of the art techniques in the field of error estimation. It then focuses on the construction of a dual weighted residual error estimator for mimetic spectral element methods. Poisson problem in standard variational form and mixed form is chosen as the sample problem and a multitude of examples in 1 and 2D are presented. Chapter 5, deals with post-processing of linear functionals using the information obtained from adjoint error estimation. It will be shown that faster convergence rates can be achieved for specific quantities of interest. Finally, chapter 6 contains some concluding remarks and recommendations for future research on this topic.

Chapter 2

Differential Geometry and Algebraic Topology

Differential geometry and algebraic topology are the mathematical disciplines that will be used throughout the course of this thesis. Hence, it is beneficial if not mandatory to introduce the reader to the building blocks of the work which will follow. To this end, this chapter is devoted to a review of the mathematical objects and operations that are taken from differential geometry, and its discrete counterpart algebraic topology.

2.1 Differential Geometry

Differential geometry is a part of geometry which is concerned with geometrical constructions that live on smooth (differentiable) manifolds. These constructions, which in three dimensional space constitute points, curves, surfaces, and volumes, are investigated by means of differential and integral calculus.
Within differential geometry two branches are identifiable: Local Differential Geometry, and Global Differential Geometry. The former is concerned with the study of geometrical objects in the neighborhood of a point while the latter deals with the study of these objects as a whole. For the purposes of the current work Local Differential Geometry is considered.
In this section, initially, differential forms and their corresponding spaces are introduced. This paves the way for the introduction of some concepts from exterior algebra, namely, exterior derivative, generalized Stokes' theorem, the Hodge-$\star$ operator, and finally mapping operators.

2.1.1 Exterior Differential Forms

Within Differential Geometry the most elementary building blocks are objects known as *exterior differential forms*. According to Flanders [1], exterior p-forms are things which live under integral signs and can be integrated over p-dimensional objects. In three dimensional space four types of differential forms can be identified. These are: zero-forms, one-forms, two-forms, and finally three-forms.
A zero-form is a scalar valued function and is associated with integration over points $\mathcal{P}$. In $\mathbb{R}^3$ a zero-form can be written as:

$$\phi^0 = f(x, y, z), \tag{2.1}$$

where superscript 0 indicates that ϕ is a zero-form. An example of a zero-form is the velocity potential function which accepts coordinates and returns a point value. Integration of ϕ^0 can be viewed as a duality pairing between ϕ^0 and the points $\mathcal{P}$ in the following way:

$$\langle \phi^0, \mathcal{P} \rangle := \phi^0(\mathcal{P}). \tag{2.2}$$

The line integral along a smooth curve $\mathcal{D}$ in $\mathbb{R}^3$ can be written as:

$$\int_{\mathcal{D}} A(x, y, z)dx + B(x, y, z)dy + C(x, y, z)dz, \tag{2.3}$$

where the one-form under integral sign is:

$$\omega^1 = A(x, y, z)dx + B(x, y, z)dy + C(x, y, z)dz. \tag{2.4}$$

The superscript 1 indicates that ω is a one-form. An example of a one-form is the force function, which when integrated along a line results in the amount of work performed. A 1-form is a linear functional which lives in the covector field and is connected to its corresponding tangent linear vector space via inner product operation. An unnatural one to one correspondence between the two spaces can be recognized as follows:

$$\omega^1 = A(x, y, z)dx + B(x, y, z)dy + C(x, y, z)dz \longrightarrow \boldsymbol{\omega} = A^x e_x + B^x e_y + C^x e_z, \tag{2.5}$$

where subscripts and superscripts x,y, and z have been adopted from tensor algebra to indicate an association with the tangential space. Coefficients A^x, B^y, and C^z are known as the vector proxies of ω^1 and dx, dy, and dz are the basis vectors that associate these coefficients with one dimensional objects or lines [1]. Integration of ω^1 introduces a duality pairing between ω^1 and the curve $\mathcal{D}$ in the following way [2, 3]:

$$\langle \omega^1, \mathcal{D} \rangle := \int_{\mathcal{D}} A(x,y,z)dx + B(x,y,z)dy + C(x,y,z)dz. \tag{2.6}$$

In $\mathbb{R}^3$ a surface integral over surface $\mathcal{S}$ can be written as:

$$\iint_{\mathcal{S}} P(x,y,z)dydz + Q(x,y,z)dzdx + R(x,y,z)dxdy. \tag{2.7}$$

Hence, the resulting two-form under the integral sign is:

$$\alpha^2 = P(x,y,z)dydz + Q(x,y,z)dzdx + R(x,y,z)dxdy, \tag{2.8}$$

where, again superscript 2 indicates that α is a two-form. An example of a two-form is a function describing flux through a surface or rotation within a surface. Once again, coefficients $P(x,y,z)$, $Q(x,y,z)$, and $R(x,y,z)$ constitute the vector proxies of α^2 and $dydz$,$dzdx$, and $dxdy$ are the basis vectors that associate these coefficients with two dimensional objects or surfaces. Similar to the case of a one-form, an unnatural isomorphism between a two-form and its counterpart in the primal[2] space can be recognized as follows:

$$\alpha^2 = P(x,y,z)dydz + Q(x,y,z)dzdx + R(x,y,z)dxdy \longrightarrow \boldsymbol{\alpha} = P^x e_x + Q^x e_y + R^x e_z. \tag{2.9}$$

From (2.5) and (2.9) it can be seen that in $\mathbb{R}^3$ one-forms and two-forms are both in one to one correspondance with vectors in the tangent space. From elementary algebra it is known that a surface area can be represented by a vector whose magnitude is equal to the area and whose direction is perpendicular to the surface. This form of association obscures the difference between physical quantities which live on surfaces and those which live on lines. Therefore, one of the advantages of introducing differential forms is that this form of ambiguity is rectified.

[1] It is worth mentioning that although in Euclidean basis the coefficients of vectors are the same as those of one/two-forms, in general this depends on the basis and the metric and is not always the case.

[2] The primal space is the tangent space to $\mathcal{S}$. The corresponding dual space is the space of all differential forms.

Again integration of α^2 introduces a duality pairing between α^2 and the surface $\mathcal{S}$ in the following way:

$$\langle \alpha^2, \mathcal{S} \rangle := \int_{\mathcal{S}} P(x,y,z)dydz + Q(x,y,z)dzdx + R(x,y,z)dxdy. \tag{2.10}$$

A volume integral in $\mathbb{R}^3$ over volume $\mathcal{V}$ has the form:

$$\iiint_{\mathcal{V}} g(x,y,z)dxdydz. \tag{2.11}$$

Hence, the resulting three-form is:

$$\gamma^3 = g(x,y,z)dxdydz. \tag{2.12}$$

Superscript 3 indicates that γ is a three-form. An example of a three-form is a function which describes the density of a fluid within a volume. Therefore, it can be understood that three-forms like zero-forms are described by scalar fields. However, their geometrical characteristics are different (one lives on points while the other in volumes). $dxdydz$ is known as the volume form and associates the scalar $g(x,y,z)$ with volumes. Again integral of γ^3 introduces a duality pairing between γ^3 and the volume $\mathcal{V}$ in the following way:

$$\langle \gamma^3, \mathcal{V} \rangle := \int_{\mathcal{V}} g(x,y,z)dxdydz. \tag{2.13}$$

2.1.2 Space of p-Forms and Exterior (Wedge) Product

Let Ω be a 2-manifold whose coordinate patches $(\mathcal{U}, \phi_u)$ are homeomorphic to open sets in $\mathbb{R}^2$, where, $\phi_u : \mathcal{U} \to \mathbb{R}^2$, see Figure 2.1.

The surface integral on this manifold can be written as:

$$\iint_{\mathcal{U}} A(x,y)dxdy = \iint_{\phi_u^{-1}(\mathcal{U})} A(x(u,v), y(u,v)) \left| \begin{array}{cc} \frac{\partial x}{\partial u} & \frac{\partial x}{\partial v} \\ \frac{\partial y}{\partial u} & \frac{\partial y}{\partial v} \end{array} \right| dudv, \tag{2.14}$$

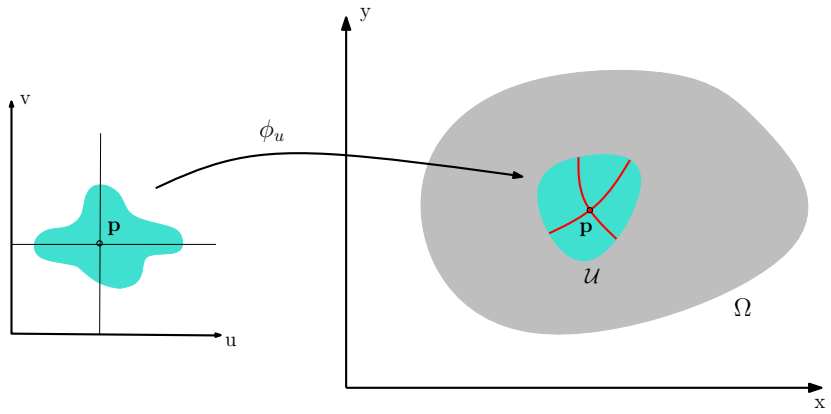

Figure 2.1: Depiction of a 2-manifold Ω.

where, $|\ .\ |$ denotes the Jacobian of the matrix. From the Jacobian it can be understood that if $dy = dx$ the differential form under the integral disappears. Moreover, if the order of $dxdy$ is reversed the Jacobian changes sign. Therefore, in order to construct a multiplication relation for differential forms the following rules are justified [1]:

$$dxdx = 0, \tag{2.15}$$

$$dxdy = -dydx. \tag{2.16}$$

This new multiplication is known as the *wedge*, " $\wedge$ ", product and allows for the construction of high degree differential forms from lower degree ones. From (2.16) it is obvious that the wedge product is skew symmetric. The calculus of differential forms is endowed with the following structure for the wedge product [4]:

$$(a^p \wedge b^l) \wedge c^m = a^p \wedge (b^l \wedge c^m), \qquad \text{(Associativity)} \tag{2.17}$$

$$\begin{aligned} (\alpha a^p + \beta b^l) \wedge (\gamma c^m + \delta d^n) \quad &= \quad \text{(Multilinearity)} \\ \alpha\gamma(a^p \wedge c^m) + \alpha\delta(a^p \wedge d^n) \quad &+ \quad \beta\gamma(b^l \wedge c^m) + \beta\delta(b^l \wedge d^n), \end{aligned} \tag{2.18}$$

$$(a^p \wedge b^l) = (-1)^{pl}(b^l \wedge a^p), \qquad \text{(Skew symmetry)} \tag{2.19}$$

where α, β, γ, and δ are real numbers and a^p, b^l, c^m, and d^n are differential forms of degrees p, l, m, and n respectively.
(2.19) and the fact that on an n-manifold, Ω, p-forms with $p > n$ are bound to be trivial, one has:

$$a^p \wedge a^p = 0, \qquad \forall a^p \in \Lambda^p(\Omega), \quad p \text{ is odd or } p > \left(\frac{n}{2}\right), \tag{2.20}$$

where $\Lambda^p(\Omega)$ is the space of all p-forms on Ω.
From the reduction rules mentioned, it can be concluded that the dimension of the space of p-forms in an n-dimensional vector space is determined by the number of p-combinations of the universal set. Therefore, in $\mathbb{R}^3$, zero-forms and three-forms both constitute one dimensional linear vector spaces while one-forms and two-forms constitute three dimensional linear vector spaces.
The wedge product of a p-form and an l-form results in a (p+l)-form:

$$a^p \in \Lambda^p(\Omega), \;\; b^l \in \Lambda^l(\Omega) \qquad \rightarrow \qquad (a^p \wedge b^l) \in \Lambda^{p+l}(\Omega). \tag{2.21}$$

Following the rules mentioned thus far, wedge product of two one-forms in $\mathbb{R}^3$ can be written as:

$$a^1 \wedge b^1 = (a_y b_z - a_z b_y) dy \wedge dz + (a_z b_x - a_x b_z) dz \wedge dx + (a_x b_y - a_y b_x) dx \wedge dy. \tag{2.22}$$

Note that in $\mathbb{R}^3$, the vector proxies of the resulting two-form can be obtained by performing a cross product of the vector proxies of the initial one-forms as follows:

$$\begin{pmatrix} e_x & e_y & e_z \\ a^x & a^y & a^z \\ b^x & b^y & b^z \end{pmatrix} = (a^y b^z - a^z b^y) e_x + (a^z b^x - a^x b^z) e_y + (a^x b^y - a^y b^x) e_z, \tag{2.23}$$

where the coefficients of the two-vector in (2.23) coincide with those of the two-form in (2.22).
In the same vein, the wedge product of a one-form and a two-form yields:

$$a^1 \wedge c^2 = (a_x c_x + a_y c_y + a_z c_z) dx \wedge dy \wedge dz, \tag{2.24}$$

corresponding to the inner product in vector algebra.

2.1.3 Exterior Derivative

In the same manner that the wedge product in differential geometry generalizes multiplication operations such as cross product and inner product in vector algebra, a new operation known as *exterior derivative*, "d", can be viewed as the generalization of **grad**, **curl**, and **div**. When subjected to the exterior derivative, a p-form is transformed into a (p+1)-form. Exterior derivative is determined by the following rules [1]:

$$\mathrm{d}(a^p + b^l) = \mathrm{d}a^p + \mathrm{d}b^l, \tag{2.25}$$

$$\mathrm{d}\mathrm{d}a^p = 0 \qquad \forall a^p \in \Lambda^p(\Omega), \tag{2.26}$$

$$\mathrm{d}(a^p \wedge b^l) = \mathrm{d}a^p \wedge b^l + (-1)^p a^p \wedge \mathrm{d}b^l, \tag{2.27}$$

$$\mathrm{d}a^0 = \sum_i \frac{\partial a}{\partial x^i} dx^i. \tag{2.28}$$

As will be explained in the next subsection, the exterior derivative can be viewed as the formal adjoint of boundary operator, therefore, (2.26) states that boundary of a boundary is zero. This is a result of the assumption made in the derivation of Stokes' theorem, namely, that the boundary of the region of integration is closed. From (2.26) it can be seen that every exact p-form is closed. However, not every closed p-form is exact (Poincaré Lemma). (2.26) states the equality of mixed second partial derivatives which in terms of vector proxies in $\mathbb{R}^3$ reduces to [2]:

$$\textbf{curl grad} \equiv 0, \tag{2.29}$$

$$\textbf{div curl} \equiv 0. \tag{2.30}$$

As will be shown in the remainder of this section, the action of the exterior derivative on a p-form can result in a (p+1)-form. A one-form obtained in this way is bound to be a conservative field in the sense that its integral value between two points will be independent

of the path traveled. This is also carried over to surface and volume integrals where instead of the initial and the final points, the boundary of the domain is considered.
The exterior derivative of the zero-form introduced in 2.1.1 can be written as:

$$\mathrm{d}\phi^0 = \frac{\partial \phi}{\partial x}\mathrm{d}x + \frac{\partial \phi}{\partial y}\mathrm{d}y + \frac{\partial \phi}{\partial z}\mathrm{d}z, \tag{2.31}$$

whose vector proxy is equal to **grad** $\boldsymbol{\phi}$.
For the one-form in (2.1.1) one has:

$$\mathrm{d}\omega^1 = \left(\frac{\partial C}{\partial y} - \frac{\partial B}{\partial z}\right) dydz + \left(\frac{\partial A}{\partial z} - \frac{\partial C}{\partial x}\right) dzdx + \left(\frac{\partial B}{\partial x} - \frac{\partial A}{\partial y}\right) dxdy, \tag{2.32}$$

whose vector proxy is equal to **curl** $\boldsymbol{\omega}$.
The exterior derivative of the two-form introduced in 2.1.1 can be written as:

$$\mathrm{d}\alpha^2 = \left(\frac{\partial P}{\partial x} + \frac{\partial Q}{\partial y} + \frac{\partial R}{\partial z}\right) dxdydz, \tag{2.33}$$

whose vector proxy is equal to **div** $\boldsymbol{\alpha}$.
From (2.19) it is obvious that in $\mathbb{R}^3$:

$$\mathrm{d}\gamma^3 = 0. \tag{2.34}$$

In the light of what has been explained thus far for the exterior derivative of differential forms in $\mathbb{R}^3$, the following exact sequence holds:

$$\mathbb{R} \longrightarrow \Lambda^0(\Omega) \xrightarrow{\mathrm{d}} \Lambda^1(\Omega) \xrightarrow{\mathrm{d}} \Lambda^2(\Omega) \xrightarrow{\mathrm{d}} \Lambda^3(\Omega) \xrightarrow{\mathrm{d}} 0. \tag{2.35}$$

This is known as the De Rham sequence.

2.1.4 Generalized Stokes Theorem

From vector calculus the following results are known for integration of a quantity over different geometrical objects:

$$\int_{\mathcal{D}} \nabla f \cdot dr = f(r(a)) - f(r(b)), \tag{2.36}$$

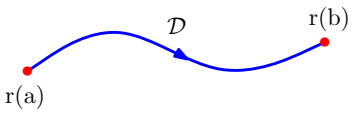

$$\iint_{\mathcal{S}} \mathbf{curl}\ F \cdot dS = \int_{\mathcal{D}} F \cdot dr, \tag{2.37}$$

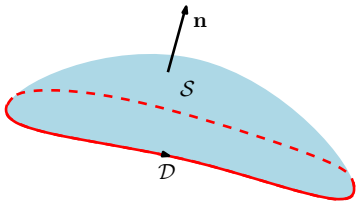

$$\iiint_{\mathcal{V}} \mathbf{div}\ F \cdot dV = \int_{\mathcal{S}} F \cdot dS. \tag{2.38}$$

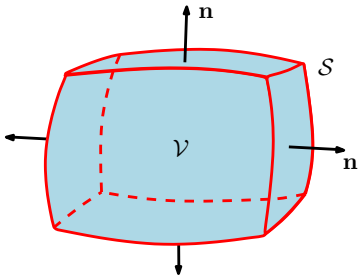

From (2.36), (2.37), and (2.38) it can be seen that **grad**, **curl**, and **div** take quantities that are defined on points, lines, and surfaces and map them onto lines, surfaces, and volumes. Hence, the following exact sequence can be established:

$$\mathbb{R} \longrightarrow H_P \xrightarrow{\mathbf{grad}} H_L \xrightarrow{\mathbf{curl}} H_S \xrightarrow{\mathbf{div}} H_V. \tag{2.39}$$

This sequence is known as the De Rham complex and is equivalant to (2.35).
In the previous section the concept of exterior derivative was reviewed and it became clear that depending on the degree of the differential form it is operating on, the exterior derivative can play the role of **grad**, **curl**, and **div** in $\mathbb{R}^3$. This revelation allows for the introduction of a new theorem which not only encompasses (2.36), (2.37), and (2.38), it generalizes this concept for higher dimensions. This new theorem is known as the *generalized Stokes' theorem* and for a p-form, η^p, on a (p+1)-manifold, Ω, reads:

$$\int_{\Omega} \mathrm{d}\eta^p = \int_{\partial\Omega} \eta^p. \tag{2.40}$$

For $p = 0$, 1 and 2, (2.40) reduces to the familiar **grad**, **curl**, and **div** integral theorems. Moreover, from (2.40), the boundary operator ∂ can be viewed as the formal adjoint of the exterior derivative and vice versa. This indicates that the exterior derivative is closely connected to the topology.

2.1.5 Hodge-$\star$ Operator

Looking at the De Rahm sequence (2.35) it can be seen that only a one way exact transformation from left to right is possible. Moreover, due to (2.26) it is not possible to apply the exterior derivative twice to a zero-form to obtain a three-form as is often required in physical problems. One important operator whose construction suffers from this short coming is the Laplace operator. This motivates the introduction of a new linear operator that can be used to circumvent these problems. This operator is known as the *Hodge-$\star$* operator. The Hodge-$\star$ operator takes a p-form from the primal space and to its contravariant version associates a (n-p)-form from the dual space [3]. Perhaps one way of recognizong the existance of such an operator is through comparing the dimensions of differential forms. From left to right in the De Rahm sequence it can be seen that a zero-form and a three-form are both one dimensional, while a one-form and a two-form are both three dimensional. This suggests that a dual space with a different orientation can be associated to the primal space in the following way:

$$\begin{array}{ccccccccccc} \mathbb{R} & \longrightarrow & \Lambda^0(\Omega) & \xrightarrow{\mathrm{d}} & \Lambda^1(\Omega) & \xrightarrow{\mathrm{d}} & \Lambda^2(\Omega) & \xrightarrow{\mathrm{d}} & \Lambda^3(\Omega) & \xrightarrow{\mathrm{d}} & 0 \\ & & \updownarrow\star & & \updownarrow\star & & \updownarrow\star & & \updownarrow\star & & \\ 0 & \longleftarrow & \Lambda^3(\Omega) & \xleftarrow{\mathrm{d}} & \Lambda^2(\Omega) & \xleftarrow{\mathrm{d}} & \Lambda^1(\Omega) & \xleftarrow{\mathrm{d}} & \Lambda^0(\Omega) & \longleftarrow & \mathbb{R}. \end{array} \tag{2.41}$$

Note that the connection between the two sequences is realized by the Hodge-$\star$ operator. In a way, the Hodge-$\star$ operator can be viewed as the embodiment of the fact that every geometrical object possesses two types of orientations: an inner orientation, and an outer orientation. The former is independent of the dimension of the ambient space, while the latter is determined by the dimension and orientation of the ambient space, see [5].
The Hodge-$\star$ operator is determined by:

$$a^p \wedge \star b^p = \langle a^p, b^p \rangle \omega^n, \tag{2.42}$$

where, $\langle . \rangle$ is the pointwise inner product, a^p and b^p are differential forms of degree p, and ω^n is the volume form. For a more thourough explanation of the derivation of this relation see appendix A.
From (2.41) it can be seen that the Hodge-$\star$ operator can be used to construct a constitutive equation. It allows for a change between different geometrical objects while keeping the scalar or vector fields that are defined on these objects unaffected [2].
In $\mathbb{R}^3$, the action of this operator on a one-form can be written as:

$$a^1 = a_x dx + a_y dy + a_z dz \quad \Longrightarrow \quad \star a^1 = a_x \star dx + a_y \star dy + a_z \star dz \quad \Longrightarrow \quad \star a^1 = a_x dydz + a_y dzdx + a_z dxdy. \tag{2.43}$$

Note that the Hodge-$\star$ operator is linear.
Applying the hodge operator twice yields:

$$\star \star a^p = (-1)^{p(n-p)}\, a^p. \tag{2.44}$$

Using the Hodge-$\star$ operator, the formal Hilbert adjoint of the exterior derivative known as the codifferential operator, $\mathrm{d}^\star$, is defined as [4]:

$$\left(\mathrm{d}a^{p-1}, b^p\right) = \left(a^{p-1}, \mathrm{d}^\star b^p\right) \quad \text{where,} \quad \mathrm{d}^\star b^p := (-1)^{n(p+1)+1} \star \mathrm{d} \star b^p \quad \forall\, b^p \in \Lambda^p(\Omega). \tag{2.45}$$

In terms of the exterior derivative and the codifferential operator the self-adjoint Laplace operator becomes:

$$-\Delta a^p := \left(\mathrm{d}^\star \mathrm{d} + \mathrm{d}\mathrm{d}^\star\right) a^p \quad , \quad \forall\, a^p \in \Lambda^p(\Omega). \tag{2.46}$$

Some of the most important relations concerning the Hodge-$\star$ operator are listed in appendix B.
To end this section it is necessary to mention that unlike all the operations explained thus far, the Hodge-$\star$ operator lacks a discrete counterpart in algebraic topology and is not metric free. Hence, in problems such as Poisson, all the numerical approximations can be attributed to the discretization of this operator. The rest of the operations can be performed in an exact manner. This characteristic is inherent to constitutive models [2].

2.1.6 Mappings

In performing numerical computations the domain of the problem is most often a curved setting (e.g. flow around an airfoil). Therefore, in order to move back and forth between the reference and the physical domains different mappings are necessary. In differential geometry

this mapping is performed by using an operator called the *pullback*. Since differential forms are objects that live under integral signs, the operation of the pullback is defined by a change of variables.
Let Φ be a map sending the reference domain, a p-manifold $\mathcal{M}_{ref}$, to the physical domain, a p-manifolad $\mathcal{N}$, $\Phi : \mathcal{M}_{ref} \to \mathcal{N}$. Moreover, let a^p be a differential form in the physical domain. Then,

$$\int_{\Phi(\mathcal{M}_{ref})} a^p = \int_{\mathcal{M}_{ref}} \Phi^*(a^p). \tag{2.47}$$

Φ^* is a linear transformation called the pullback operator which brings a^p to the reference domain, $\Phi^* : \Lambda^p(\mathcal{N}) \to \Lambda^p(\mathcal{M}_{ref})$.
The pullback operator commutes with the wedge product and exterior derivative:

$$(\Phi^* a^p \wedge \Phi^* b^l) = \Phi^*(a^p \wedge b^l). \tag{2.48}$$

$$\Phi^*(\mathrm{d}a^p) = \mathrm{d}(\Phi^* a^p). \tag{2.49}$$

(2.48) and (2.49) confirm that the wedge product and the exterior derivative are metric free operators [2].
Let $\Phi : \partial\mathcal{N} \to \mathcal{N}$, then its pullback is known as the *trace operator* and is defined as: $\mathrm{tr} : \Lambda^p(\mathcal{N}) \to \Lambda^p(\partial\mathcal{N})$.

2.2 Algebraic Topology

Algebraic topology is a mathematical discipline that is concerned with connectedness of geometrical objects (topological spaces). Hence, the main focus here is classifying the objects according to the degree that they are connected. Since, stretching or shrinking an object has no effect on the nature of its connectedness, any mathematical concept that has a topological basis is metric free.
The notions of exactness and closedness of differential forms are the main themes that introduce the current work into the realm of algebraic topology. Here, manifolds are discretized into a finite collection of subspaces which in $\mathbb{R}^3$ are composed of points, lines, surfaces, and volumes. As will be shown in this section it is possible to assign values to these subspace elements and perform operations. Therefore, in this sense algebraic topology can be viewed as the discrete counterpart of differential geometry.
In this section first discretization of a manifold into cells is explained. Next, attribution of values to these cells is treated and the concept of the coboundary operator is explained. For a more in depth treatment of this subject the reader is referred to [6, 7, 8].

2.2.1 Cells, Chains, and Cell Complex

In algebraic topology points or zero dimensional objects are referred to as *zero-cells*. Since, the notion of a metric does not exist here, the position of these points or their distance from each other is irrelevant, what matters is how they are connected to each other.
Consider a compact manifold, a finite number of zero-cells will be associated to this manifold. The formal sum of these zero-cells, called a *zero-chain*, can be written as,

$$P_0 = \sum_{i=1}^{n_p} m_{0,i}\, p_{0,i}, \tag{2.50}$$

where, P_0 is a zero-chain, $p_{0,i}$ a zero-cell, and $m_{0,i}$ is the weight of the zero-cell.
Lines that will be associated to a compact manifold are known as *one-cells*. Similar to a zero-chain, a one-chain is a formal sum of one-cells (or edges). A one-chain can be written as:

$$L_1 = \sum_{i=1}^{n_l} m_{1,i}\, l_{1,i}. \tag{2.51}$$

where, L_1 is a one-chain, $l_{1,i}$ a one-cell, and $m_{1,i}$ is the weight of the one-cell. A one-chain with a boundary is bounded by a zero-chain[3] .
Surfaces that will be associated to a compact manifold are known as *two-cells*. A two-chain is a collection of two-cells and can be written as.

$$S_2 = \sum_{i=1}^{n_s} m_{2,i}\, s_{2,i}. \tag{2.52}$$

where, S_2 is a two-chain, $s_{2,i}$ a two-cell, and $m_{2,i}$ is the weight of the two-cell. A two-chain with a boundary is bounded by a one-chain.
In this work for a p-cell that belongs to a specific chain and whose orientation agrees with a chosen orientation, $m_{p,i} = 1$. For a p-cell that does not belong to a chain $m_{p,i} = 0$. And finally, for a p-cell that belongs to a specific chain but whose orientation is reversed with respect to a chosen orientation, $m_{p,i} = -1$.
A collection of bounded cells is known as a cell-complex. Figure 2.2 depicts a cell complex with bounded cells.

Following the discussion in 2.1.5 each cell possesses two orientations: an inner orientation, and an outter orientation. Figure 2.3 depicts these two orientations in $\mathbb{R}^2$. Note that an

[3]Boundary of a zero-chain is empty.

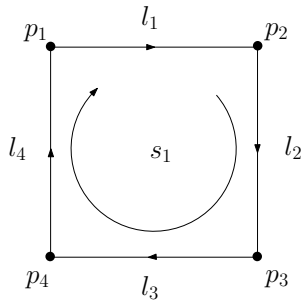

Figure 2.2: Cell complex.

internal orientation of a zero-cell is equivalent to the external orientation of a two-cell and vice versa.

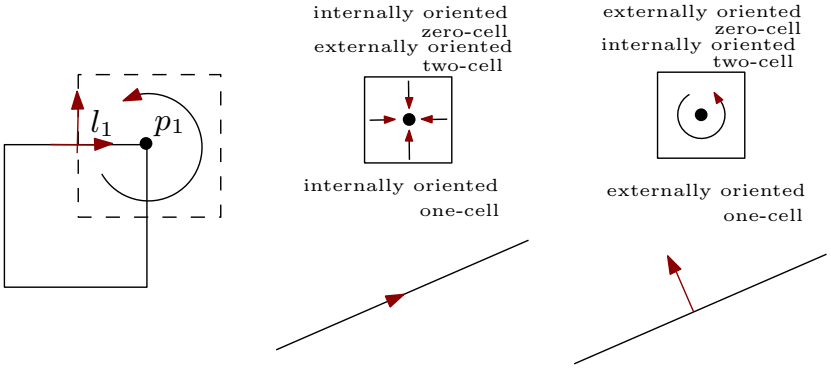

Figure 2.3: Internal and external orientations in $\mathbb{R}^2$.

Moreover, boundary of a p-chain is a (p-1)-chain and the discrete operator which receives a p-chain and returns its boundary chain is known as the boundary operator, ∂. Its action on a p-chain can be written as:

$$\partial C_p = \partial \left(\sum_{i=1}^{n_p} m_{p,i}\, c_{p,i} \right) = \sum_{i=1}^{n_p} m_{p,i}\, \partial c_{p,i}. \tag{2.53}$$

According to the rules mentioned for the weights of a p-chain the action of the boundary operator on the one-cells from Figure 2.2 can be written as:

$$\begin{aligned} \partial l_1 &= p_2 - p_1, \\ \partial l_2 &= p_3 - p_2, \\ \partial l_3 &= p_4 - p_3, \\ \partial l_4 &= p_1 - p_4. \end{aligned} \tag{2.54}$$

This can in turn be expressed in the following matrix format:

$$\partial L = \partial \begin{pmatrix} l_1 \\ l_2 \\ l_3 \\ l_4 \end{pmatrix} = \begin{pmatrix} -1 & 1 & 0 & 0 \\ 0 & -1 & 1 & 0 \\ 0 & 0 & -1 & 1 \\ 1 & 0 & 0 & -1 \end{pmatrix} \begin{pmatrix} p_1 \\ p_2 \\ p_3 \\ p_4 \end{pmatrix}. \tag{2.55}$$

The matrix on the right hand side of (2.55) is called an *incidence matrix* and is denoted by $\mathbb{E}^{1,0}$. The superscripts 1 and 0 indicate that boundary of a one-chain is being expressed in terms of a zero-chain through the incidence matrix.
Similarly, the relation between the boundary of the two-chain in Figure 2.2 and the one-chain containing all the one-cells can be written as:

$$\partial S = \begin{pmatrix} 1 & 1 & 1 & 1 \end{pmatrix} \begin{pmatrix} l_1 \\ l_2 \\ l_3 \\ l_4 \end{pmatrix}, \tag{2.56}$$

where the incidence matrix on the right hand side is denoted by $\mathbb{E}^{2,1}$. Now applying the boundary operator twice to this two-chain yields:

$$\partial\partial S = \begin{pmatrix} 1 & 1 & 1 & 1 \end{pmatrix} \begin{pmatrix} -1 & 1 & 0 & 0 \\ 0 & -1 & 1 & 0 \\ 0 & 0 & -1 & 1 \\ 1 & 0 & 0 & -1 \end{pmatrix} \begin{pmatrix} p_1 \\ p_2 \\ p_3 \\ p_4 \end{pmatrix} = 0. \tag{2.57}$$

This result is a reiteration of the previously established conclusion, namely, that the boundary of the boundary of a closed p-chain is always zero.
Using the boundary operator, the following sequence can be constructed in $\mathbb{R}^2$:

$$0 \longrightarrow C_2 \xrightarrow{\partial} C_1 \xrightarrow{\partial} C_0 \longrightarrow 0, \tag{2.58}$$

where C_2, C_1, and C_0 are the sets of all ordered points, edges, and surfaces in the cell complex [2].

2.2.2 Cochains and coboundary operator

The cell-complex introduced in 2.2.1 provides the setting in which the mathematical operations can be performed. It is the discrete analogue of a manifold. In order to perform different operations it is necessary to introduce also the discrete counterparts of differential forms. These are known as *p-cochains* and can be thought of as functions that assign to each p-cell a number. The connection between cochains and differential forms is established through integration. Moreover, just as integration of differential forms over manifolds is a duality pairing, in a discrete setting, summation of cochains over chains is a duality paring of cochains and chains.
Let c_i^p be the operator which assigns 1 to the p-cell $c_{p,i}$ and 0 to $c_{p,j}$, where $i \neq j$, then,

$$C^p = \sum_{i=1}^{n_p} a_i^p \; c_i^p. \tag{2.59}$$

is a p-cochain. From (2.59) it can be seen that similar to a p-cell, a p-cochain can be written as a formal sum. Furthermore, the duality pairing of p-cochains and p-chains can be written as:

$$\langle C^p, C_p \rangle = \sum_{i=1}^{n_p} \sum_{j=1}^{n_p} a_i^p m_{p,j} \; \langle c_i^p, c_{p,j} \rangle = \sum_{i=1}^{n_p} a_i^p m_{p,i}, \tag{2.60}$$

where in the last step $\langle c_i^p, c_{p,j} \rangle = \delta_{ij}$ was used.
The role of the exterior derivative in a discrete setting is played by a new operator known as the *coboundary operator*, δ. Similar to the exterior derivative, this operator is the formal adjoint of the boundary operator [2, 9]:

$$\langle \delta C^p, C_{p+1} \rangle := \langle C^p, \partial C_{p+1} \rangle. \tag{2.61}$$

And from (2.57) and (2.61) it is clear that:

$$\langle \delta\delta C^p, C_{p+1} \rangle = \langle C^p, \partial\partial C_{p+1} \rangle = 0. \tag{2.62}$$

Therefore,

$$\delta\delta C^p = 0. \tag{2.63}$$

The coboundary operator maps p-cochains to (p+1)-cochains. Therefore, when applied to zero-, one-, or two-cochains it plays the roles of discrete gradient, discrete curl, and discrete diveregence. Using the coboundary operator the following De Rham complex can be set up in $\mathbb{R}^2$:

$$\mathbb{R} \longrightarrow C^0(K) \xrightarrow{\delta} C^1(K) \xrightarrow{\delta} C^2(K) \xrightarrow{\delta} 0, \tag{2.64}$$

where $C^p(K)$ is the space of all p-cochains on the cell complex K.
In order to construct the dual of this sequence it is necessary to first set up a new cell complex called the *dual cell complex*. Figure 2.4 shows the primal cell complex from Figure 2.2 in grey and the dual cell complex in black in $\mathbb{R}^2$. The zero-cells from the primal cell complex are associated with the two-cells from the dual cell complex. The primal one-cells are associated with the dual one-cells. And finally the primal two-cells are associated with the dual zero-cells. The cells from the dual cell complex are labeled with $\tilde{}$.

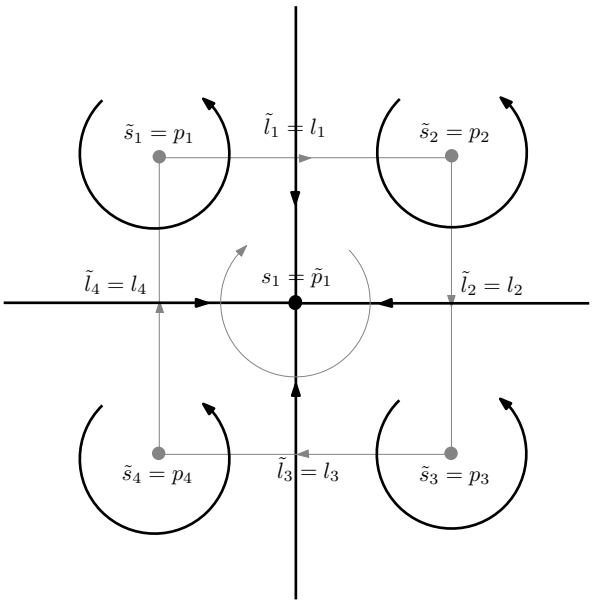

Figure 2.4: Primal cell complex in grey and dual cell complex in black.

The incidence matrices from the primal cell complex are:

$$\mathbb{E}^{1,0} = \begin{pmatrix} -1 & 1 & 0 & 0 \\ 0 & -1 & 1 & 0 \\ 0 & 0 & -1 & 1 \\ 1 & 0 & 0 & -1 \end{pmatrix}, \qquad \mathbb{E}^{2,1} = \begin{pmatrix} 1 & 1 & 1 & 1 \end{pmatrix}. \tag{2.65}$$

Similarly, the incidence matrices from the dual cell complex can be written as:

$$\mathbb{F}^{1,0} = \begin{pmatrix} 1 \\ 1 \\ 1 \\ 1 \end{pmatrix}, \qquad \mathbb{F}^{2,1} = \begin{pmatrix} -1 & 0 & 0 & 1 \\ 1 & -1 & 0 & 0 \\ 0 & 1 & -1 & 0 \\ 0 & 0 & 1 & -1 \end{pmatrix}. \tag{2.66}$$

From (2.65) and (2.66) it can be seen that:

$$\mathbb{E}^{1,0} = \left(\mathbb{F}^{2,1}\right)^T, \quad \text{and} \quad \mathbb{E}^{2,1} = \left(\mathbb{F}^{1,0}\right)^T. \tag{2.67}$$

Since coboundary operator is the formal adjoint of the boundary operator, (2.67) reveals that discrete divergence and curl operators on the dual cell complex are related to the transpose of the discrete gradient and curl operators on the primal cell complex.
Once the dual cell complex is constructed, the dual of the sequence in (2.64) can be built on the dual cell complex and the two sequences can be connected using the discrete Hodge-$\star$ operator, $\star^h$. The extended De Rham complex becomes:

$$\begin{array}{ccccccccc} \mathbb{R} & \longrightarrow & C^0(K) & \xrightarrow{\delta} & C^1(K) & \xrightarrow{\delta} & C^2(K) & \xrightarrow{\delta} & 0 \\ & & \updownarrow \star^h & & \updownarrow \star^h & & \updownarrow \star^h & & \\ 0 & \longleftarrow & \tilde{C}^2(\tilde{K}) & \xleftarrow{\delta} & \tilde{C}^1(\tilde{K}) & \xleftarrow{\delta} & \tilde{C}^0(\tilde{K}) & \longleftarrow & \mathbb{R}, \end{array} \tag{2.68}$$

where $\tilde{C}^p$ is the space of all p-cochains on the dual and $\tilde{K}$ represents the dual cell complex [2].

2.3 Connecting Differential Geometry and Algebraic Topology

In order to exploit the riches of the two mathematical disciplines that were introduced, it is crucial to construct a bridge that can connect them. In this section two one way bridges will be introduced that will connect algebraic topology to differential geometry.

2.3.1 Reduction and Reconstruction of p-Forms

As was mentioned briefly in subsection 2.2.2, the connection between a p-form and a p-cochain is established by integration. The operator which is associated with integration of p-forms over p-chains is known as *Reduction operator*, $\mathcal{R}$, and its operation is defined as:

$$\langle \mathcal{R}a^p, C_p \rangle := \int_{C_p} a^p. \tag{2.69}$$

Using linearity of inner product yields:

$$\langle \mathcal{R}a^p, \sum_{i=0}^{n_p} m_{p,i} c_{p,i} \rangle = \sum_{i=0}^{n_p} m_{p,i} \langle \mathcal{R}a^p, c_{p,i} \rangle = \sum_{i=0}^{n_p} m_{p,i} \int_{c_{pi}} a^p \implies \langle \mathcal{R}a^p, c_{p,i} \rangle = \int_{c_{pi}} a^p. \tag{2.70}$$

(2.70) shows that it is possible to reduce a p-form on individual cells and sum the results over the p-chain [2].

Since the coboundary operator is the discrete counterpart of exterior derivative the following commuting De Rham diagram can be constructed:

$$\begin{array}{ccc} \Lambda^p & \xrightarrow{\mathrm{d}} & \Lambda^{p+1} \\ \mathcal{R}\downarrow & & \downarrow\mathcal{R} \\ C^p & \xrightarrow[\delta]{} & C^{p+1} \end{array} \tag{2.71}$$

which can be reexpressed as [9]:

$$\mathcal{R}\mathrm{d} = \delta\mathcal{R}. \tag{2.72}$$

The action of reduction operator can be approximately reversed using a new operator known as *reconstruction operator*, $\mathcal{I}$. Hence, reconstruction of a cochain translates it back to a differential form. Reconstruction of a differential form can be performed in a multitude of ways depending on the nature of the approximated linear functional. However, irrespective of this choice, the reconstruction operator satisfies the following two conditions:

$$\mathcal{R}\mathcal{I} = I \quad \text{(Consistency property)}, \tag{2.73}$$

$$\mathcal{I}\mathcal{R} = I + O(h^s) \quad \text{(Approximation property)}, \tag{2.74}$$

where, I is the identity matrix, and h and s are positive real numbers that specify the partition size and the order of reconstruction. This work makes extensive use of polynomial interpolation where:

$$s = p + 1, \tag{2.75}$$

and p is the order of polynomial approximation.
$\mathcal{I}$ is a linear map whose range encompasses continuous square integrable p-forms. In order for the range of $\mathcal{I}$ to encompass square integrable p-forms whose exterior derivatives are also square integrable, a new condition can be imposed to coordinate the action of exterior derivative and boundary operator:

$$\mathrm{d}\mathcal{I} = \mathcal{I}\delta. \tag{2.76}$$

Such mappings are known as conforming mimetic reconstruction operators [9].
Reduction and reconstruction operators introduced can be used to define another operator known as *projection operator*, π_h. This new operator provides an approximate continuous description of a p-form and is defined as [4]:

$$\pi_h = \mathcal{I} \circ \mathcal{R}. \tag{2.77}$$

π_h is linear,

$$\pi_h(a^p + b^p) = \pi_h a^p + \pi_h b^p, \tag{2.78}$$

and in general not a Galerkin projection, see [4].
Let Π_h be a Galerkin projection, then,

$$(\Pi_h a^p, b^p) = (a^p, b^p)\,. \tag{2.79}$$

Chapter 3

Basis Functions

It was explained in section 2.3 that the connection between algebraic topology and differential geometry is established through reduction and reconstruction operations. However, performing these operations demands a new set of mathematical tools. These constitute a set of polynomial basis that can be used in reconstruction of differential forms and a set of weights that can be used in performing integration. This chapter aims at introducing these tools in the context of mimetic spectral element method used in this work.

3.1 Lagrange Polynomials and Gauss-Lobatto Nodes

Polynomial expansion sets can be divided into two main branches: modal, and nodal expansions. Modal expansions are hierarchical, in that expansion sets of higher orders contain and are built from those of lower orders. Legendre polynomials are an example of such expansions. In contrast to modal expansions, nodal polynomial expansions are performed by using a set of $P+1$ polynomials of order p which are based on $P+1$ nodal points. Nodal expansions are non-hierarchical. Lagrange interpolation is the quintessential nodal expansion and can be used in different methods such as the Galerkin or collocation method.
Selection of a polynomial expansion set is dictated by many factors among which are: its numerical efficiency, its conditioning, its approximation property, its linear independence, and continuity at element boundaries. For a more in depth treatment of these concepts see [10]. Nodal expansions allow the interior points to be chosen freely. These points play a significant role in the stability of the approximation. This work makes extensive use of Lagrange polynomials where the interior points are the zeros of Gauss-Lobatto polynomials.
Let x_q denote a set of $P+1$ nodal points, where $0 \leqslant q \leqslant P$. Then the unique Lagrange

polynomial of order p, $h_p(x)$, can be written as:

$$h_p(x) = \frac{\prod_{q=0,q\neq p}^{P} (x - x_q)}{\prod_{q=0,q\neq p}^{P} (x_p - x_q)}. \tag{3.1}$$

$h_p(x)$ has unit value at x_p and is zero at all other nodes, $p \neq q$. Therefore, Lagrange polynomials possess discrete orthogonality:

$$h_p(x) = \delta_{pq}. \tag{3.2}$$

Using, (3.2), Lagrange interpolation of a zero-form $a^0(x)$ through $P+1$ nodal points can be written as:

$$\pi_h a^0(x) = \sum_{p=0}^{P} a(x_p) h_p(x). \tag{3.3}$$

From (3.3) it can be seen that the coefficients in Lagrange expansion have a physical meaning and represent the value of the approximate solution at the points x_p. If the approximate solution is a polynomial of order $P-1$, then $\pi_h a^0(x) = a^0(x)$. In other words, the interpolation is exact.
Let $g(x)$ represent a polynomial of order $P+1$ with zeros at $P+1$ nodes x_p. Then (3.1) can be written as:

$$h_p(x) = \frac{g(x)}{g'(x_p)(x - x_p)}. \tag{3.4}$$

For a complete treatment of how (3.4) can be used to construct a Lagrange basis with nodal points at the roots of Gauss-Lobatto polynomials see [10, 11]. The final expression for the Gauss-Lobatto Lagrange polynomials can be written as:

$$h_p(x) = \frac{PL_{P-1}(x) - PxL_P(x)}{(-P(P+1)L_P(x))(x - x_p)}, \tag{3.5}$$

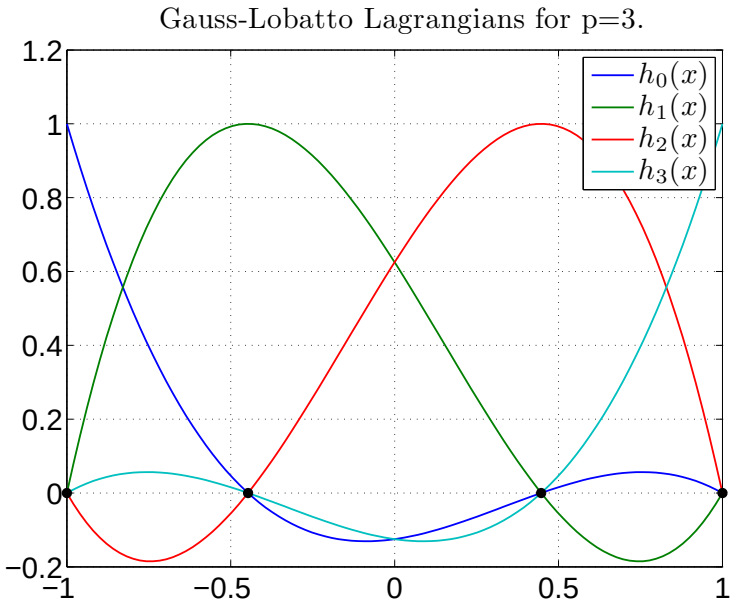

Figure 3.1: Lagrange polynomials and Gauss-Lobatto nodes.

where, $L_P(x)$ represents the Legendre polynomial of order P. Figure 3.1 shows the resulting Lagrange polynomials of order 3 and their corresponding Gauss-Lobatto nodes.

Since these polynomials make use of nodal values to interpolate a function, they are used throughout this work for reconstructing zero-forms. In 2D, these polynomials are used in combination with another set of polynomials know as edge functions to reconstruct one-forms.
The following bound for the interpolation error of zero-forms exists [4]:

$$\|a^0 - \pi_h a^0\|_{L^2\Lambda^0(\Omega)} \leqslant Ch^{l-1}|a^0|_{H^m\Lambda^0(\Omega)}, \quad \text{where, } l = \min(P+1, m). \tag{3.6}$$

$\|.\|_{L^2\Lambda^0(\Omega)}$ and $|.|_{H^m\Lambda^0(\Omega)}$ represent the norm and seminorm in the space of square integrable zero-forms and space of functions whose weak derivatives of order m and lower are square integrable. h is the maximum of all element sizes and C is a constant independent of h. From (3.6) it can be seen that the interpolation error decays faster than any power of h for analytic functions.
Following Cea's Lemma one has that the error in the solution of the weak formulation of Poisson problem is of the same order as the interpolation error. This is shown in Figure 3.2, where the convergence plot of the following Poisson problem in 1D is depicted.

$$\begin{cases} -\left(\mathrm{d}\phi^0, \mathrm{d}h^0\right) = \left(f^0, h^0\right), & x \in \Omega, \\ \phi^0 = 0, & x \in \partial\Omega. \end{cases} \tag{3.7}$$

where, $f^0 = \sin(2\pi x)$.

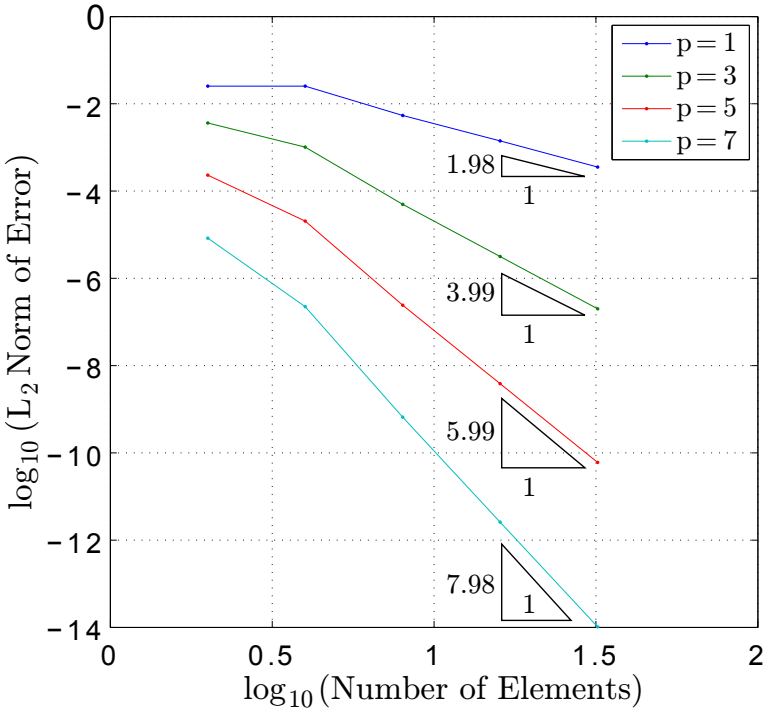

Figure 3.2: Convergence plot.

In order to perform integration, a set of weights, w, are required. These weights can be obtained as follows:

$$\begin{aligned}
&\int_{-1}^{1} \pi_h a^0(x)dx = \sum_{p=0}^{P} \pi_h a^0(x_p) w_p = \sum_{p=0}^{P} a(x_p) w_p \quad \Rightarrow \\
&\sum_{p=0}^{P} a(x_p) \int_{-1}^{1} h_p(x)dx = \sum_{p=0}^{P} a(x_p) w_p \quad \Rightarrow \\
&\int_{-1}^{1} h_p(x)dx = w_p. \qquad (3.8)
\end{aligned}$$

The final weights are [11]:

$$w_p = \frac{2}{P(P+1)\left(L_P(x_p)\right)^2}. \qquad (3.9)$$

When p-th order Lagrange polynomials are employed, use of Gauss-Lobatto nodes results in an exact integration for polynomials up to order $2p-1$.

3.2 Lagrange Polynomials and Gauss Nodes

If Lagrange polynomials are based at Gauss points instead of Gauss-Lobatto nodes, a new set of nodal polynomial expansion is obtained. These new Gauss nodes are zeros of the orthogonal polynomials, $g(x) = L_P$, and are located between Gauss-Lobatto nodes. Therefore, these nodes are good candidates for the construction of a grid dual to a grid based on Gauss-Lobatto nodes. For a discussion of how Lagrange polynomials with zeros at Gauss nodes are constructed see [11]. The new Lagrange polynomials are:

$$h_p(x) = \frac{L_P(x)}{(x-x_p)\frac{(PL_{P-1}(x_p))}{1-x_p^2}}. \tag{3.10}$$

Figure 3.3 shows the resulting polynomials of order 3 and their corresponding Gauss nodes. Note that Gauss nodes are all in the interior of [-1,1] domain.

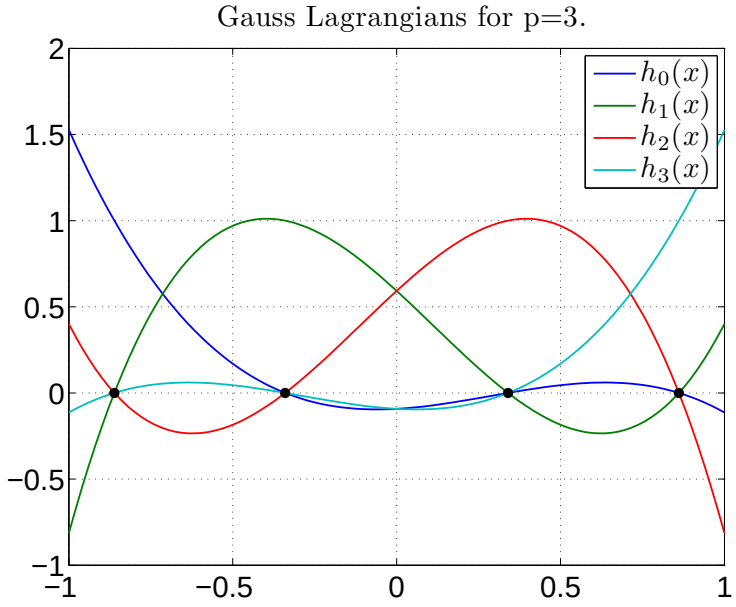

Figure 3.3: Lagrange polynomials and Gauss nodes.

For continuity reasons across element boundaries it is sometimes desirable to introduce element boundary points as expansion nodes. This is achieved by Gauss-Lobatto nodes at the

cost of lower quadrature accuracy. In this case the weights for performing integration are:

$$w_p = \frac{2}{(1-x_p^2)\left(L'_N(x_p)\right)^2}. \tag{3.11}$$

When p-th order Lagrange polynomials are employed, use of Gauss nodes results in an exact integration for polynomials up to order $2p+1$.

3.3 Edge Functions

The nodal polynomials introduced in the previous sections are zero-forms used for the reconstruction of zero-forms from zero-cochains. In order to reconstruct one-forms from one-cochains new basis functions are required. These mathematical objects known as edge functions are one-forms and have been derived in [12]. Edge functions are defined as follows:

$$e_j(x) = -\sum_{i=0}^{j-1} \mathrm{d}h_i(x), \quad \text{where,} \quad j = 1, \ldots, P, \tag{3.12}$$

where, $h_i(x)$ are the corresponding Lagrange nodal functions. A one-form, $\pi_h a^1$, can be reconstructed from its cochains, a_i, using edge functions as follows:

$$\pi_h a^1 = a_h^1(x) = \sum_{i=1}^{P} a_i e_i(x). \tag{3.13}$$

Edge functions are regularization of the delta function and satisfy:

$$\mathcal{R}\, e_j^1(x) = \int_{x_{i-1}}^{x_i} e_j(x) = \delta_{ij} = \begin{cases} 1, & \text{if } i = j, \\ 0, & \text{if } i \neq j. \end{cases} \tag{3.14}$$

Edge functions are one-tensors and as such transform as tensors under coordinate transformation. Therefore, they are independent of any coordinate system. Figure 3.4 shows edge functions of order 3 on a Gauss-Lobatto grid.

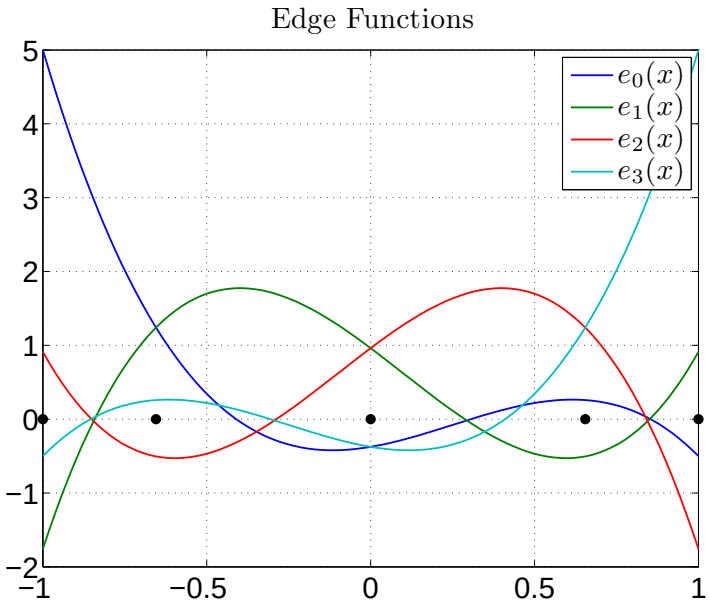

Figure 3.4: Edge functions and Gauss-Lobatto nodes.

Since the basis functions used in this work are tensors, extension to 2D and 3D is achieved through tensor product.

Chapter 4

Adjoint Error Estimation and Test Cases

In performing numerical computations which can mimic the physics of fluid flow it is vital to be able to estimate the accuracy of captured results. The resulting error within these computations stems from different sources among which is the error due to discretization of the system of p.d.e.'s. Obtaining tight error bounds on this type of error can provide the possibility of performing an optimal adaptive mesh refinement. This form of mesh refinement can in turn be used to minimize the cost of reaching a given accuracy or to produce the most accurate solution for a given cost.
Developments in the field of *a posteriori* error estimation have lead to the realization that in the majority of the time the quantities of interest are functionals of the solution of the original p.d.e.'s. Following this train of thought, the early works of Eriksson, Estep, Hansbo and Johnson [13] lead the way to the most recent advancements made by Prudhomme & Oden [14], Becker & Rannacher [15, 16], Süli & Giles [17], Giles & Pierce [18], which deals with finding the absolute error in these derived quantities. This is done by constructing an inhomogeneous adjoint p.d.e with certain boundary conditions relevant to the goal functional. The solution of this adjoint problem is then used to relate the residual, which is the extent to which the approximate result differs from the analytic solution, to the error in the goal functional.
This chapter begins with a review of the history of adjoint error estimation leading to the current advancements in this field. Next, the theory behind adjoint error estimation will be translated to the language of differential geometry, a number of test cases will be examined, and some interesting results will be introduced.

4.1 State of the Art

A mathematical model is said to be reliable if it is computable and predictable. To expound these two concepts, let A represent a differential operator and let f denote some known data.

Then the following model can be constructed [13]:

$$A(u) = f. \tag{4.1}$$

where, u denotes the exact solution of this equation and is usually an unknown quantity. Let U denote an approximated solution of (4.1). This leads to the introduction of a source of error known as computational error:

$$e_c := u - U. \tag{4.2}$$

Many mathematical models, e.g., the full Navier-Stokes equations, are too complex for direct computation. Therefore, they are usually subjected to some form of simplification. Now let $\hat{u}$ denote the solution of the complex model. Then the data-modeling error is defined as:

$$e_{dm} := \hat{u} - u. \tag{4.3}$$

Now the total error can be written as:

$$e := e_{dm} + e_c. \tag{4.4}$$

The solution of the complex model, $\hat{u}$, is said to be predictable with respect to a norm, $\| \, . \, \|$, and tolerance, $TOL > 0$, if, $\|e_{dm}\| \leq TOL$. Moreover, the exact solution of the simplified model, u, is said to be computable with respect to a norm, $\| \, . \, \|$, and tolerance, $TOL > 0$, if, $\|e_c\| \leq TOL$.
In constructing any numerical computational method the most influential elements are reliability and efficiency. Reliability means that computational error can be controlled to within a tolerance limit while efficiency means that computational work for reaching a solution is minimal [13].
A computational method is reliable and efficient if it is equipped with an adaptive discretization and a feedback system. In this way once a set tolerance level is not met in a region within the computational domain, the feedback system notifies the automated program and the discretization of that region is enriched. The estimated error during each iteration is obtained from *a posteriori* error estimator.
A posteriori error estimation for Galerkin finite element can be traced back to the pioneering works of Babuška and Rheinboldt [19], and is done with respect to the energy norm. The important factor in this form of estimator is localization of the residual norm such that it can be computed as a sum of cellwise contributions.

Within this field two main categories can be recognized. These are namely: global error estimators in energy norm, and goal-oriented error estimators. This section is dedicated to the review of these two categories. However, the emphasis will be mainly on goal-oriented error estimators as these are the focus of the work which will follow. For a more in depth treatment of these methods the reader is referred to the works of Verfürth [20], Ainsworth and Oden [21], and Grätsch and Bathe [22].

4.1.1 Global error estimators in energy norm

This class of error estimators use the data of the problem in various ways to provide an approximation of the global error in the energy norm. Within this class different groups can be recognized. These are:

- Explicit and implicit error estimators: In construction of these estimators, use is made of the fact that the true error is the unique solution of a variational boundary value problem which is equivalent to the original problem. Moreover, since the solution of the original problem is a Galerkin approximation, the error also satisfies Galerkin orthogonality condition. Explicit estimators rely explicitly on the data from the original problem and incorporate the residuals of the original problem directly into the construction of the error estimator, see for example [23, 24]. From the drawbacks of explicit error estimators one can mention the appearance of two unknown constant in the expression for the error estimate. Although research has been done to obtain the values of these constants for general problems, the results have failed to provide sharp error bounds [22]. In contrast to explicit estimators, implicit estimators involve the solution of local auxiliary boundary value problems in order to obtain an approximation for the true error. This subcategory can in turn be divided into other subclasses (e.g. Element residual method and Subdomain residual method [25, 26, 27]) depending on the nature of these local problems. While implicit methods do not suffer from unknown constants, they are more expensive because they deal with additional local auxiliary problems. However, what these methods lack in terms of computational efficiency, they make up for in terms of robustness and accuracy.

- Recovery-based error estimators: For finite element methods such as discontinuous Galerkin, the approximate solution is discontinuous across element boundaries and a gradient jump exists from one element to another. In recovery-based error estimation, this gradient jump is post-processed and the result is compared with the approximate solution to obtain an estimate of the true error, see for example [27].

Among the methods discussed here, the recovery-based error estimators perform more efficiently for linear as well as nonlinear problems and for general discretizations. These estimators provide reasonable accuracy and are cheap compared to implicit estimators and can be used to steer an adaptive scheme.

4.1.2 Goal-oriented error estimators

In numerical analysis sometimes it is not the error in the computed solution that is of interest but a functional of this solution. Examples of such quantities would be the flux through a part of the domain boundary or average value of stresses in a portion of a structure. Obtaining an approximation on this error would provide the analyst with the correct information on how the discretization of the computational domain can be altered in order to efficiently improve the resulting quantity of interest. An important point here is that any linear functional acting on the finite element space has a higher convergence rate (roughly double) than the error in the energy norm. As a result all estimators previously introduced can be employed for goal-oriented error estimation [21].
Goal-oriented error estimators rely on the solution of an adjoint problem whose construction is dictated by the target functional and their history goes back to the pioneering works of Babuška and Miller [28]. Within this framework different methods have been developed among which are:

- Energy norm based estimates: Energy norm based estimates make use of Cauchy-Schwarz inequality and relate the error in the energy norms of the dual and primal solutions to the error in the quantity of interest. However, the error bounds obtained in this way generally lead to overestimation of the error which becomes more severe for higher order polynomial interpolation functions in p-version finite element method [22, 29]. Tighter error bounds have been constructed by Prudhomme and Oden in Refs. [14, 30] by taking advantage of parallelogram identity (instead of Cauchy-Schwarz inequality) for symmetric bilinear forms, which can be used to steer an adaptive refinement process. Since these estimators rely on boundedness of functionals of interest, if the value of the solution at a single point is desired, their performance might deteriorate.

- Dual weighted residual method: These error estimators as first proposed by Rannacher and co-workers, (see Ref. [31]) are constructed by adding the contributions of the residual and the jump in the gradient of the primal solution to the error in the target functional. Dual weighted residual estimators involve the exact solution of the dual problem which can be either approximated by using a higher order method to solve the adjoint problem or by using higher order interpolation functions. This approximated exact solution is then projected onto the space of the primal solution. The difference between this projected quantity and the exact solution then provides the correct weight for the residuals. This method relies on Galerkin orthogonality to achieve a higher convergence rate for the error estimate of the functional of interest over each element [14, 15, 16, 17, 18].
  Although, this method has been successfully applied to many problems in the past (linear, nonlinear, and transient analyses), it is still subject of research for complex problems such as fluid structure interaction [22].

Even though, much has been achieved in the field of *a posteriori* error estimation for finite element methods, this field is yet new to mimetic spectral element methods. Following the

recent advancements on the confluence of these two fields (see for example [32]) and due to similarities shared between mimetic spectral element and finite element methods, new interpretations of these error estimators in the language of differential geometry is made possible. The recent works of Kreeft and Gerritsma on a priori error estimates [33] and Demlow and Hirani [34] on residual type *a posteriori* error estimates constitute the most recent developments in this area.

4.2 Theory

A sound way of approaching the theory behind duality and adjoint error estimation is through introduction of the Green's function. However, before doing so it is necessary to introduce the function spaces which will be used throughout this work.
The current work makes extensive use of the space of continuous real valued square integrable p-forms on a complete oriented Riemannian manifold Ω. This space, denoted by $L^2\Lambda^p(\Omega)$, is equipped with inner product,

$$(a^p, b^p) = \int_\Omega a^p \wedge \star b^p, \tag{4.5}$$

and is complete with respect to the norm,

$$\|a^p\|_{L^2\Lambda^p(\Omega)} = \left(\int_\Omega a^p \wedge \star a^p \right)^{1/2}. \tag{4.6}$$

$L^2\Lambda^p(\Omega)$ is a Hilbert space and isomorphic to its dual.
The Sobolev space $H\Lambda^p(\Omega)$ that is associated with the exterior derivative is defined as [33]:

$$H\Lambda^p(\Omega) = \left\{ a^p \in L^2\Lambda^p(\Omega) : \mathrm{d}a^p \in L^2\Lambda^{p+1}(\Omega) \right\}. \tag{4.7}$$

$H\Lambda^p(\Omega)$ is a Hilbert space equipped with the following norm and seminorm:

$$\|a^p\|^2_{H\Lambda^p(\Omega)} = \|a^p\|^2_{L^2\Lambda^p(\Omega)} + \|\mathrm{d}a^p\|^2_{L^2\Lambda^{p+1}(\Omega)}, \quad |a^p|_{H\Lambda^p(\Omega)} = \|\mathrm{d}a^p\|_{L^2\Lambda^{p+1}(\Omega)}. \tag{4.8}$$

In order to avoid technical difficulties that might arise when introducing the dual space of $H\Lambda^p(\Omega)$ a subspace of this space needs to be defined. This new space denoted by $H_0\Lambda^p(\Omega)$

is defined as:

$$H_0\Lambda^p(\Omega) = \{a^p \in H\Lambda^p(\Omega) : \text{tr } a^p = 0 \text{ on } \partial\Omega\}\,. \tag{4.9}$$

Let L denote a linear differential operator in Ω. Moreover, let u^p and f^q belong to appropriate spaces, where, p,$q = 0$, or 1. Now consider a problem of the form:

$$\begin{cases} Lu^p = f^q, & x \in \Omega, \\ \text{suitable b.c. and i.c.}, & x \in \partial\Omega. \end{cases} \tag{4.10}$$

where, the suitability of the boundary and initial conditions are such that (4.10) assumes unique solutions.
The Green's function for (4.10) is a q-form, v^q, (where, $q = 0$, or 1), which satisfies the system:

$$\begin{cases} L^*v^q = \delta_y^p(x), & x \in \Omega, \\ \text{suitable adjoint b.c. and i.c.}, & x \in \partial\Omega, \end{cases} \tag{4.11}$$

where L^* is the formal adjoint of the operator L and δ_y^p is the delta-function at point $y \in \Omega$ in 1D. It should be noted that the delta-function is a distribution (it is a linear and continuous functional) whose action demands a certain amount of smoothness. Next using the Green's function, the solution of the primal problem at y can be obtained as follows:

$$\left(u^p, \delta_y^p\right) = (u^p, L^*v^q) = (Lu^p, v^q) = (f^q, v^q)\,. \tag{4.12}$$

From (4.12) it can be seen that the value of the p-form, u^p, at y is given by the linear functional $(u^p, \delta_y^p(x))$. However, generally the quantities of interest are not summarized in the value of u^p at a point. Hence, this result needs to be generalized to encompass other linear functionals that might be of interest and this can be achieved by reviewing an important theorem known as Riesz Representation theorem.

> **Theorem: Riesz Representation** There is a one to one correspondence between every bounded linear functional F on a Hilbert space X and a unique element of X, denoted by u^p such that
>
> $$F(v^p) = (u^p, v^p) \quad \forall v^p \in X. \tag{4.13}$$
>
> where, $u^p \in X$ and F belongs to the dual space of X.

Following Riesz Representation theorem the result in (4.12) can be generalized to many other quantities that can be expressed as linear functionals on the space Ω. This leads to the introduction of the new linear functional of interest, (u^p, g^p), and the generalized Green's function, v^q.

$$\begin{cases} L^* v^q = g^p, & x \in \Omega, \\ \text{suitable adjoint b.c. and i.c.}, & x \in \partial\Omega. \end{cases} \tag{4.14}$$

Moreover, since a p-form in $L^2\Lambda^p(\Omega)$ is only defined almost everywhere, it does not make sense to talk about its value at a point. Therefore, a certain level of smoothness is required for the value of the solution of the primal problem to be well-defined at a point in two or more dimensions (for example, in order for the value of a p-form at a point to make sense in 2D, it must belong to the space $L^3\Lambda^p(\Omega)$). Hence, to avoid these restrictions, instead of $(u^p, \delta_y^p(x))$, now the mollification of u^p in some neighborhood of point y is considered [1]. As a result, p and q in (4.10) and (4.11) are not necessarily restricted to 1D anymore [21].

Now that a generalization to higher dimensions and a larger class of linear functionals has been achieved, the following variational formulation is considered:

$$(Lu^p, v^q) = (f^q, v^q) \quad \text{where,} \quad u^p \in H_0\Lambda^p(\Omega), \;\; \forall v^q \in H_0\Lambda^q(\Omega). \tag{4.15}$$

To introduce the mimetic spectral element solution of this problem, let $\partial\Omega$ be the boundary of Ω and let $\mathcal{T}_h$ denote a partition of Ω into elements Ω_K where $K = 1, \ldots, N$ and N is the number of elements. Moreover, let $\Lambda_h^p(\Omega) \subset H_0\Lambda^p(\Omega)$ denote the mimetic spectral element solution space of p-forms with compact support on Ω. Then, (4.15) can be written as:

$$(LU^p, V^q) = (f^q, V^q) \quad \text{where,} \quad U^p \in \Lambda_h^p(\Omega), \;\; \forall\, V^q \in \Lambda_h^q(\Omega). \tag{4.16}$$

Solving (4.16) in this form yields for all $v^q \in \Lambda^q(\Omega)$:

$$(f^q - LU^p, v^q) = (L(e^p), v^q) = (R(U^p), v^q) = \mathcal{R}(v^q). \tag{4.17}$$

where, $e^p := u^p - U^p$, is the error and $R(U^p)$ is the residual. $\mathcal{R}(v^q)$ is known as the weak residual and is a bounded linear functional on $\Lambda^q(\Omega)$. From (4.16) it can be seen that if

[1] Any p-form can be written as a linear combination of delta-functions. Also, it is interesting to note that the edge functions introduced in the previous chapter are mollifications of delta-functions.

$v^q = V^q \in \Lambda_h^q(\Omega)$, then:

$$(f^q - LU^p, V^q) = (R(U^p), V^q) = \mathcal{R}(V^q) = 0. \tag{4.18}$$

(4.18) states that the residual is orthogonal to the space $\Lambda_h^q(\Omega)$. This is known as *Galerkin orthogonality*.
$R(U^p)$ is a measure of how well the numerical solution, U^P, satisfies equation (4.10). Following the mentioned description for the residual an error bound can be constructed for a functional of interest as follows:

$$\begin{aligned} &Lu^p - LU^p = R(U^p) \implies Le^p = R(U^p) \implies \\ &(e^p, g^p) = (e^p, L^* v^q) = (Le^p, v^q) = (R(U^p), v^q)\,. \end{aligned} \tag{4.19}$$

Using generalized Cauchy inequality leads to the following error bound:

$$|\,(e^p, g^p)\,| \leqslant \|R(U^p)\|\|v^q\|, \quad \text{where,} \quad \|R(U^p)\| := \sup_{v^q \in \Lambda^q(\Omega)\setminus\{0\}} \frac{|\mathcal{R}(v^q)|}{\|v^q\|}. \tag{4.20}$$

Since real inner product spaces are considered, the modulus in (4.20) can be eliminated. (e^p, g^p) is a linear functional and can be written as:

$$J(u^p) - J(U^p) = (e^p, g^p) = (R(U^p), v^q)\,. \tag{4.21}$$

Let $\pi_h v^q$ be the mimetic projection of the exact solution to the dual problem, $v^q \in \Lambda^q(\Omega)$, onto the mimetic spectral element space $\Lambda_h^q(\Omega)$. Then using Galerkin orthogonality from (4.18) yields:

$$J(u^p) - J(U^p) = (R(U^p), v^q - \pi_h v^q)\,. \tag{4.22}$$

Since Hilbert spaces are considered, the right hand side in (4.22) is a bounded bilinear form.

Moreover, assuming $\|R(U^p)\|$ and $\|u^p - U^p\|$ converge at the same rate [2], yields,

$$\|R(U^p)\|\|v^q - \pi_h v^q\| \leqslant M\|u^p - U^p\| \, \|v^q - \pi_h v^q\|, \tag{4.23}$$

where, M is a constant. (4.23) shows that if $\|u^p - U^p\|$ converges with $\mathcal{O}(h^m)$ and $\|v^q - \pi_h v^q\|$ converges with $\mathcal{O}(h^n)$, then, the error in the functional of interest, $J(u^p) - J(U^p)$, converges with, $\mathcal{O}(h^{m+n})$.
In the following sections the theory that was presented here will be used to construct dual weighted residual error estimators when standard variational, or mixed methods are considered.

4.3 Standard Variational Method: Poisson in 1D

This section focuses on the construction of dual weighted residual error estimators when the standard variational method is considered. For simplicity the focus will be on the Poisson problem.

4.3.1 Derivation of the Dual Problem

To illustrate the method introduced in the previous section the Poisson equation in 1D provides a good starting point. Moreover, for simplicity, homogeneous boundary conditions are considered. Let $\Omega \subset \mathbb{R}$ and let $\partial\Omega$ be its boundary. Moreover, let $\phi^0 \in H\Lambda^0(\Omega)$ and let f^0 belong to an appropriate space. Then, the primal Poisson problem becomes:

$$\begin{cases} \Delta\phi(x) = f(x), & x \in \Omega, \\ \phi(x) = 0, & x \in \partial\Omega. \end{cases} \tag{4.24}$$

Using the definition of Laplace operator introduced in the previous chapter this problem can be written in the language of differential geometry as:

$$\begin{cases} \star \mathrm{d} \star \mathrm{d}\phi^0 = f^0, & x \in \Omega, \\ \phi^0 = 0, & x \in \partial\Omega. \end{cases} \tag{4.25}$$

[2] For the Poisson equation which is the focus of the current work this follows directly from Poincaré inequality.

Moreover, consider the map $J : \Lambda^0(\Omega) \to \mathbb{R}$. Then the functional under investigation is chosen to be:

$$J(\phi^0) = \int_\Omega g^0 \wedge \star\phi^0. \tag{4.26}$$

where, g^0 is a user specified weight.
Now the adjoint problem can be derived by multiplying the primal problem with a test function and performing integration by parts. To do so, let $\psi^0 \in H\Lambda^0(\Omega)$. Multiplying (4.25) by ψ^0 and integrating by parts yields:

$$\begin{aligned}
\left(\star\mathrm{d}\star\mathrm{d}\phi^0, \psi^0\right) &= \int_\Omega \star\mathrm{d}\star\mathrm{d}\phi^0 \wedge \star\psi^0 = \int_\Omega \star\mathrm{d}\star\mathrm{d}\phi^0 \wedge \tilde{\psi}^1 = \left(\tilde{\psi}^1, \mathrm{d}\star\mathrm{d}\phi^0\right) = \dots \\
\dots &= \int_\Omega \mathrm{d}\star\mathrm{d}\phi^0 \wedge \star\tilde{\psi}^1 = \int_\Omega \mathrm{d}\left(\star\mathrm{d}\phi^0 \wedge \star\tilde{\psi}^1\right) - \int_\Omega \star\mathrm{d}\phi^0 \wedge \mathrm{d}\star\tilde{\psi}^1 = \dots \\
\dots &= \int_\Omega \mathrm{d}\left(\star\mathrm{d}\phi^0 \wedge \star\tilde{\psi}^1\right) - \int_\Omega \mathrm{d}\phi^0 \wedge \star\mathrm{d}\star\tilde{\psi}^1 = \dots \\
\dots &= \int_\Omega \mathrm{d}\left(\star\mathrm{d}\phi^0 \wedge \star\tilde{\psi}^1\right) - \int_\Omega \mathrm{d}\left(\phi^0 \wedge \star\mathrm{d}\star\tilde{\psi}^1\right) + \int_\Omega \phi^0 \wedge \mathrm{d}\star\mathrm{d}\star\tilde{\psi}^1 = \dots \\
\dots &= \int_{\partial\Omega} \left(\star\mathrm{d}\phi^0 \wedge \psi^0 - \phi^0 \wedge \star\mathrm{d}\star\tilde{\psi}^1\right) + \int_\Omega \phi^0 \wedge \mathrm{d}\star\mathrm{d}\star\tilde{\psi}^1.
\end{aligned} \tag{4.27}$$

where the tilde, $\tilde{}$, means that $\tilde{\psi}$ belongs to the dual grid. Assuming ϕ^0 and ψ^0 both have compact support in Ω, the adjoint of the Laplace operator can be recognized as:

$$\left(\star\mathrm{d}\star\mathrm{d}\phi^0, \psi^0\right) = \left(\phi^0, \star\mathrm{d}\star\mathrm{d}\star\tilde{\psi}^1\right) = \left(\phi^0, \star\mathrm{d}\star\mathrm{d}\psi^0\right). \tag{4.28}$$

(4.28) is a confirmation of the fact that the Laplace operator is formally self-adjoint.
The adjoint boundary conditions are minimal conditions that make the boundary conditions which appear when performing integration by parts vanish. Hence, the adjoint boundary conditions can be obtained through evaluation of the bilinear identity. Rewriting the last line in (4.27) yields:

$$\int_\Omega \mathrm{d}\star\mathrm{d}\phi^0 \wedge \psi^0 - \int_\Omega \phi^0 \wedge \mathrm{d}\star\mathrm{d}\psi^0 = \int_{\partial\Omega} \left(\star\mathrm{d}\phi^0 \wedge \psi^0 - \phi^0 \wedge \star\mathrm{d}\psi^0\right). \tag{4.29}$$

From the boundary conditions specified in (4.24) the last term on the right hand side of (4.29) vanishes. In order for the first term on the right hand side to vanish the adjoint boundary condition becomes, $\psi^0 = 0$ on $\partial\Omega$ [35].
Finally, the dual problem can be written as:

$$\begin{cases} \Delta\psi(x) = g, & x \in \Omega, \\ \psi(x) = 0, & x \in \partial\Omega. \end{cases} \tag{4.30}$$

where, g is the user specified weight in (4.26). In the language of differential geometry this problem can be formulated as:

$$\begin{cases} \star \mathrm{d} \star \mathrm{d}\psi^0 = g^0, & x \in \Omega, \\ \psi^0 = 0, & x \in \partial\Omega. \end{cases} \tag{4.31}$$

or as,

$$\begin{cases} \mathrm{d} \star \mathrm{d} \star \tilde{\psi}^1 = \tilde{g}^1, & x \in \Omega, \\ \star\tilde{\psi}^1 = 0, & x \in \partial\Omega. \end{cases} \tag{4.32}$$

(4.31) and (4.32) are both dual problems to (4.25). However, there is a difference between the two, namely, that the former can be solved using Galerkin's method while the latter proves unsolvable as it stands. Therefore, a different construction must be considered for (4.32). A more thorough explanation on how (4.32) can be reformulated is given in appendix C.
The primal and the dual problems can be combined to form the following saddle point system:

$$\begin{pmatrix} 0 & A \\ A^T & 0 \end{pmatrix} \begin{pmatrix} y \\ x \end{pmatrix} = \begin{pmatrix} f \\ g \end{pmatrix}. \tag{4.33}$$

where, in this example,

$$A = \star \mathrm{d} \star \mathrm{d}, \quad A^T = \star \mathrm{d} \star \mathrm{d}, \quad y = \psi^0, \quad x = \phi^0, \quad g = g^0, \quad f = f^0. \tag{4.34}$$

However, due to simplicity of these two problems in this case and the fact that neither is under- or over-determined they can be solved seperately.
In the next section the dual problem (4.31) will be used to construct an adjoint error estimator.

4.3.2 Derivation of an Adjoint Error Estimator

In order to construct a dual weighted residual error estimator the convetional approach involves problems in their normal variational form. Therefore, using (4.28), the following primal and dual problems will be considered:

$$\text{Primal problem} \quad \begin{cases} \star \mathrm{d} \star \mathrm{d}\phi^0 = f^0, & x \in \Omega, \\ \phi^0 = 0, & x \in \partial\Omega. \end{cases} \tag{4.35}$$

$$\text{Dual problem} \quad \begin{cases} \star \mathrm{d} \star \mathrm{d}\psi^0 = g^0, & x \in \Omega, \\ \psi^0 = 0, & x \in \partial\Omega. \end{cases} \tag{4.36}$$

The grids used for solving these two problems are of Gauss-Lobatto type and are depicted in figure 4.1.

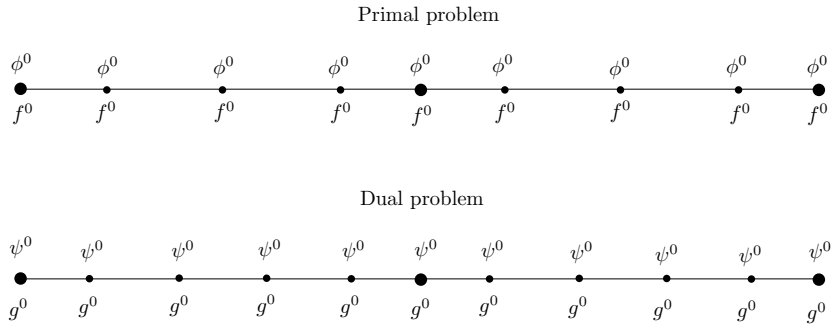

Figure 4.1: Grids used for solving the primal and the dual problems.

The reasons why the dual problem is solved on a higher order grid rest in the construction of the dual weighted residual error estimator and will be explained shortly. Now the target error quantity can be expressed as:

$$
\begin{aligned}
J(\phi^0) - J(\phi_h^0) &= \left(g^0, \phi^0\right) - \left(g^0, \phi_h^0\right) = \int_\Omega g^0 \wedge \star\phi^0 - \int_\Omega g^0 \wedge \star\phi_h^0 = \dots \\
\dots &= \int_\Omega \star \mathrm{d} \star \mathrm{d}\psi^0 \wedge \star \left(\phi^0 - \phi_h^0\right) = \int_\Omega \mathrm{d} \star \mathrm{d}\psi^0 \wedge \left(\phi^0 - \phi_h^0\right) = \dots \\
\dots &= \int_{\partial\Omega} \star \mathrm{d}\psi^0 \wedge \left(\phi^0 - \phi_h^0\right) - \int_\Omega \star \mathrm{d}\psi^0 \wedge \mathrm{d}\left(\phi^0 - \phi_h^0\right) = \dots \\
\dots &= \int_{\partial\Omega} \star \mathrm{d}\psi^0 \wedge \left(\phi^0 - \phi_h^0\right) - \int_\Omega \star \mathrm{d}\psi^0 \wedge \mathrm{d}\phi^0 + \int_\Omega \star \mathrm{d}\psi^0 \wedge \mathrm{d}\phi_h^0 = \dots \\
\dots &= \int_{\partial\Omega} \left(\star \mathrm{d}\psi^0 \wedge \left(\phi^0 - \phi_h^0\right) - \left(\psi^0 \wedge \star \mathrm{d}\phi^0\right)\right) + \int_\Omega \psi^0 \wedge \mathrm{d} \star \mathrm{d}\phi^0 + \dots \\
\dots &+ \int_\Omega \star \mathrm{d}\psi^0 \wedge \mathrm{d}\phi_h^0. \qquad (4.37)
\end{aligned}
$$

where, $\phi_h^0 \in \Lambda_h^0(\Omega) \subset H_0\Lambda^0(\Omega)$, and is the approximated solution of the primal problem. Using the prescribed boundary conditions in (4.35) and (4.36) yields:

$$
J(\phi^0) - J(\phi_h^0) = \int_\Omega f^0 \wedge \star\psi^0 + \int_\Omega \star \mathrm{d}\psi^0 \wedge \mathrm{d}\phi_h^0. \qquad (4.38)
$$

Considering (4.19) and (4.21) and employing Galerking orthogonality results in:

$$
J(\phi^0) - J(\phi_h^0) = \int_\Omega f^0 \wedge \star \left(\psi^0 - \pi_h\psi^0\right) + \int_\Omega \star \mathrm{d} \left(\psi^0 - \pi_h\psi^0\right) \wedge \mathrm{d}\phi_h^0. \qquad (4.39)
$$

where, $\pi_h\psi^0 \in \Lambda_h^0(\Omega)$, is the mimetic projection of the solution of the dual problem onto the points of the primal grid. Once again using integration by parts yields:

$$
\begin{aligned}
J(\phi^0) - J(\phi_h^0) &= \int_\Omega f^0 \wedge \star \left(\psi^0 - \pi_h\psi^0\right) + \int_\Omega \star \mathrm{d} \left(\psi^0 - \pi_h\psi^0\right) \wedge \mathrm{d}\phi_h^0 = \dots \\
\dots &= \int_\Omega f^0 \wedge \star \left(\psi^0 - \pi_h\psi^0\right) + \int_{\partial\Omega} \left(\psi^0 - \pi_h\psi^0\right) \wedge \star \mathrm{d}\phi_h^0 - \dots \\
\dots &- \int_\Omega \left(\psi^0 - \pi_h\psi^0\right) \wedge \mathrm{d} \star \mathrm{d}\phi_h^0 = \dots \\
\dots &= \int_\Omega \left(f^0 - \star \mathrm{d} \star \mathrm{d}\phi_h^0\right) \wedge \star \left(\psi^0 - \pi_h\psi^0\right) + \dots \\
\dots &+ \int_{\partial\Omega} \star \mathrm{d}\phi_h^0 \wedge \left(\psi^0 - \pi_h\psi^0\right). \qquad (4.40)
\end{aligned}
$$

The error in the chosen functional is governed by the residual and the last line of (4.40) is a reduction of the residual into an interior and a boundary component.
Let $\mathcal{T}_h$ denote a partition of Ω into elements Ω_K where $K = 1, \dots, N$ and N is the number of elements. Then (4.40) can be written as:

$$\begin{aligned} & J(\phi^0) - J(\phi_h^0) = \sum_K \eta_K = \dots \\ \dots \quad = \quad & \sum_K \left\{ \int_{\Omega_K} \left(f^0 - \star \mathrm{d} \star \mathrm{d}\phi_h^0 \right) \wedge \star \left(\psi^0 - \pi_h \psi^0 \right) + \int_{\partial\Omega_K} \frac{1}{2} \left[\star \mathrm{d}\phi_h^0 \right] \wedge \left(\psi^0 - \pi_h \psi^0 \right) \right\}. \end{aligned} \tag{4.41}$$

The expression in (4.41) is computed for each element in order to obtain their individual contributions to the global error. Partitioning the global error quantity in this way causes the boundary integral in the last line of (4.40) to be considered twice when moving over an edge between two elements (once for the left and once for the right elements). Therefore, the boundary term in (4.41) now involves half the jump in the gradient across internal element faces and is defined to be zero on $\partial\Omega_K \cap \partial\Omega$. Moreover, the error estimate in (4.41) now depends on the exact solution of the dual problem, ψ^0. Since in practice this quantity is unknown, a number of ways have been introduced by Becker and Rannacher [15], and Giles and Süli [17], to circumvent this problem. Some of these ideas are as follows:

(1) Approximation using a higher order scheme: This method involves approximating the true value of the solution of the dual problem by solving the adjoint equation with higher order piecewise polynomials compared to the primal problem. This approach might not be very economical since the cost of solving the adjoint problem might be considerably larger than the primal problem [15].

(2) Approximation using a higher order interpolation: In this approach the dual problem is computed on the same mesh as the primal equation and the result is interpolated using higher order interpolation functions to find an approximation for ψ^0.
Consider a 2×2 cell patch with second order polynomial interpolation in 2D. The total number of points in this cell complex is 25, which can be used to construct an interpolation of degree 4. This is done by treating the 2×2 cell patch as one element and employing a fourth order polynomial interpolation on this single element. This is indicated by $\mathcal{I}_{2h}^{(2)} \psi_h^0$, where the superscript, (2), denotes an interpolation order, twice that of the primal problem, and the subscript, $2h$, indicates that this interpolation is performed on two elements instead of one [15].

(3) Global refinement: In this approach the exact solution to the dual problem is approximated by solving the adjoint equation on a globally refined mesh with respect to the primal problem (i.e. higher number of elements). Again, as in the case of (1), this

approach is not very economical since the cost of solving the adjoint equation might be high [17].

(4) Different dual and primal meshes: This approach is based on the idea that since the dual and primal solutions in general exhibit different behavior it is reasonable to solve the dual equation on a dual mesh which is relevant to its behavior. The drawback here is the additional effort needed for an daptive design of the dual mesh and transference of data between different mesh families [17].

In order to obtain the contribution of each element to the global error quantity it is also possible to leave the residual in the weak form as in (4.39) and write [22]:

$$\begin{aligned} & J(\phi^0) - J(\phi_h^0) = \sum_K \eta_K = \dots \\ \dots \quad = \quad & \sum_K \left\{ \int_{\Omega_K} f^0 \wedge \star \left(\psi_h^0 - \pi_h \psi^0\right) + \int_{\Omega_K} \star \mathrm{d}\left(\psi_h^0 - \pi_h \psi^0\right) \wedge \mathrm{d}\phi_h^0 \right\}, \end{aligned} \tag{4.42}$$

where, $\psi_h^0 \in \bar{\Lambda}_h^0(\Omega)$, and $\bar{\Lambda}_h^0(\Omega)$ is a polynomial space different from $\Lambda_h^0(\Omega)$ (in one of the ways explained above). Moreover, since now the dual solution is approximated, one has:

$$J(\phi^0) - J(\phi_h^0) \approx \sum_K \eta_K, \tag{4.43}$$

which leads to the following approximate bound for the error:

$$|J(\phi^0) - J(\phi_h^0)| \leqslant \sum_K \left\{ \int_{\Omega_K} |f^0 \wedge \star \left(\psi_h^0 - \pi_h \psi^0\right) + \star \mathrm{d}\left(\psi_h^0 - \pi_h \psi^0\right) \wedge \mathrm{d}\phi_h^0| \right\}. \tag{4.44}$$

In the next section the results obtained from a dual weighted residual error estimator constructed following (4.42) and (1) will be discussed.

4.3.3 Results for Poisson equation in 1D

Considering the expression in (4.42), for a case where the second expression under summation vanishes one has:

$$J(\phi^0) - J(\phi_h^0) \approx \sum_K \eta_K = \dots$$

$$\dots = \sum_K \left\{ \int_{\Omega_K} f^0 \wedge \star \left(\psi_h^0 - \pi_h \psi^0 \right) \right\} = \int_\Omega g^0 \wedge \star \left(\phi^0 - \phi_h^0 \right). \tag{4.45}$$

(4.45) suggests that if a higher order solution of the dual problem is considered to be the representative of the exact solution of the adjoint equation in the finite domain, then in order to verify the results obtained from the error estimator, the exact solution of the primal problem, ϕ^0, needs to be at least considered in the same polynomial space as the exact finite solution of the dual problem [3]. Bearing this point in mind, the following primal and dual problems are considered:

$$\text{Primal problem} \quad \begin{cases} \star \mathrm{d} \star \mathrm{d}\phi^0 = \cos(2\pi x), & x \in \Omega, \\ \phi^0 = 0, & x \in \partial\Omega. \end{cases} \tag{4.46}$$

$$\text{Dual problem} \quad \begin{cases} \star \mathrm{d} \star \mathrm{d}\psi^0 = \cos(2\pi x), & x \in \Omega, \\ \psi^0 = 0, & x \in \partial\Omega. \end{cases} \tag{4.47}$$

Now the error estimator can be constructed as in (4.43) and the error over each element can be approximated. The results for 5, 10, and 15 elements with second order polynomial interpolation are depicted in Figure 4.3 (the order of the dual problem is therefore three). Moreover, Figure 4.2 depicts the convergence of the effectivity index defined as:

$$\lambda = \frac{\sum_K |\eta_K|}{\sum_K \left| \int_K (\star\phi^0 \wedge g^0) - (\star\phi_h^0 \wedge g^0) \right|}, \tag{4.48}$$

and the error bounds when increasing the number of elements from 1 to 25.
Comparing the left and the right columns in Figure 4.3 shows that the estimator is capable of estimating the error on each individual element accurately even when low numbers of elements are considered. Figure 4.2 shows the convergence of the total estimated error towards the actual total error. It can be seen that this convergence is fast and reaches approximately 0.95 when only three elements are considered. Furthermore, It can be seen that the error bound introduced in (4.44) tightly bounds the exact and the estimated error as they approach zero,

[3] Note that reduction of the true solution of the primal on the points of the dual grid generally results in a more accurate representation of the true error.

one almost on top of the other. For additional results see appendix (D).
In obtaining these results the order of integration of the exact error was kept equal to the polynomial order of the dual problem while the order of integration of the estimator was set to 2 orders higher than the polynomial order of the primal problem. Although, the results that were presented here show good convergence and high accuracy of the error estimator, often high orders of integration are required for achieving highly accurate results. This shortcoming is in addition to the requirement of solving the dual solution more accurately than the primal problem. As a result this method can prove to be costly if the break even point is not predicted accurately. This is dependent on the problem where the reduction in the computational resources due to adaptive refinement is weighed against the additional cost of a dual solution and high orders of integration.

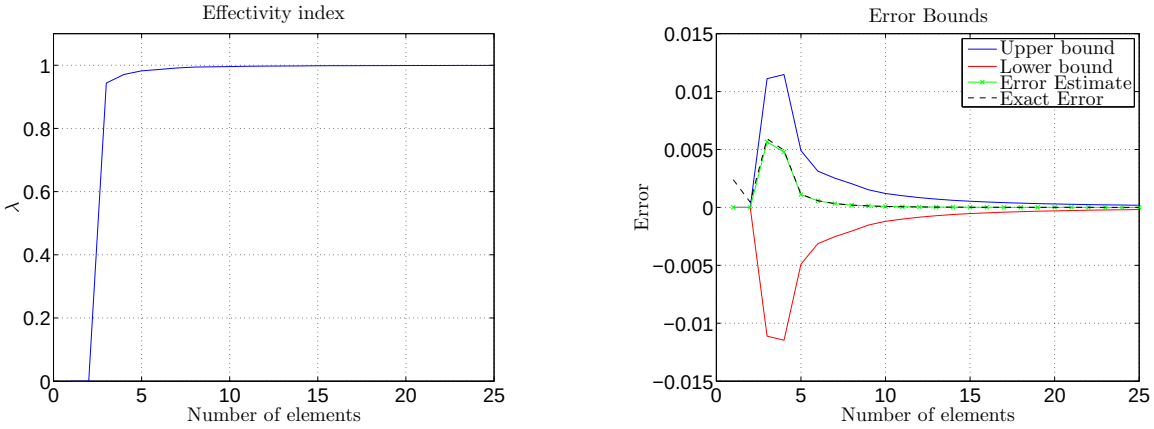

(a) Convergence of the effectivity index.

(b) Exact and estimated error and the error bounds.

Figure 4.2: Convergence of the effectivity index and the error bounds as the number of elements grow from 1 to 25.

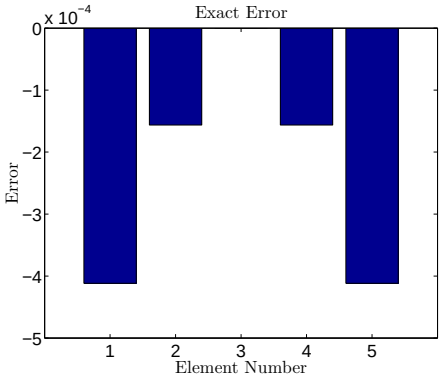

(a) Exact error over each element for 5 elements.

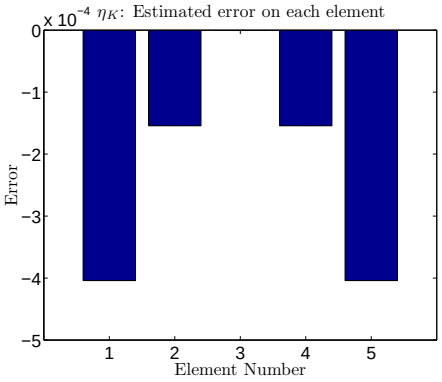

(b) Estimated error over each element for 5 elements.

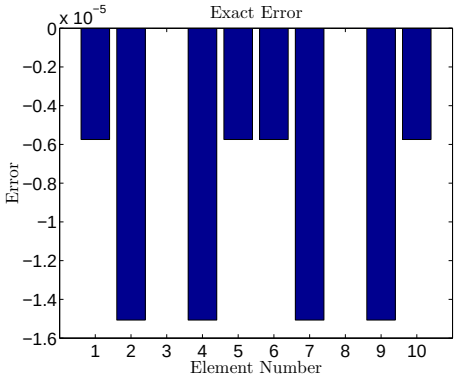

(c) Exact error over each element for 10 elements.

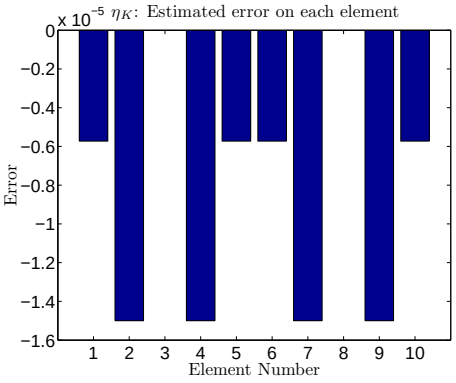

(d) Estimated error over each element for 10 elements.

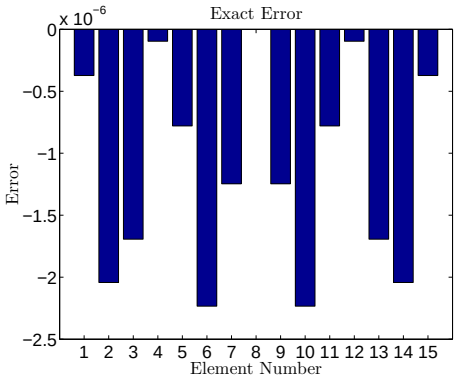

(e) Exact error over each element for 15 elements.

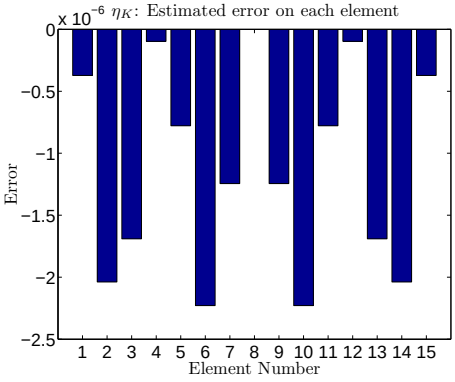

(f) Estimated error over each element for 15 elements.

Figure 4.3: Exact and estimated error for 5, 10, and 15 elements with second order polynomial interpolation.

In order to further test the performance of this error estimator similar results have been obtained for one different right hand side of the dual problem and two different right hand sides of the primal problem. Here they will be referred to as g_1^0, f_2^0, and f_3^0. Moreover, to eliminate the influence of integration error as much as possible the order of integration of the dual and primal problems are set to 10 orders higher than the polynomial order of the primal problem. The order of integration of the exact error is kept equal to the polynomial order of the dual problem. The following paragraphs discuss the results.

Trial Case 1:

In this case the right hand side of the dual problem, g_1^0, is chosen to be:

$$g_1^0 = e^{-500|x-1|}, \tag{4.49}$$

and is the regularization of the delta function on the boundary of the domain. The right hand side of the primal problem is kept as $\cos(2\pi x)$ [4].The results for this case are shown in Figures 4.4 and 4.5.

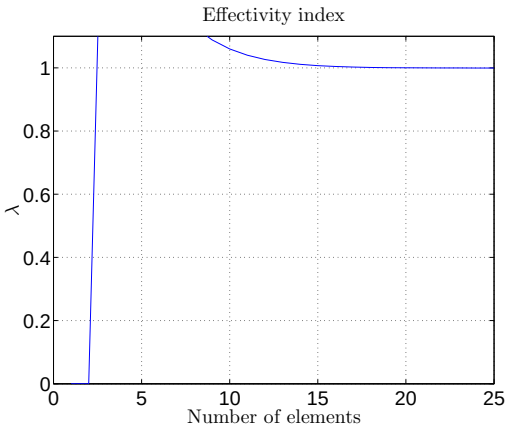

(a) Effectivity index for the case $\star \mathrm{d} \star \mathrm{d}\psi_1^0 = g_1^0$.

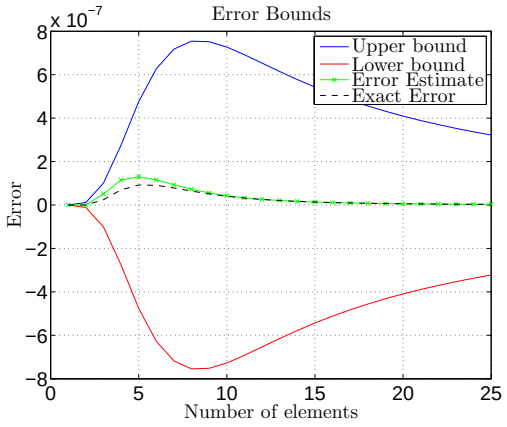

(b) Error bounds for the case $\star \mathrm{d} \star \mathrm{d}\psi_1^0 = g_1^0$.

Figure 4.4: Convergence of the effectivity index and the error bounds for the case $\star \mathrm{d} \star \mathrm{d}\psi_1^0 = g_1^0$.

From Figure 4.4 it can be seen that the effectivity index approaches 1 from above and when approximately nine elements are considered, it falls within a $\pm 10\%$ bound of 1. Moreover, it can be seen that the error bounds correctly bound the actual and the estimated error and approach zero as these quantities converge. Figure 4.5 shows that the estimated error is

[4]Note that the solution of the primal problem in this case is a continuous function. Therefore, according to Sobolev theorem, restriction of this function to a submanifold of zero dimension is well-defined. However, since polynomial interpolation is considered to avoid Gibbs phenomenon the delta function must be regularized.

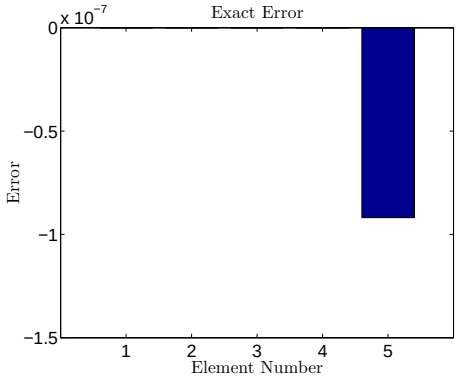

(a) Exact error over each element for 5 elements.

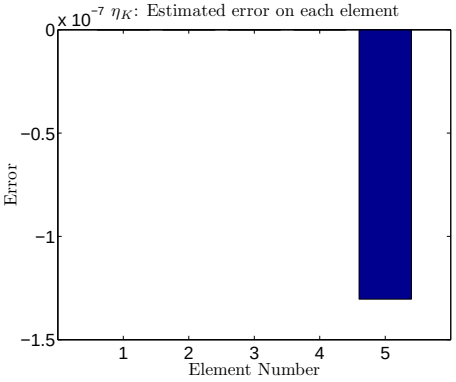

(b) Estimated error over each element for 5 elements.

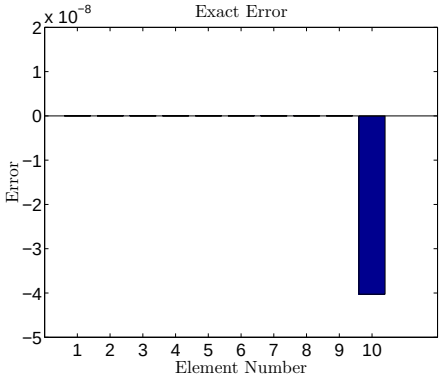

(c) Exact error over each element for 10 elements.

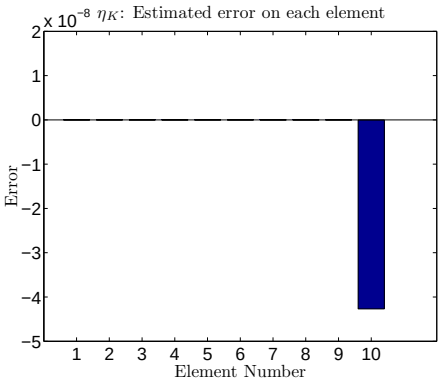

(d) Estimated error over each element for 10 elements.

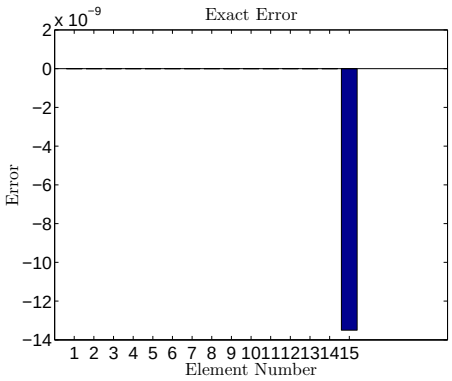

(e) Exact error over each element for 15 elements.

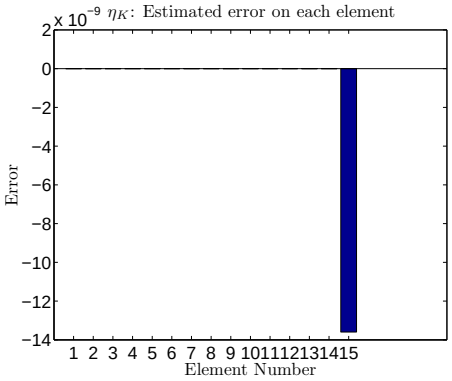

(f) Estimated error over each element for 15 elements.

Figure 4.5: Exact and estimated error for 5, 10, and 15 elements with second order polynomial interpolation for the primal problem.

correctly predicted to be higher on the element closest to the boundary at 1. It can be seen that the approximated and the actual error are in good agreement.
A comparison of the convergence rate of the effectivity index and error bounds in this case with the previous example reveals that a slower convergence is achieved. The reason for this discrepancy is that the convergence of the error estimator is dependent on how fast the solution of the primal and dual problems converge to the real values. In this case, since uniform refinement is considered, convergence of the error estimate is far from optimal. To rectify this shortcoming, refinement must be directed towards the elements that contain the largest error. For the previous case where both right hand sides (for the dual and the primal problems) were $\cos(2\pi x)$, the error was spread over the whole domain as opposed to a local region and hence uniform refinement actually performed very well in reducing the error in the calculated quantities (solutions of the primal and the dual problems) in the areas of interest. Since after all to have good convergence for the estimated error, ϕ_h^0 and ψ_h^0 have to converge well in the regions of interest. In the current case, although the solution of the primal problem converges well with uniform h-refinement, this is not the case for the solution of the dual problem. As a result the estimated error is condemned to a slow convergence.
Another important point that needs some attention is that if the point of interest falls within the domain of computation, an oscillatory behavior is observed whose severity is dependent on the localization of the regularized delta function. For large enough numbers of elements the oscillations finally die out and convergence is achieved. Some extra results concerning this case are provided in appendix D.

Trial Case 2:

In this case the right hand side of the primal problem is chosen to be:

$$f_2^0 = \begin{cases} 0, & -1 \leqslant x \leqslant 0, \\ -t\pi \sin(t\pi x) - 12\left(\frac{(t\pi)^2}{6} + 1\right) x^2 + (t\pi)^2 x, & 0 < x \leqslant 1, \end{cases} \tag{4.50}$$

where, t is set to 6. The exact solution for this case is:

$$\phi_2^0 = \begin{cases} x + 1, & -1 \leqslant x \leqslant 0, \\ \left(\frac{\sin(t\pi x)}{t\pi}\right) - \left(\frac{(t\pi)^2}{6} + 1\right) x^4 + \frac{(t\pi)^2}{6} x^3 + 1, & 0 < x \leqslant 1. \end{cases} \tag{4.51}$$

Figure 4.6 shows the right hand side and the exact solution. It can be seen that both f_2^0 and its first derivative are continuous in this case. Moreover, due to the more oscillatory behavior of the solution in the regions close to 1 larger error can be expected in these areas.
The right hand side of the dual problem is set to, $\cos(2\pi x)$. The results are shown in Figures 4.7 and 4.8. Figure 4.7 shows that convergence of the effectivity index is fast and reaches higher than 90% for only three elements. Moreover, the error bound is sharp and correctly

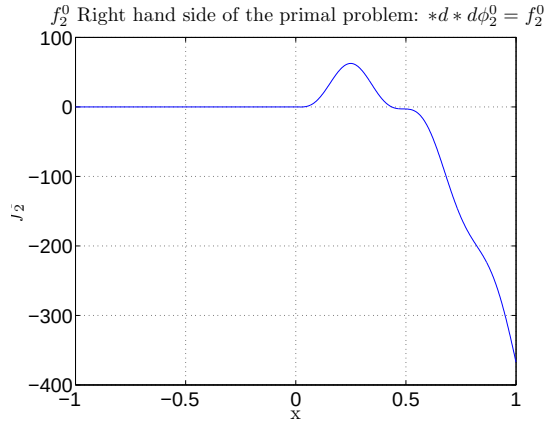

(a) Right hand side of the primal problem f_2^0.

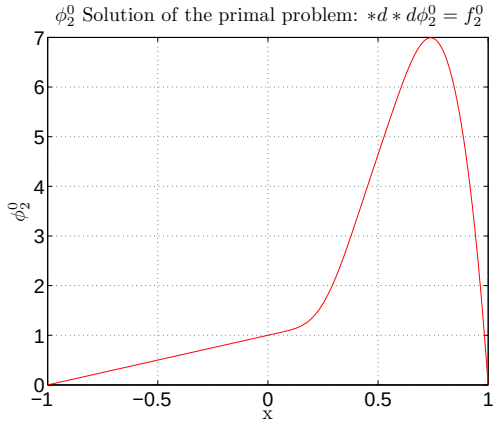

(b) Exact solution of the primal problem ϕ_1^0.

Figure 4.6: The righ hand sides f_1^0 and f_2^0 and the exact solutions ϕ_1^0 and ϕ_2^0.

bounds the estimated and the actual error. From Figure 4.8 it can be seen that the quantity of error on each element is approximated accurately even when low numbers of elements are considered. The good agreement between the estimated and the exact error shows the generality of the method in terms of the choice of the target functional.
Since in this case f_2^0 is not analytic, Gibbs phenomenon can be expected to occur when higher order polynomials are considered. Some extra results concerning this case are provided in appendix (D).

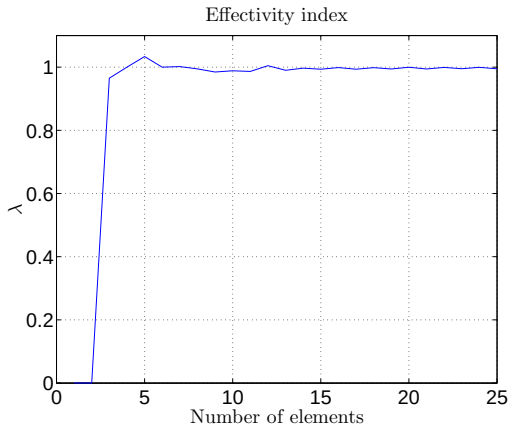

(a) Effectivity index for the case $\star\mathrm{d}\star\mathrm{d}\phi_2^0 = f_2^0$.

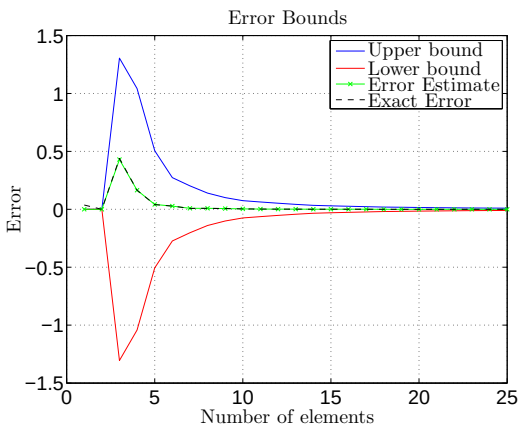

(b) Error bounds for the case $\star\mathrm{d}\star\mathrm{d}\phi_2^0 = f_2^0$.

Figure 4.7: Convergence of the effectivity index and the error bounds for the case $\star\mathrm{d}\star\mathrm{d}\phi_2^0 = f_2^0$.

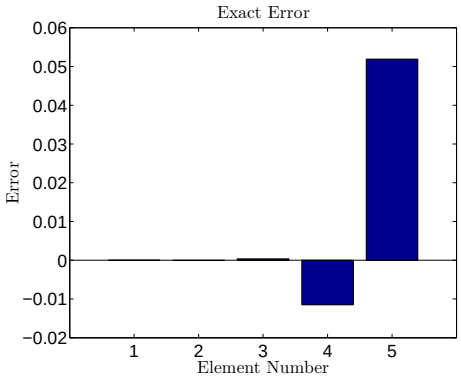

(a) Exact error over each element for 5 elements.

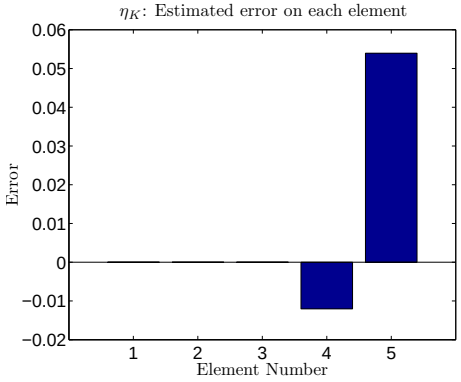

(b) Estimated error over each element for 5 elements.

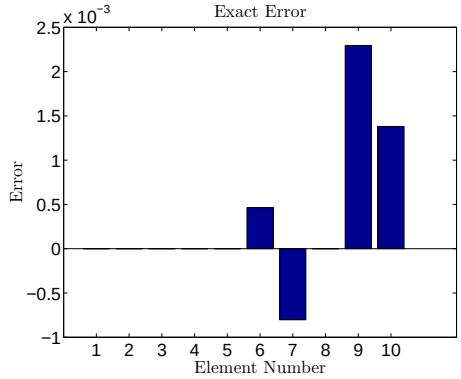

(c) Exact error over each element for 10 elements.

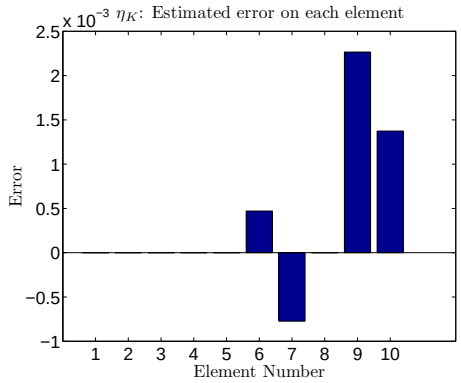

(d) Estimated error over each element for 10 elements.

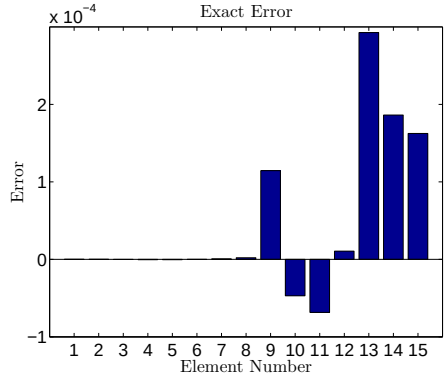

(e) Exact error over each element for 15 elements.

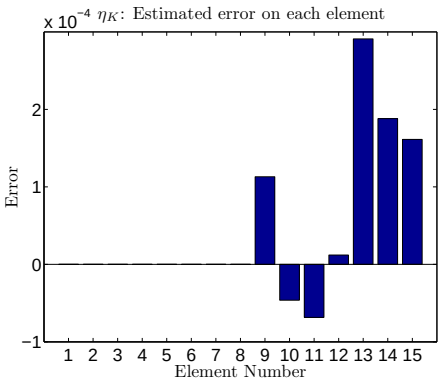

(f) Estimated error over each element for 15 elements.

Figure 4.8: Exact and estimated error for 5, 10, and 15 elements with second order polynomial interpolation for the primal problem.

Trial Case 3: The third and final case in this section is aimed at identifying the limitations of the method presented. In this case the right hand side f_3^0 is chosen to be:

$$f_3^0 = \begin{cases} 0, & -1 \leqslant x \leqslant 0, \\ -6x - 6\pi \sin(6\pi x), & 0 < x \leqslant 1, \end{cases} \tag{4.52}$$

and the corresponding exact solution is:

$$\phi_3^0 = \begin{cases} x + 1, & -1 \leqslant x \leqslant 0, \\ \frac{\sin(6\pi x)}{6\pi} - x^3 + 1, & 0 < x \leqslant 1. \end{cases} \tag{4.53}$$

f_3^0 and ϕ_3^0 are depicted in Figure 4.9.

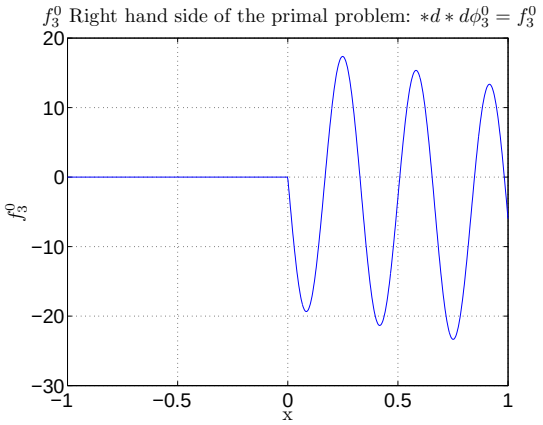

(a) Right hand side of the primal problem f_3^0.

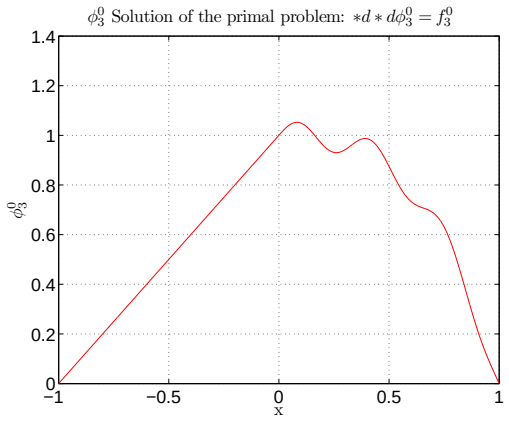

(b) Exact solution of the primal problem ϕ_3^0.

Figure 4.9: The righ hand side f_3^0 and the exact solution ϕ_3^0.

It can be seen that in this case f_3^0 is continuous, while its derivative is not.
Since polynomial basis functions and Gauss-Lobatto quadratures are considered, the inaccuracy in interpolation and integration significantly influence the performance of the error estimator to the point that unstable behavior can be observed for the effectivity index. This oscillatory behavior of the effectivity index together with the corresponding error bounds are depicted in Figure 4.10. From these results it can be seen that for even numbers of elements the estimated error is close to the actual error while for odd numbers of elements the performance of the estimator decreases drastically. Moreover, this drop in performance becomes more severe for larger numbers of elements. Increasing the order of integration will only postpone this drop in performance to larger numbers of elements. This can be seen in Figure 4.11 where the order of integration is increased to 30 orders higher than the order of the solution of the primal problem (improved by 20 compared to the initial case).

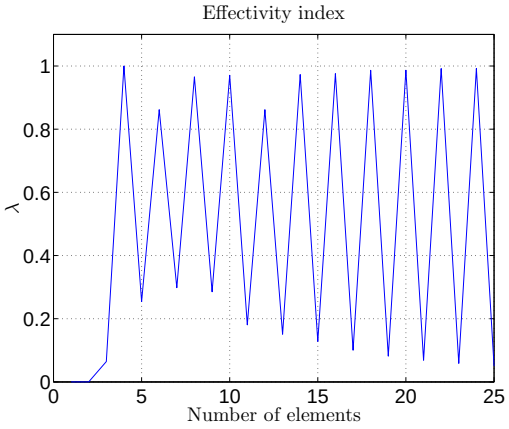

(a) Effectivity index for the case $\star \mathrm{d} \star \mathrm{d}\phi_3^0 = f_3^0$.

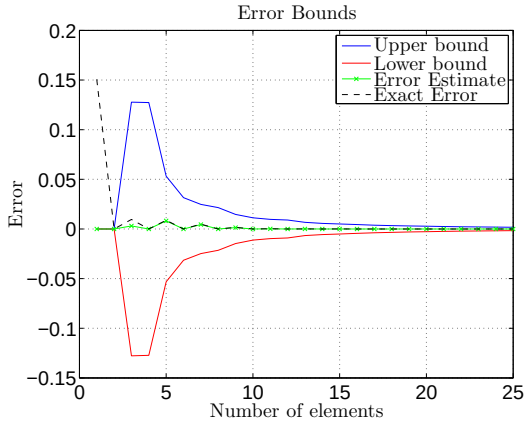

(b) Error bounds for the case $\star \mathrm{d} \star \mathrm{d}\phi_3^0 = f_3^0$.

Figure 4.10: Convergence of the effectivity index and the error bounds for the case $\star \mathrm{d} \star \mathrm{d}\phi_3^0 = f_3^0$.

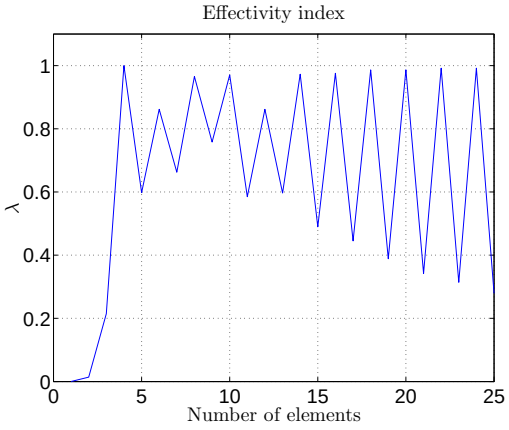

(a) Effectivity index for the case $\star \mathrm{d} \star \mathrm{d}\phi_3^0 = f_3^0$.

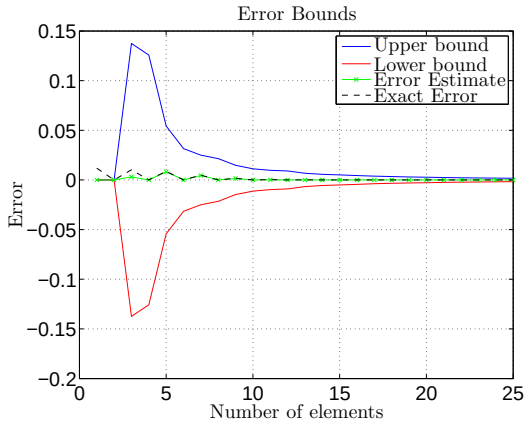

(b) Error bounds for the case $\star \mathrm{d} \star \mathrm{d}\phi_3^0 = f_3^0$.

Figure 4.11: Convergence of the effectivity index and the error bounds for the case $\star \mathrm{d} \star \mathrm{d}\phi_3^0 = f_3^0$ with order of integration set at 32.

Figure 4.12 shows the estimated and the exact error for 15 and 16 elements. It can be seen that for 16 elements an accurate estimate for the error is obtained while for 15 elements the results are disappointing. The reason for this division is that for even numbers of elements, the point of discontinuity of the derivative, $x = 0$, coincides with a Gauss-Lobatto point whereas for odd numbers of elements this point falls in between Gauss-Lobatto nodes. The latter triggers Gibbs phenomenon which can be alleviated by switching the interpolation order to a first order interpolation near the region of discontinuity.

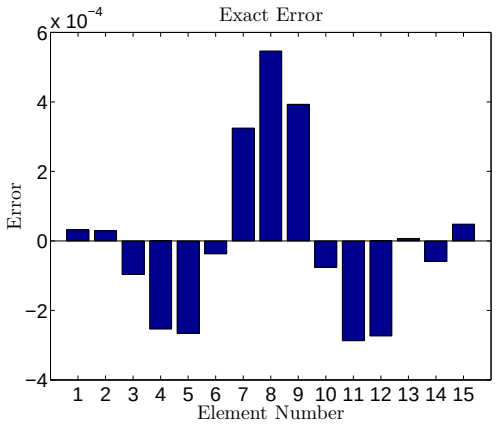

(a) Exact error over each element for 15 elements.

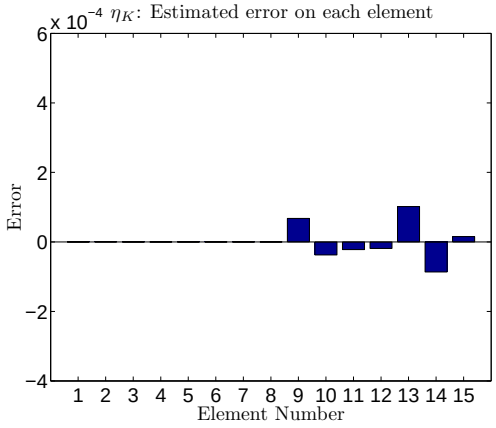

(b) Estimated error over each element for 15 elements.

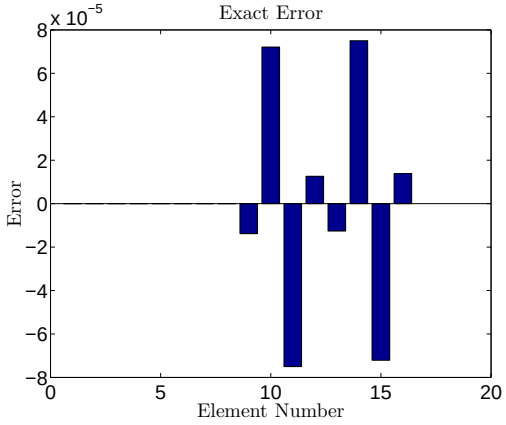

(c) Exact error over each element for 16 elements.

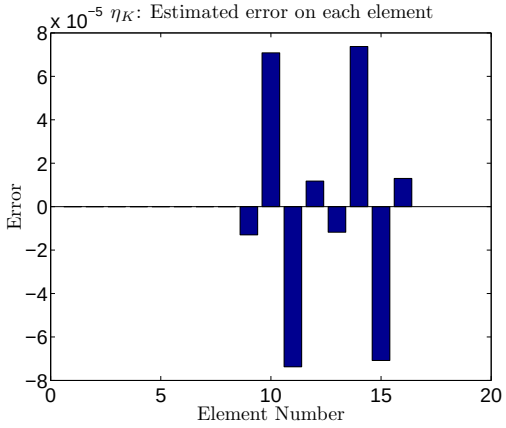

(d) Estimated error over each element for 16 elements.

Figure 4.12: Exact and estimated error for 15 and 16 numbers of elements with second order polynomial interpolation for the primal problem.

Figures 4.13 and 4.14 depict the same results when only first order polynomials are employed for the primal problem. It can be seen that in this case the difference between the estimated error and the actual error is smaller for odd numbers of elements, 5 and 15, and seems to be diminishing for larger numbers of elements. Again good agreement is achieved for even numbers of elements. More information concerning this case is provided in appendix (D).

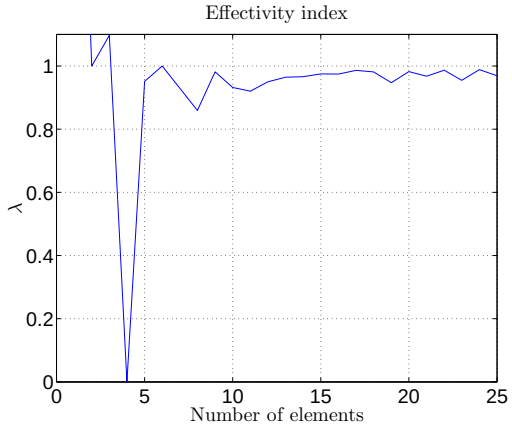

(a) Effectivity index for the case $\star \mathrm{d} \star \mathrm{d}\phi_3^0 = f_3^0$.

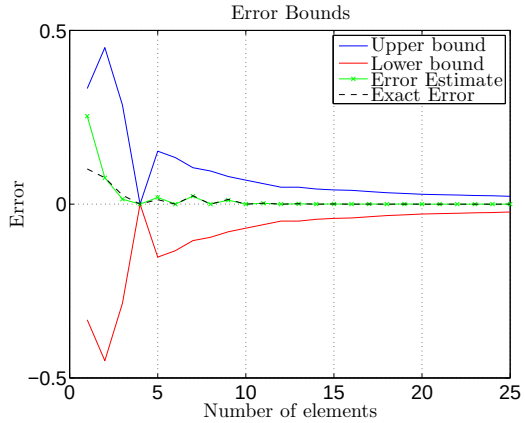

(b) Error bounds for the case $\star \mathrm{d} \star \mathrm{d}\phi_3^0 = f_3^0$.

Figure 4.13: Convergence of the effectivity index and the error bounds for the case $\star \mathrm{d} \star \mathrm{d}\phi_3^0 = f_3^0$ with first order polynomial interpolation.

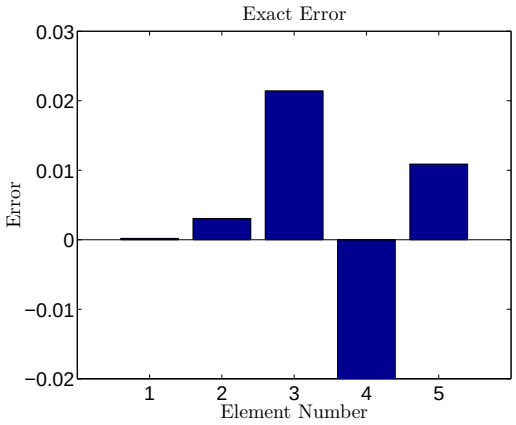

(a) Exact error over each element for 5 elements.

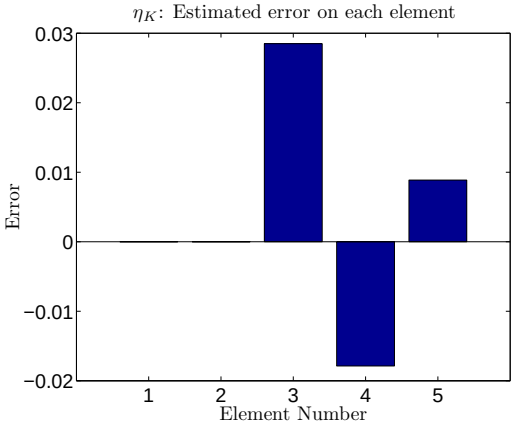

(b) Estimated error over each element for 5 elements.

Figure 4.14: Exact and estimated error for 5, 10, and 15 elements with first order polynomial interpolation for the primal problem.

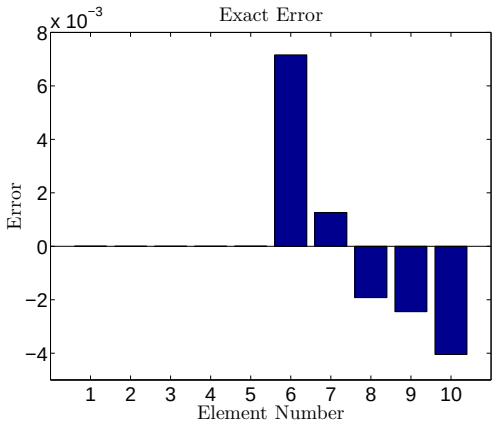

(c) Exact error over each element for 10 elements.

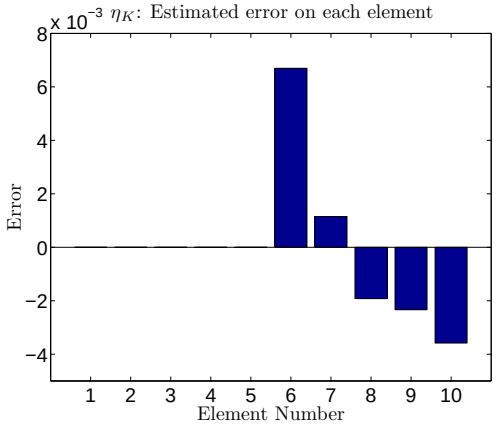

(d) Estimated error over each element for 10 elements.

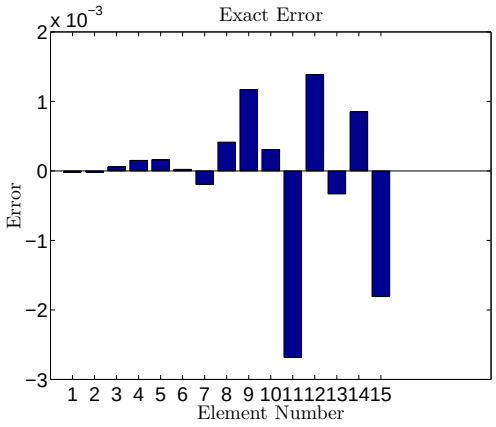

(e) Exact error over each element for 15 elements.

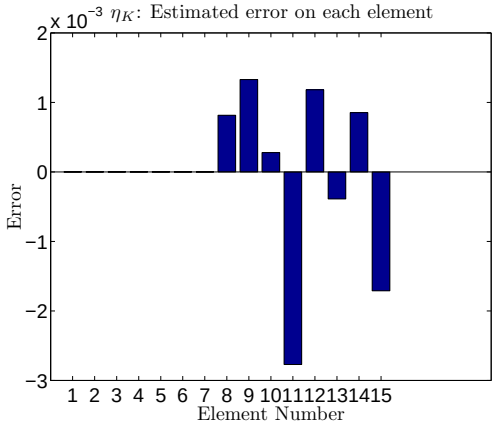

(f) Estimated error over each element for 15 elements.

Figure 4.14: Exact and estimated error for 5, 10, and 15 elements with first order polynomial interpolation for the primal problem.

4.3.4 Concluding Remarks

There are a number of issues that need to be addressed regarding the formulation of the primal and dual problems. These are:

(1) The solution of the dual problem must belong to a polynomial space which is larger than the space spanned by the test functions of the primal problem. This is because throughout the derivations explained in the previous section ψ^0 has been assumed to represent the exact solution to the dual problem. As explained earlier, since in reality the exact solution to the dual equation is not known, one way to deal with this problem

is to solve the dual problem with a higher accuracy than the primal problem. Hence, ψ_h^0 is closer to the exact solution than its projection onto the points of the primal grid, $\pi_h\psi^0$. Now one might wonder why not solve the dual problem with the same order of accuracy as the primal one and simply project the solution onto a coarser grid to obtain $\pi_{\gamma h}\psi^0$, where γ could be 2. This is not done due to Galerkin orthogonality. If the solution of the dual problem belongs to the same space as the test functions of the primal problem then Galerkin orthogonality entails: $\left(R, \psi_h^0 - \pi_{2h}\psi^0\right) = 0$.

(2) From (1) it can be understood that the order of the solution of the dual problem is dependant on the order of the test functions of the primal equation. For the case presented in the previous section this order would be the order of reconstruction of f^0. If this order is lower than the order of the solution of the primal equation, then the dual problem can be solved with the same order as the primal equation for the construction of the dual weighted residual error estimator.

(3) Let, $e^p := \phi^p - \phi_h^p$, be the error in the solution of the primal problem. Then, if the right hand side of the dual problem is chosen to be $e^p/\|e^p\|_{L^2\Lambda^p(\Omega)}$, the functional of interest is the L^2-norm of the error in the solution of the primal problem. However, in practice e^p is not known and must be approximated. This approximation can be achieved by using a higher order interpolation of the solution of the primal problem.

(4) In all the cases discussed here, $\mathrm{d}\pi_h\psi_h^0 = \Pi_h\mathrm{d}\psi_h^0$, holds. Therefore, the good convergence that was observed over each element might be due to this equality.

The results that were presented in the previous section were obtained from second and third order polynomial interpolation for the primal and the dual problems respectively. However, similar results can be obtained using first and second order polynomial interpolations.
Association of physical variables with their underlying geometrical objects sometimes presents problems in a mixed form. This can have some consequences on the derivation of the adjoint problem as explained in (4.27). In the next section these issues will be addressed and a dual weighted residual estimator will be constructed for the mixed formulation of a sample problem.

4.4 Mixed Formulation: Poisson in 1D

Sometimes a multitude of advantages in terms of efficiency and practicality can be gained if mixed formulations are considered as opposed to standard variational methods. In short some of these are:

(1) For some problems, use of standard variational methods is impractical, e.g. Stokes' problem, or Poisson's equation given in appendix C. Therefore, for these problems, mixed methods are usually considered.

(2) It is sometimes the case that the dual variable in the mixed formulation is the main variable of interest. Therefore, it is beneficial to introduce this variable as a fundamental

unknown into the system of equations instead of deriving it *a posteriori*. Mixed formulations offer this possibility. If the geometrical features are respected, it is sometimes possible to construct an exact relation for these unknowns which would otherwise be lost.

(3) Mixed formulation allows for a reduction of the smoothness constraint that must be imposed on the function spaces.

With these motivations it is important to be able to also estimate the error when mixed formulations are considered. To this end, this section is dedicated to the construction of a dual weighted error estimator which can achieve this goal.

4.4.1 Derivation of the Dual problem

To present the method for the construction of an error estimator for mixed problems again Poisson's equation will be considered. Some mixed formulations can be transformed into normal weak formulations and as a result they can be interchanged with their normal counterparts. One such example is the following mixed formulation of the Poisson problem: Find $\left\{\psi^0, u^1\right\} \in H\Lambda^0(\Omega) \times H\Lambda^1(\Omega)$, with [5],

$$\begin{cases} \left(\mathrm{d}\psi^0, e^1\right) = \left(u^1, e^1\right), & x \in \Omega, \quad \forall \ e^1 \in L^2\Lambda^1(\Omega) \\ \left(\star\mathrm{d}\star u^1, h^0\right) = \left(g^0, h^0\right), & x \in \Omega, \quad \forall \ h^0 \in H\Lambda^0(\Omega) \\ \psi^0 = 0, & x \in \partial\Omega. \end{cases} \tag{4.54}$$

(4.54) can be reformulated into

$$\begin{cases} \left(\star\mathrm{d}\star\mathrm{d}\psi^0, h^0\right) = \left(g^0, h^0\right), & x \in \Omega, \quad \forall \ h^0 \in H\Lambda^0(\Omega) \\ \psi^0 = 0, & x \in \partial\Omega, \end{cases} \tag{4.55}$$

by performing integration by parts. To do so one has to start from the second expression in (4.54) and perform integration by parts as follows:

[5] e^1 here represents a test function and should not be confused with error.

$$\begin{aligned}\int_\Omega \mathrm{d}\star u^1\wedge h^0 &= \int_{\partial\Omega}\star u^1\wedge h^0-\int_\Omega u^1\wedge\star\mathrm{d}h^0=\dots\\ \dots &= \int_{\partial\Omega}\star u^1\wedge h^0-\int_\Omega \mathrm{d}\psi^0\wedge\star\mathrm{d}h^0=\dots\\ \dots &= \int_{\partial\Omega}\star u^1\wedge h^0-\int_{\partial\Omega}\star u^1\wedge h^0+\int_\Omega \mathrm{d}\star\mathrm{d}\psi^0\wedge h^0=\dots\\ \dots &= \left(\star\mathrm{d}\star\mathrm{d}\psi^0,h^0\right).\end{aligned}\tag{4.56}$$

Note that in going from the first to the second line one has to use the fact that $\left(\mathrm{d}\psi^0,e^1\right)=\left(u^1,e^1\right)$ is an exact expression and $\mathrm{d}\psi^0-u^1=0$, which in the discrete case becomes $\mathrm{d}\psi_h^0-u_h^1=0$. Therefore, (4.54) and (4.55) are equivalent and can be interchanged in constructing a dual weighted residual error estimator.
While this trick can prove to be useful for some problems it can not be used for all and care must be taken in replacing some unknowns with others. For example in the discrete case, g_h^0 in (4.54) can not be substituted with $\star\mathrm{d}\star u_h^1$, because even though $\star\mathrm{d}\star u^1-g^0=0$, unlike before, $\star\mathrm{d}\star u_h^1-g_h^0\neq 0$.
In contrast to the case that was discussed, there are many mixed problems that can not be transformed into their normal forms as easily. These cases are also important and therefore need to be investigated. To this end, consider the following mixed form of Poisson equation: Find $\left\{\phi^0,\tilde{q}^0\right\}\in H\Lambda^0(\Omega)\times H\Lambda^0(\Omega)$, with,

$$\begin{cases}\left(\star\mathrm{d}\phi^0,\tilde{p}^0\right)=\left(\tilde{q}^0,\tilde{p}^0\right), & x\in\Omega,\quad\forall\ \tilde{p}^0\in H\Lambda^0(\Omega)\\ \left(\mathrm{d}\tilde{q}^0,\tilde{\psi}^1\right)=\left(\tilde{f}^1,\tilde{\psi}^1\right), & x\in\Omega,\quad\forall\ \tilde{\psi}^1\in H\Lambda^1(\Omega)\\ \phi^0=0, & x\in\partial\Omega.\end{cases}\tag{4.57}$$

Adding the first and the second equations yields the following mixed formulation for the primal problem: Find $\left\{\phi^0,\tilde{q}^0\right\}\in H\Lambda^0(\Omega)\times H\Lambda^0(\Omega)$, with,

$$\begin{cases}\left(\star\mathrm{d}\phi^0,\tilde{p}^0\right)-\left(\tilde{q}^0,\tilde{p}^0\right)+\left(\mathrm{d}\tilde{q}^0,\tilde{\psi}^1\right)=\left(\tilde{f}^1,\tilde{\psi}^1\right), & x\in\Omega,\\ \phi^0=0, & x\in\partial\Omega,\end{cases}\tag{4.58}$$

$\forall\left\{\tilde{\psi}^1,\tilde{p}^0\right\}\in H\Lambda^1(\Omega)\times H\Lambda^0(\Omega)$.
To obtain the dual problem to (4.58) the same procedure introduced in the previous section is followed. Starting from (4.58) integration by parts is performed until all the operators are passed onto the test functions. The resulting dual problem is: Find $\left\{\tilde{\psi}^1,\tilde{p}^0\right\}\in H\Lambda^1(\Omega)\times$

$H\Lambda^0(\Omega)$, with,

$$\begin{cases} -\left(\phi^0, \star \mathrm{d}\tilde{p}^0\right) - \left(\tilde{q}^0, \tilde{p}^0\right) - \left(\tilde{q}^0, \star \mathrm{d} \star \tilde{\psi}^1\right) = \left(g^0, \phi^0\right), & x \in \Omega, \\ \star\tilde{\psi}^1 = 0, & x \in \partial\Omega, \end{cases} \tag{4.59}$$

$\forall \left\{\phi^0, \tilde{q}^0\right\} \in H\Lambda^0(\Omega) \times H\Lambda^0(\Omega)$.
(4.59) is the dual problem to (4.58). It is worth mentioning that this procedure is not specific to this problem and can be used to obtain the dual of any problem proposed in mixed form. (4.59) will be used in the next section to construct a dual weighted residual error estimator.

4.4.2 Derivation of an Adjoint Error Estimator

Consider the following discrete primal and dual problems from previous section: Find $\left\{\phi_h^0, \tilde{q}_h^0\right\} \in \Lambda_h^0(\Omega) \times \widehat{\Lambda}_h^0(\Omega)$, with,

$$\begin{cases} \left(\star \mathrm{d}\phi_h^0, \tilde{h}^0\right) - \left(\tilde{q}_h^0, \tilde{h}^0\right) + \left(\mathrm{d}\tilde{q}_h^0, \tilde{e}^1\right) = \left(\tilde{f}^1, \tilde{e}^1\right), & x \in \Omega, \\ \phi_h^0 = 0, & x \in \partial\Omega, \end{cases} \tag{4.60}$$

$\forall \left\{\tilde{e}^1, \tilde{h}^0\right\} \in \Lambda_h^1(\Omega) \times \widehat{\Lambda}_h^0(\Omega)$, and, find $\left\{\tilde{\psi}_h^1, \tilde{p}_h^0\right\} \in \bar{\Lambda}_h^1(\Omega) \times \bar{\Lambda}_h^0(\Omega)$, with,

$$\begin{cases} -\left(m^0, \star \mathrm{d}\tilde{p}_h^0\right) - \left(\tilde{n}^0, \tilde{p}_h^0\right) - \left(\tilde{n}^0, \star \mathrm{d} \star \tilde{\psi}_h^1\right) = \left(g^0, m^0\right), & x \in \Omega, \\ \star\tilde{\psi}_h^1 = 0, & x \in \partial\Omega, \end{cases} \tag{4.61}$$

$\forall \left\{m^0, \tilde{n}^0\right\} \in \widehat{\Lambda}_h^0(\Omega) \times \bar{\Lambda}_h^0(\Omega)$, where, $\Lambda_h^1(\Omega) \subset \bar{\Lambda}_h^1(\Omega) \subset H\Lambda^1(\Omega)$, and $\Lambda_h^0(\Omega) \subset \widehat{\Lambda}_h^0(\Omega) \subset \bar{\Lambda}_h^0(\Omega) \subset H\Lambda^0(\Omega)$.
To construct the error estimator corresponding to (4.60) and (4.61) the following target functional is considered:

$$J(\left\{\phi^0, \tilde{q}^0\right\}) = \int_\Omega g^0 \wedge \star\phi^0. \tag{4.62}$$

The error in this target functional can be written as:

$$J(\left\{\phi^0, \tilde{q}^0\right\}) - J(\left\{\phi_h^0, \tilde{q}_h^0\right\}) = \int_\Omega g^0 \wedge \star\phi^0 - \int_\Omega g^0 \wedge \star\phi_h^0. \tag{4.63}$$

Using (4.58) and performing integration by parts, (4.62) becomes:

$$\begin{aligned} J(\{\phi^0, \tilde{q}^0\}) &= \int_\Omega g^0 \wedge \star\phi^0 = -\left(\phi^0, \star \mathrm{d}\tilde{p}^0\right) - \left(\tilde{q}^0, \tilde{p}^0\right) - \left(\tilde{q}^0, \star \mathrm{d} \star \tilde{\psi}^1\right) = \dots \\ \dots &= -\int_{\partial\Omega} \tilde{q}^0 \wedge \star\tilde{\psi}^1 + \int_\Omega \mathrm{d}\tilde{q}^0 \wedge \star\tilde{\psi}^1 - \int_\Omega \tilde{q}^0 \wedge \star\tilde{p}^0 - \dots \\ \dots &- \int_{\partial\Omega} \phi^0 \wedge \tilde{p}^0 + \int_\Omega \mathrm{d}\phi^0 \wedge \tilde{p}^0. \end{aligned} \tag{4.64}$$

Now employing the boundary conditions in (4.58) and (4.59) yields:

$$J(\{\phi^0, \tilde{q}^0\}) = \int_\Omega \mathrm{d}\tilde{q}^0 \wedge \star\tilde{\psi}^1 - \int_\Omega \tilde{q}^0 \wedge \star\tilde{p}^0 + \int_\Omega \mathrm{d}\phi^0 \wedge \tilde{p}^0. \tag{4.65}$$

Similarly, for the approximated target functional one has:

$$J(\{\phi_h^0, \tilde{q}_h^0\}) = \int_\Omega \mathrm{d}\tilde{q}_h^0 \wedge \star\tilde{\psi}^1 - \int_\Omega \tilde{q}_h^0 \wedge \star\tilde{p}^0 + \int_\Omega \mathrm{d}\phi_h^0 \wedge \tilde{p}^0. \tag{4.66}$$

Subtracting (4.66) from (4.65) gives:

$$\begin{aligned} J(\{\phi^0, \tilde{q}^0\}) - J(\{\phi_h^0, \tilde{q}_h^0\}) &= \int_\Omega \mathrm{d}(\tilde{q}^0 - \tilde{q}_h^0) \wedge \star\tilde{\psi}^1 - \int_\Omega \star(\tilde{q}^0 - \tilde{q}_h^0) \wedge \tilde{p}^0 + \dots \\ \dots &+ \int_\Omega \mathrm{d}(\phi^0 - \phi_h^0) \wedge \tilde{p}^0. \end{aligned} \tag{4.67}$$

Since both ϕ^0 and $\tilde{q}^0$ are considered to be exact, $\mathrm{d}\phi^0 = \star\tilde{q}^0$ holds, and therefore can be eliminated from (4.67). Moreover, $\mathrm{d}\tilde{q}^0 = \tilde{f}^1$. Therefore, the following expression for the error in the target functional can be obtained:

$$J(\{\phi^0, \tilde{q}^0\}) - J(\{\phi_h^0, \tilde{q}_h^0\}) = \int_\Omega (\tilde{f}^1 - \mathrm{d}\tilde{q}_h^0) \wedge \star\tilde{\psi}^1 + \int_\Omega (\tilde{q}_h^0 - \star\mathrm{d}\phi_h^0) \wedge \star\tilde{p}^0. \tag{4.68}$$

An important point to notice here is that although $\mathrm{d}\tilde{q}_h^0$ is exact the first integral on the right hand side in (4.68) need not be zero. If $\tilde{f}^1$ belongs to a polynomial space larger than the one to which $\mathrm{d}\tilde{q}_h^0$ belongs, then in order to subtract the latter from the former, $\mathrm{d}\tilde{q}_h^0$ must be sent to a larger polynomial space. As a result the first integral on the right hand side in (4.68) picks up the error in interpolation.
Considering (4.60) and a discrete solution for the dual problem, the following Galerkin orthogonality holds:

$$\left(\tilde{f}^1 - \mathrm{d}\tilde{q}_h^0, \pi_h\tilde{\psi}^1\right) + \left(\tilde{q}_h^0 - \star\mathrm{d}\phi_h^0, \pi_h\tilde{p}^0\right) = 0, \quad \forall \ \left\{\pi_h\tilde{\psi}^1, \pi_h\tilde{p}^0\right\} \in \Lambda_h^1(\Omega) \times \widehat{\Lambda}_h^0(\Omega). \tag{4.69}$$

$\pi_h\tilde{\psi}^1$ and $\pi_h\tilde{p}^0$ are mimetic projections of $\tilde{\psi}_h^1$ and $\tilde{p}_h^0$ onto the polynomial spaces of $\tilde{e}^1$ and $\tilde{h}^0$ respectively. Using (4.69) the error in the target functional becomes:

$$\begin{aligned} J(\{\phi^0, \tilde{q}^0\}) - J(\{\phi_h^0, \tilde{q}_h^0\}) &= \int_\Omega (\tilde{f}^1 - \mathrm{d}\tilde{q}_h^0) \wedge \star(\tilde{\psi}_h^1 - \pi_h\tilde{\psi}^1) + \dots \\ \dots &+ \int_\Omega (\tilde{q}_h^0 - \star\mathrm{d}\phi_h^0) \wedge \star(\tilde{p}_h^0 - \pi_h\tilde{p}^0). \end{aligned} \tag{4.70}$$

Once again partitioning the domain Ω into elements Ω_K and using an approximated dual solution yield:

$$\begin{aligned} & J(\{\phi^0, \tilde{q}^0\}) - J(\{\phi_h^0, \tilde{q}_h^0\}) \approx \sum_K \eta_K = \dots \\ \dots &= \sum_K \left\{ \int_{\Omega_K} (\tilde{f}^1 - \mathrm{d}\tilde{q}_h^0) \wedge \star(\tilde{\psi}_h^1 - \pi_h\tilde{\psi}^1) + \int_{\Omega_K} (\tilde{q}_h^0 - \star\mathrm{d}\phi_h^0) \wedge \star(\tilde{p}_h^0 - \pi_h\tilde{p}^0) \right\} \end{aligned} \tag{4.71}$$

which can be used to construct the following approximate bound for the error:

$$
\begin{aligned}
& |J(\{\phi^0, \tilde{q}^0\}) - J(\{\phi_h^0, \tilde{q}_h^0\})| \leqslant \dots \\
\dots \quad = \quad & \sum_K \left\{ \int_{\Omega_K} |(\tilde{f}^1 - \mathrm{d}\tilde{q}_h^0) \wedge \star(\tilde{\psi}_h^1 - \pi_h \tilde{\psi}^1) + (\tilde{q}_h^0 - \star \mathrm{d}\phi_h^0) \wedge \star(\tilde{p}_h^0 - \pi_h \tilde{p}^0)| \right\}. \quad (4.72)
\end{aligned}
$$

In the next section the results obtained from a dual weighted residual error estimator constructed following (4.71) will be discussed.

4.4.3 Results for Mixed Poisson Equation in 1D

To test the performance of the error estimator and the error bound introduced in (4.71) and (4.72) a number of test cases will be considered. Moreover, the order of integration for the dual and primal problems are set to ten orders higher than the polynomial order of $\tilde{q}^0$ in the primal problem. The order of polynomial interpolation for the primal problem is set to two and the dual problem is solved with one order higher. The grids used for solving these problems are of Gauss and Gauss-Lobatto types and are depicted in Figure 4.15.

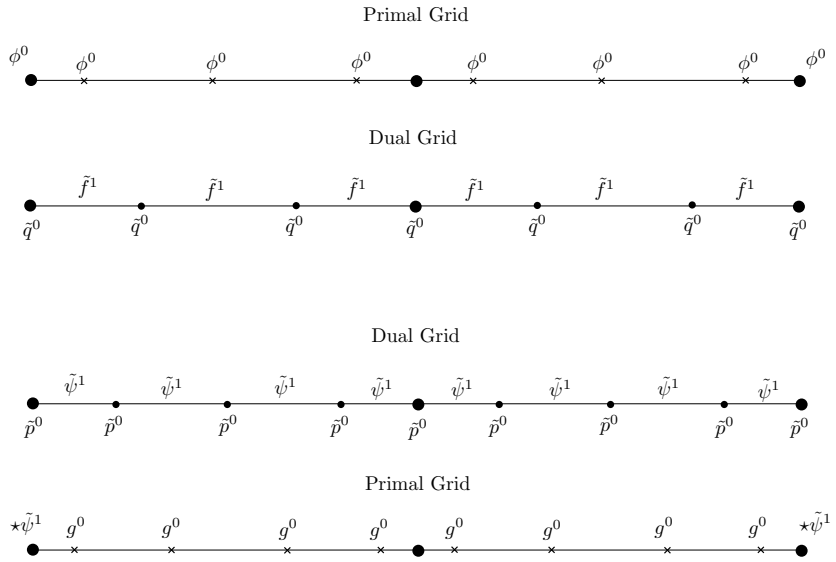

Figure 4.15: Grids used for solving the primal and the dual problems.

The following paragraphs state the test cases and discuss the results.

Trial Case 4:

The primal and dual problems in this case are:

$$\text{Primal problem} \begin{cases} \star \mathrm{d}\phi^0 = \tilde{q}^0, & x \in \Omega, \\ \mathrm{d}\tilde{q}^0 = \tilde{f}^1, & x \in \Omega, \\ \phi^0 = 0, & x \in \partial\Omega, \end{cases} \tag{4.73}$$

and,

$$\text{Dual problem} \begin{cases} \star \mathrm{d} \star \tilde{\psi}^1 = \tilde{p}^0, & x \in \Omega, \\ \star \mathrm{d}\tilde{p}^0 = \cos(2\pi x), & x \in \Omega, \\ \star\tilde{\psi}^1 = 0, & x \in \partial\Omega, \end{cases} \tag{4.74}$$

where,

$$\tilde{f}^1 = \left(-9\cos(3e^x)\cdot e^{2x} - 3e^x \cdot \sin(3e^x)\right)\, \mathrm{d}x, \tag{4.75}$$

and is a smooth function. The exact solution, ϕ^0, is:

$$\phi^0 = \cos(3e^x) + \left[\frac{\cos(3e) + \cos(3e^{(-1)})}{2} - \cos(3e)\right] x - \frac{\cos(3e) + \cos(3e^{(-1)})}{2}. \tag{4.76}$$

Figure 4.16 shows the right hand side, (4.75), and the exact solution, (4.76).

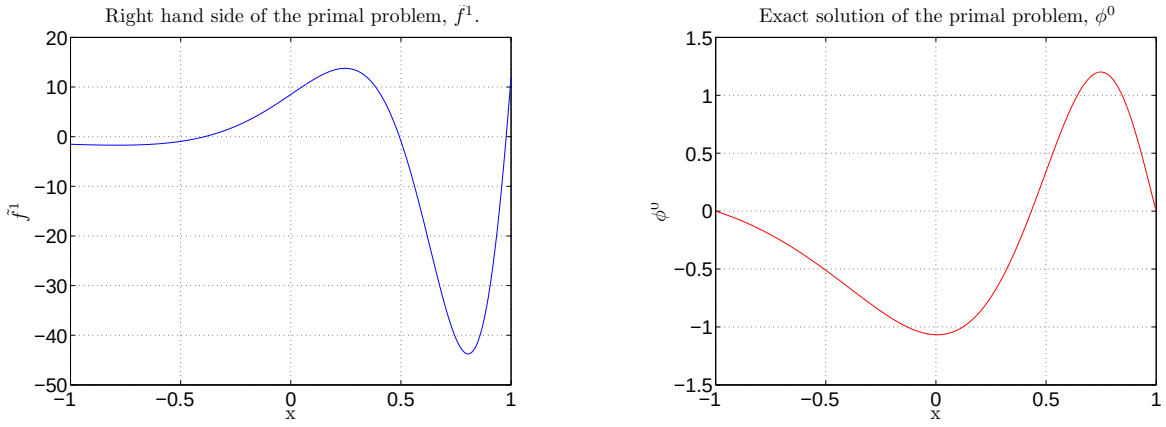

(a) Right hand side of the primal problem, $\tilde{f}^1$.

(b) Exact solution of the primal problem, ϕ^0_1.

Figure 4.16: The righ hand side $\tilde{f}^1$ and the exact solutions ϕ^0.

The results for this case are depicted in Figures 4.17 and 4.18.
Figure 4.17 shows that the effectivity index reaches 95% when only three elements are considered. Moreover, it can be seen that the error bounds tightly bound the exact and the approximated error as the number of elements is increased. Figure 4.18 shows good agreement between the exact and estimated error over each element. The oscillatory behavior of the functions in the regions close to 1 in Figure 4.16 suggests higher error in these areas. Indeed the results shown in Figure 4.18 meet this expectation. Since all functions are smooth in this case, Gibbs phenomenon is absent. Appendix D contains some extra information concerning this case.

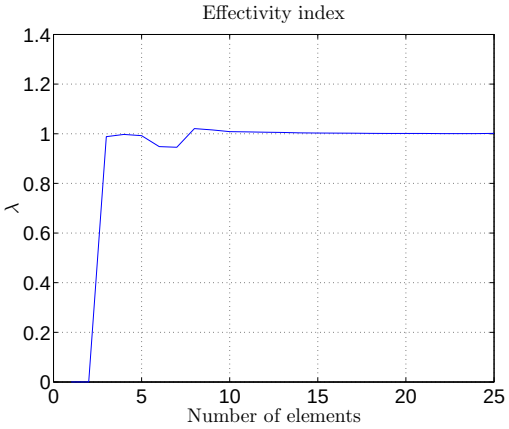

(a) Effectivity index.

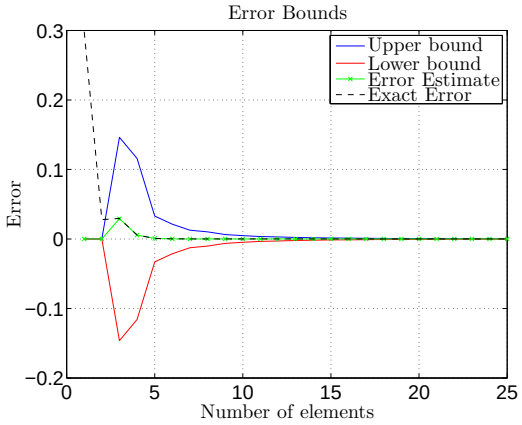

(b) Error bounds.

Figure 4.17: Convergence of the effectivity index and the error bounds for case 1.

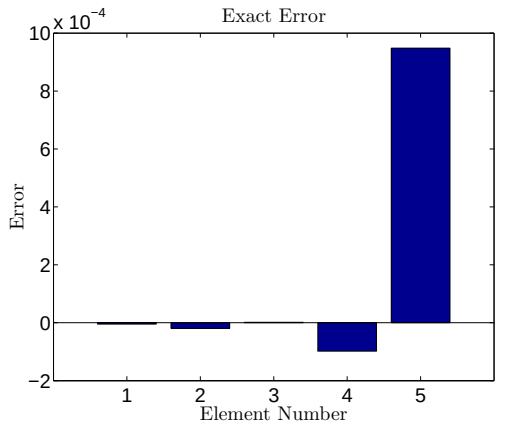

(a) Exact error over each element for 5 elements.

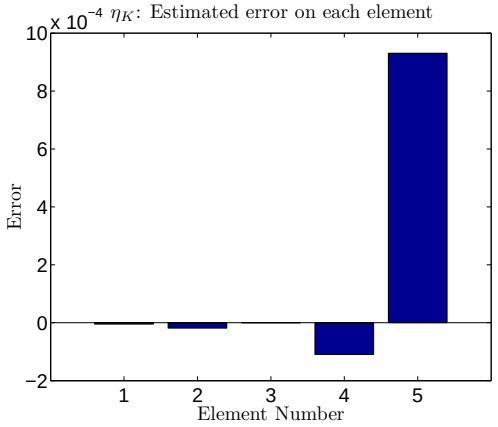

(b) Estimated error over each element for 5 elements.

Figure 4.18: Exact and estimated error for 5, 10, and 15 elements with second order polynomial interpolation for the primal problem.

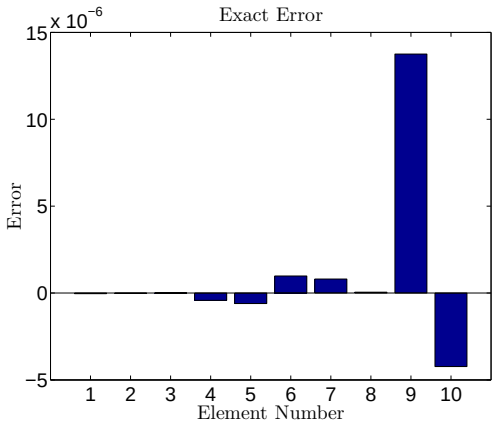

(c) Exact error over each element for 10 elements.

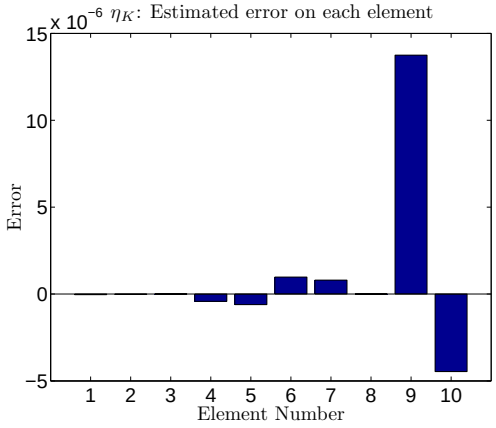

(d) Estimated error over each element for 10 elements.

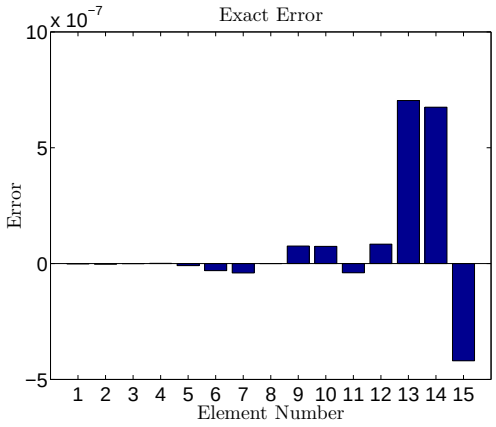

(e) Exact error over each element for 15 elements.

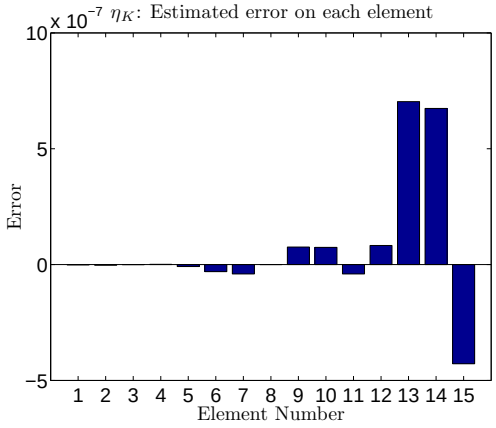

(f) Estimated error over each element for 15 elements.

Figure 4.18: Exact and estimated error for 5, 10, and 15 elements with second order polynomial interpolation for the primal problem.

Trial Case 5:

In this case again as in the trial case 1 in the previous section, the regularized delta function is considered as the right hand side of the dual problem. The primal and dual problems are:

$$\text{Primal problem} \begin{cases} \star \mathrm{d}\phi^0 = \tilde{q}^0, & x \in \Omega, \\ \mathrm{d}\tilde{q}^0 = \cos(2\pi x)\ \mathrm{d}x, & x \in \Omega, \\ \phi^0 = 0, & x \in \partial\Omega, \end{cases} \tag{4.77}$$

and,

$$\text{Dual problem} \begin{cases} \star \mathrm{d} \star \tilde{\psi}^1 = \tilde{p}^0, & x \in \Omega, \\ \star \mathrm{d} \tilde{p}^0 = e^{-500|x-1|}, & x \in \Omega, \\ \star \tilde{\psi}^1 = 0, & x \in \partial\Omega. \end{cases} \tag{4.78}$$

The results are depicted in Figures 4.19 and 4.20. It can be seen that the effectivity index overshoots 1 after seven elements and reaches approximately 1.17 for 10 elements. After this point it starts to converge slowly towards 1. One can expedite this convergence by increasing the polynomial orders. The error bounds accurately bound the exact and approximated error and follow these quantities towards zero. Figure 4.20 shows that the error estimator correctly estimates the highest error to occur on the element on the boundary at 1. More information concerning this case is provided in appendix D.

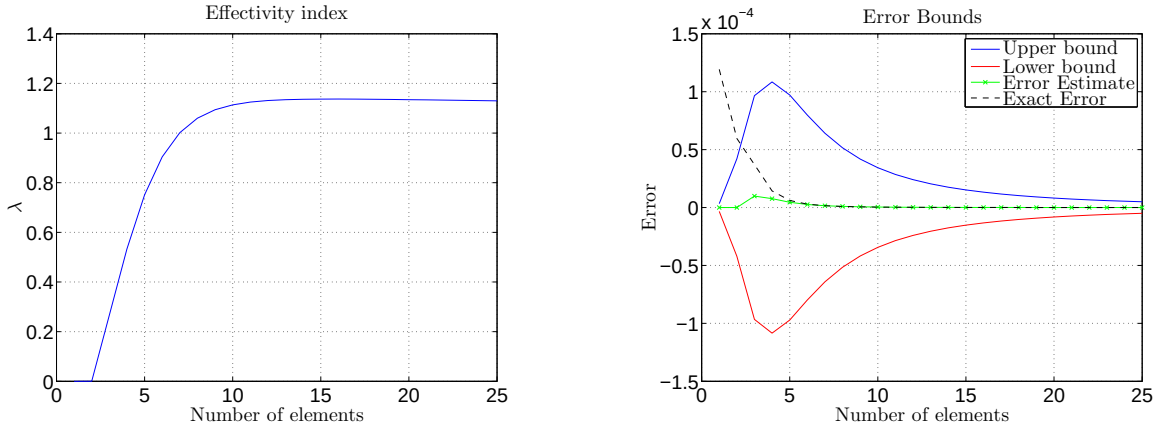

(a) Effectivity index.

(b) Error bounds.

Figure 4.19: Convergence of the effectivity index and the error bounds for case 2.

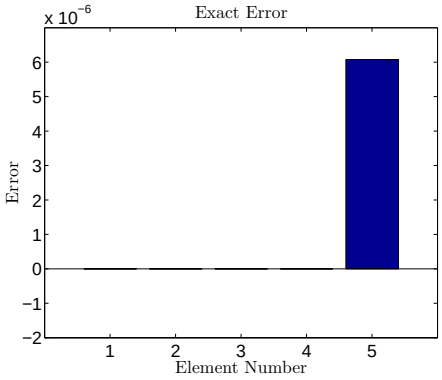

(a) Exact error over each element for 5 elements.

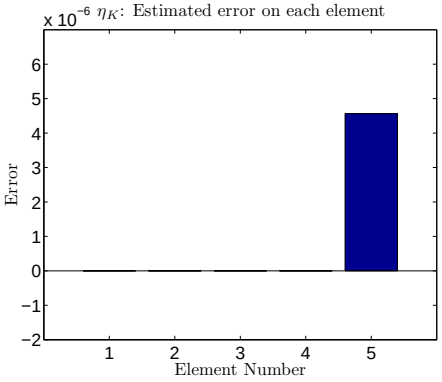

(b) Estimated error over each element for 5 elements.

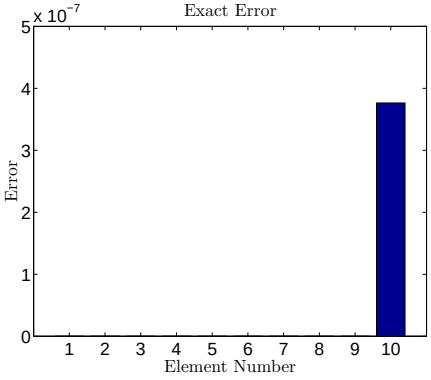

(c) Exact error over each element for 10 elements.

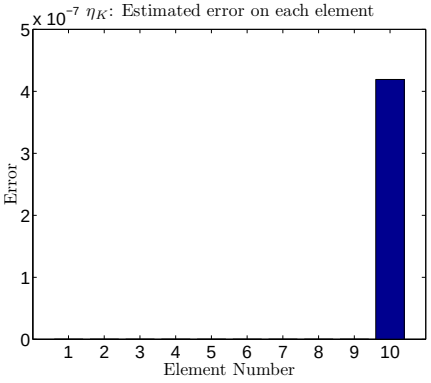

(d) Estimated error over each element for 10 elements.

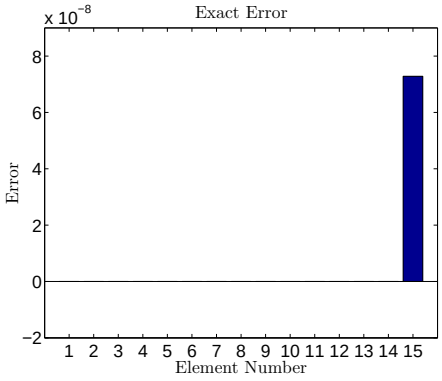

(e) Exact error over each element for 15 elements.

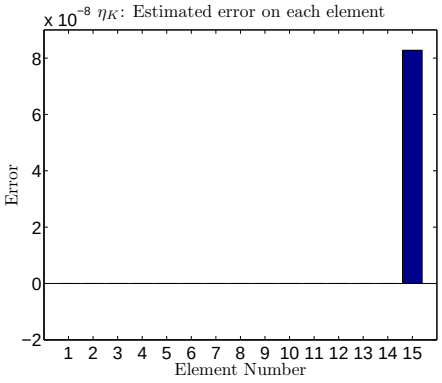

(f) Estimated error over each element for 15 elements.

Figure 4.20: Exact and estimated error for 5, 10, and 15 elements with second order polynomial interpolation for the primal problem.

Trial Case 6: In this case the same right hand side as for the trial case 3 in the previous section is considered. The primal and dual problems are:

$$\text{Primal problem} \begin{cases} \star \mathrm{d}\phi^0 = \tilde{q}^0, & x \in \Omega, \\ \mathrm{d}\tilde{q}^0 = \tilde{f}^1, & x \in \Omega, \\ \phi^0 = 0, & x \in \partial\Omega, \end{cases} \tag{4.79}$$

$$\text{Dual problem} \begin{cases} \star \mathrm{d} \star \tilde{\psi}^1 = \tilde{p}^0, & x \in \Omega, \\ \star \mathrm{d}\tilde{p}^0 = \cos(2\pi x), & x \in \Omega, \\ \star\tilde{\psi}^1 = 0, & x \in \partial\Omega, \end{cases} \tag{4.80}$$

where,

$$\tilde{f}^1 = \begin{cases} 0, & -1 \leqslant x \leqslant 0, \\ (-6x - 6\pi \sin(6\pi x))\ \mathrm{d}x, & 0 < x \leqslant 1, \end{cases} \tag{4.81}$$

and the corresponding exact solution is:

$$\phi^0 = \begin{cases} x + 1, & -1 \leqslant x \leqslant 0, \\ \frac{\sin(6\pi x)}{6\pi} - x^3 + 1, & 0 < x \leqslant 1. \end{cases} \tag{4.82}$$

The effectivity index and error bounds are depicted in Figure 4.21 when second order polynomials are used for the primal problem. Again as for the case 3 in the previous section, the presence of Gibbs phenomenon is apparent from the oscillatory behavior of the effectivity index. Decreasing the order of interpolation to 1 results in Figures 4.22 and 4.23. It can be seen that when first order polynomials are employed, the effectivity index falls within approximately $\pm 10\%$ range of 1 after 7 elements. The error bounds tightly bound the exact and the approximated error and approach zero as these quantities converge. Finally, Figure 4.23 shows that there is good agreement between the exact error on each element and the corresponding approximated error quantity. Some extra results concerning this case are provided in appendix D.

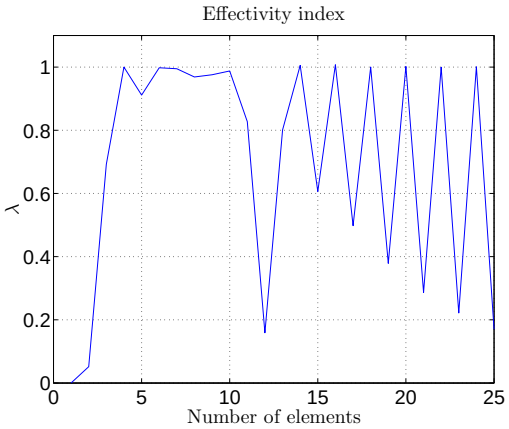

(a) Effectivity index.

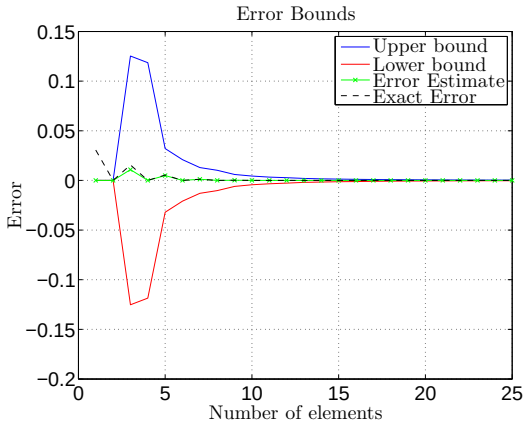

(b) Error bounds.

Figure 4.21: Convergence of the effectivity index and the error bounds for case 3. Second order polynomial interpolation for the primal problem is considered.

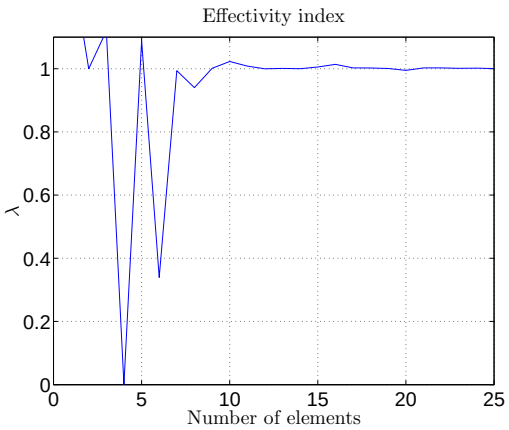

(a) Effectivity index.

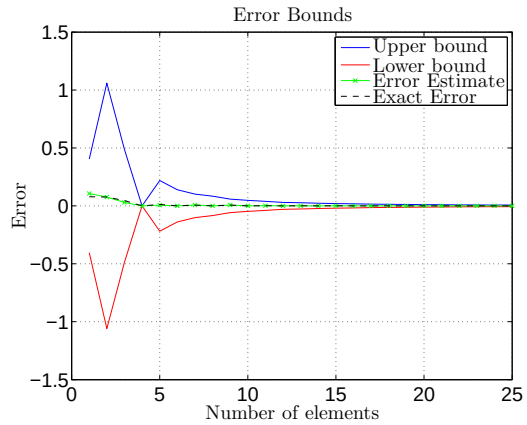

(b) Error bounds.

Figure 4.22: Convergence of the effectivity index and the error bounds for case 3. First order polynomial interpolation for the primal problem is considered.

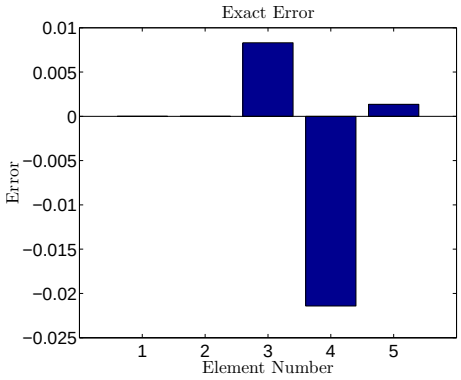

(a) Exact error over each element for 5 elements.

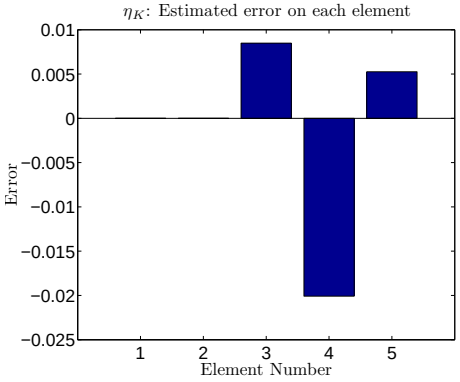

(b) Estimated error over each element for 5 elements.

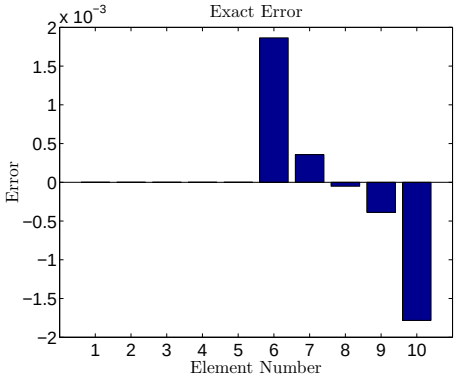

(c) Exact error over each element for 10 elements.

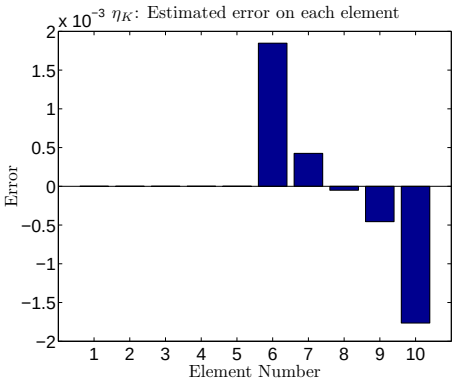

(d) Estimated error over each element for 10 elements.

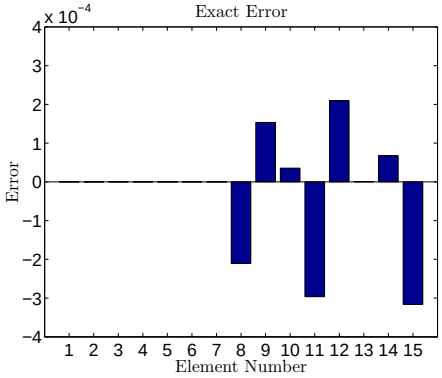

(e) Exact error over each element for 15 elements.

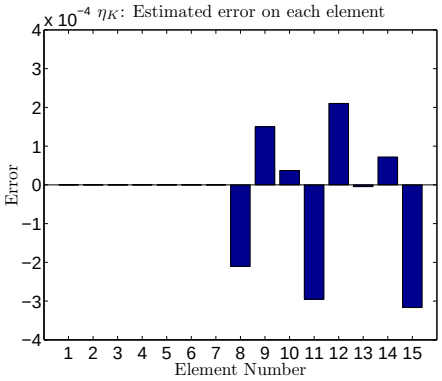

(f) Estimated error over each element for 15 elements.

Figure 4.23: Exact and estimated error for 5, 10, and 15 elements with first order polynomial interpolation for the primal problem.

4.5 Standard Variational Method: Poisson in 2D

In this section the procedure that was introduced in section 4.3 will be extended to 2D and a number of test cases will be discussed. As before the focus will be on the Poisson problem.

4.5.1 Derivation of the Dual Problem

The mathematical procedure involved in the derivation of the dual problem is very similar to the case discussed in section 4.3.1. However, due to subtle differences that might arise in extending the computations from lower dimensions to higher ones, it might be beneficial to present the step by step derivations. To this end, consider again the primal Poisson problem,

$$\begin{cases} \star \mathrm{d} \star \mathrm{d}\phi^0 = f^0, & x, y \in \Omega, \\ \phi^0 = 0, & x, y \in \partial\Omega. \end{cases} \tag{4.83}$$

and target functional,

$$J(\phi^0) = \int_\Omega g^0 \wedge \star\phi^0. \tag{4.84}$$

where, $\phi^0 \in H\Lambda^0(\Omega)$, and f^0 belongs an appropriate space such that the primal problem accepts unique solutions.
Now the adjoint problem can be derived by multiplying the primal problem with a test function and performing integration by parts. To do so, let $\psi^0 \in H\Lambda^0(\Omega)$. Multiplying (4.83) by ψ^0 and integrating by parts yields:

$$\begin{aligned} \left(\star \mathrm{d} \star \mathrm{d}\phi^0, \psi^0\right) &= \int_\Omega \psi^0 \wedge \mathrm{d} \star \mathrm{d}\phi^0 = \int_\Omega \star \mathrm{d}\phi^0 \wedge \mathrm{d}\psi^0 = -\left(\mathrm{d}\psi^0, \mathrm{d}\phi^0\right) = \dots \\ \dots &= -\int_\Omega \mathrm{d}\phi^0 \wedge \star \mathrm{d}\psi^0 = \int_\Omega \phi^0 \wedge \mathrm{d} \star \mathrm{d}\psi^0 = \left(\phi^0, \star \mathrm{d} \star \mathrm{d}\psi^0\right). \end{aligned} \tag{4.85}$$

The dual problem to (4.83) can be written as:

$$\begin{cases} \star \mathrm{d} \star \mathrm{d}\psi^0 = g^0, & x, y \in \Omega, \\ \psi^0 = 0, & x, y \in \partial\Omega. \end{cases} \tag{4.86}$$

In the next section (4.83), (4.84), and (4.86) will be used to derive a dual weighted residual error estimator.

4.5.2 Derivation of an Adjoint Error Estimator

The expression for the exact quantity of interest can be written as:

$$J(\phi^0) = \left(g^0, \phi^0\right) = -\left(\mathrm{d}\psi^0, \mathrm{d}\phi^0\right) = \left(\psi^0, f^0\right). \tag{4.87}$$

Let $\phi_h^0 \in \Lambda_h^0(\Omega)$, then the approximated quantity of interest can be written as:

$$J(\phi_h^0) = \left(g^0, \phi_h^0\right) = -\left(\mathrm{d}\psi^0, \mathrm{d}\phi_h^0\right). \tag{4.88}$$

Subtracting (4.88) from (4.87) yields:

$$J(\phi^0) - J(\phi_h^0) = \left(\psi^0, f^0\right) + \left(\mathrm{d}\psi^0, \mathrm{d}\phi_h^0\right). \tag{4.89}$$

Let ψ_h^0 be the Ritz projection of the exact solution to the dual problem onto a polynomial space larger than $\Lambda_h^0(\Omega)$. Moreover, let $\pi_h\psi^0$ be the mimetic projection of ψ_h^0 onto the polynomial space $\Lambda_h^0(\Omega)$. Then using Galerkin orthogonality one has:

$$\begin{aligned} J(\phi^0) - J(\phi_h^0) &= \left(\psi_h^0 - \pi_h\psi^0, f^0\right) + \left(\mathrm{d}\psi_h^0 - \mathrm{d}\pi_h\psi^0, \mathrm{d}\phi_h^0\right) = \dots \\ \dots &= \int_\Omega \left(\psi^0 - \pi_h\psi^0\right) \wedge \star f^0 + \int_\Omega \mathrm{d}\left(\psi^0 - \pi_h\psi^0\right) \wedge \star \mathrm{d}\phi_h^0. \end{aligned} \tag{4.90}$$

(4.90) can be divided into elemental contributions to the global error as follows:

$$J(\phi^0) - J(\phi_h^0) = \sum_K \left\{ \int_{\Omega_K} \left(\psi^0 - \pi_h\psi^0\right) \wedge \star f^0 + \int_{\Omega_K} \mathrm{d}\left(\psi^0 - \pi_h\psi^0\right) \wedge \star \mathrm{d}\phi_h^0 \right\}. \tag{4.91}$$

Using (4.91) the following bound for the error in the quantity of interest can be constructed.

$$|J(\phi^0) - J(\phi_h^0)| \leqslant \sum_K \left\{ \int_{\Omega_K} |\left(\psi^0 - \pi_h\psi^0\right) \wedge \star f^0 + \mathrm{d}\left(\psi^0 - \pi_h\psi^0\right) \wedge \star \mathrm{d}\phi_h^0| \right\}. \tag{4.92}$$

In the next section, (4.91) will be used to approximate the error in the target functional for a number of test cases.

4.5.3 Results for Poisson Equation in 2D

To test the performance of (4.91), a number of test cases will be investigated. Two effectivity indices are considered. These are:

$$\lambda_1 = \frac{|\sum_K \eta_K|}{|\sum_K \{\int_{\Omega_K} (\star\phi^0 \wedge g^0) - (\star\phi_h^0 \wedge g^0)\}|}. \tag{4.93}$$

and,

$$\lambda_2 = \frac{\sum_K |\eta_K|}{\sum_K |\int_{\Omega_K} (\star\phi^0 \wedge g^0) - (\star\phi_h^0 \wedge g^0)|}. \tag{4.94}$$

In all test cases the order of polynomial interpolation for the primal and the dual problems is set to 1 and 2 respectively. The order of integration for the two problems are set to five orders higher than the order of interpolation of the solution of the dual problem. The same order is used for the reduction and integration of the exact solution and exact functional respectively. The domain of computation is $[-1, 1] \times [-1, 1]$ and uniform h-refinement is used in all cases. The grids used for solving these problems are of Gauss-Lobatto type and are depicted in Figure 4.24.

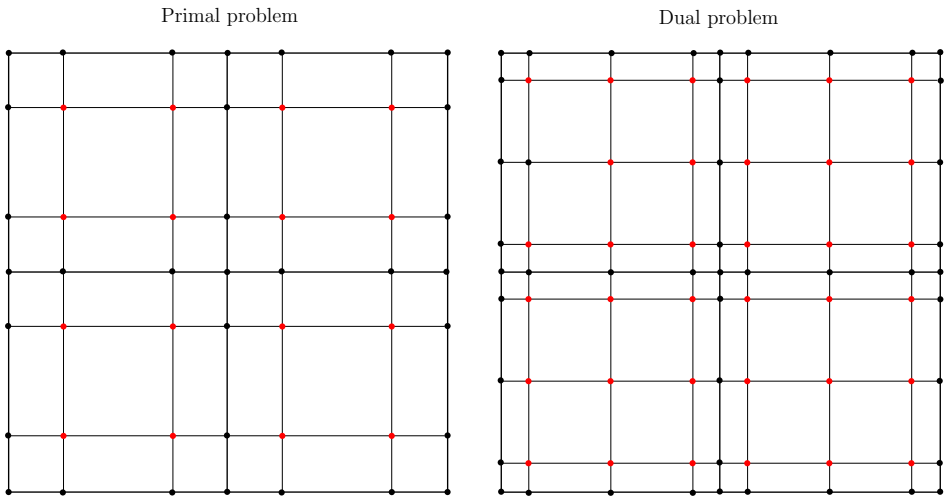

Figure 4.24: Gauss-Lobatto grids used for solving the primal and the dual problems.

The following paragraphs discuss the results.

Trial Case 7: The primal and dual problems in this case are:

$$\begin{cases} \star \mathrm{d} \star \mathrm{d}\phi^0 = -2(t\pi)^2 \sin(t\pi x)\cos(t\pi y) - (t\pi)^2 \sin(t\pi x), & x, y \in \Omega, \\ \phi^0 = 0, & x, y \in \partial\Omega. \end{cases} \tag{4.95}$$

$$\begin{cases} \star \mathrm{d} \star \mathrm{d}\psi^0 = -2(t\pi)^2 \sin(t\pi x)\cos(t\pi y) - (t\pi)^2 \sin(t\pi x), & x, y \in \Omega, \\ \psi^0 = 0, & x, y \in \partial\Omega. \end{cases} \tag{4.96}$$

where, $t = 5$. The exact solution is:

$$\phi^0 = \psi^0 = \sin(t\pi x)\cos(t\pi y) + \sin(t\pi x). \tag{4.97}$$

The right hand side and the exact solution are depicted in Figure 4.25.

The results are depicted in Figures 4.26, 4.27, and 4.28.
Figure 4.26 depicts the two effectivity indices and the error bounds. It can be seen that λ_1 falls within the 5% bound of 1 only after 36 elements and stays in this region. λ_2 on the other shows a more irregular behavior and even though stays close to 1 throughout the refinement to 900 elements, it seems that it is diverging for larger numbers of elements. Moreover, it can be seen that the error bound tightly bounds the exact and approximated error and approaches

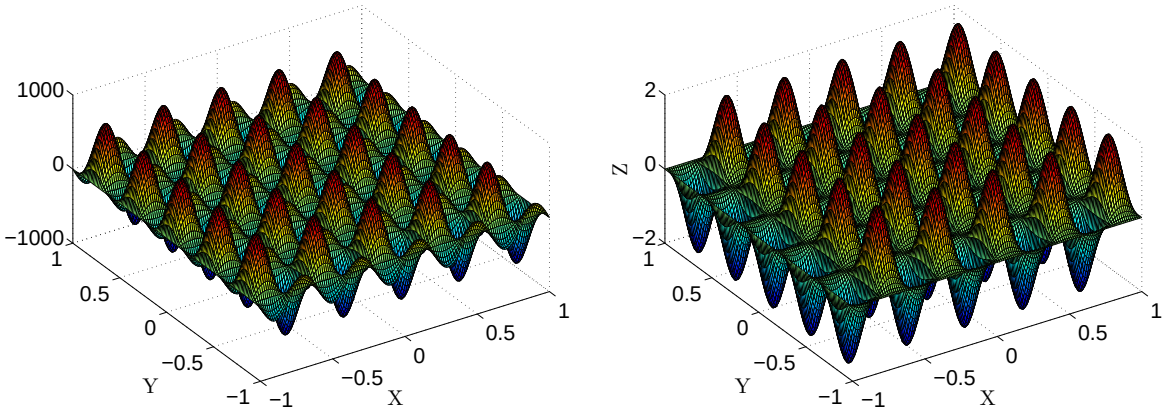

(a) Right hand side of the primal and dual problems.

(b) Exact solution of the primal and dual problems.

Figure 4.25: The right hand side and the exact solution of the primal and dual problems.

zero as these quantities converge. Since,

$$\sum_K |\eta_K| \leqslant \sum_K \left\{ \int_{\Omega_K} |\left(\psi^0 - \pi_h\psi^0\right) \wedge \star f^0 + \mathrm{d}\left(\psi^0 - \pi_h\psi^0\right) \wedge \star \mathrm{d}\phi_h^0| \right\}, \tag{4.98}$$

convergence of the error bound suggests that λ_2 will eventually converge to 1 for larger numbers of elements. That is if the error bound itself continues to converge towards zero. It is important to realize that when λ_2 is considered, due to the appearance of the absolute value inside the summation, the expression, $\left(\pi_h\psi^0, f^0\right) + \left(\mathrm{d}\pi_h\psi^0, \mathrm{d}\phi_h^0\right)$, which used to be zero due to Galerkin orthogonality, begins to contribute to the total amount of error estimated. Therefore, changing the construction of the error estimator such that Galerkin orthogonality holds on each individual element might be beneficial.
Figure 4.27 depicts the evolution of estimated error on each element as the number of elements is increased. It can be seen that the largest contributions to the global error are picked up much better by the error estimator. Figure 4.28 gives a 3D view of the error over each element when 900 elements are considered.

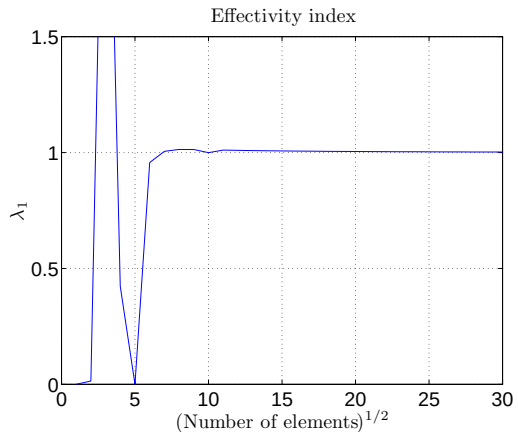

(a)

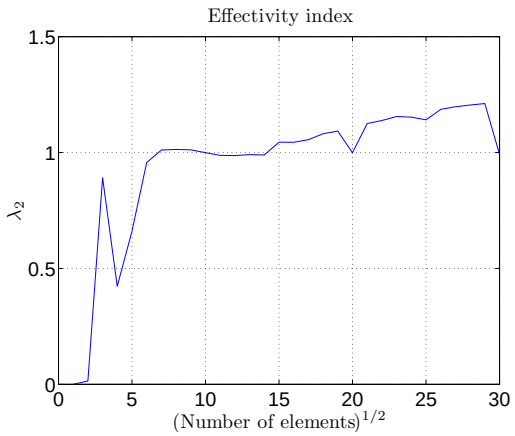

(b)

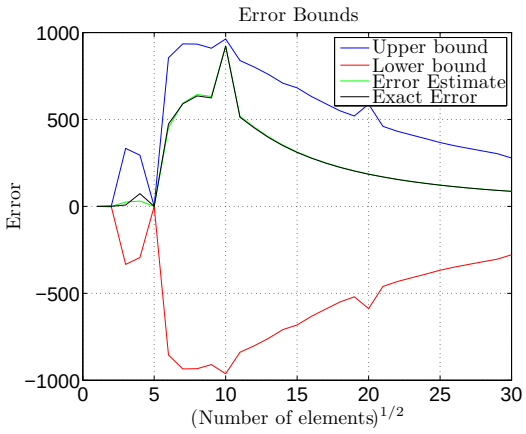

(c)

Figure 4.26: Effectivity indices and error bounds.

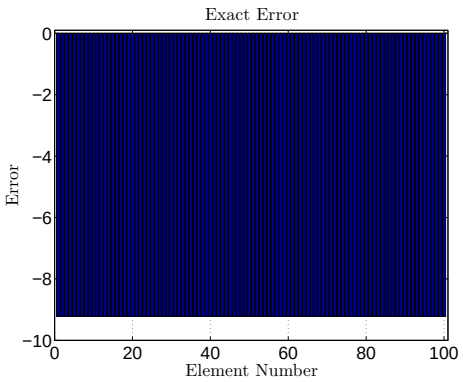

(a) Exact error over each element for 100 elements.

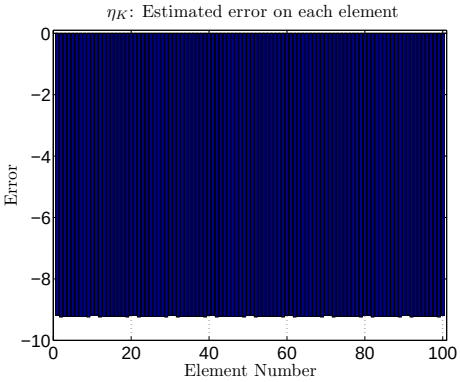

(b) Estimated error over each element for 100 elements.

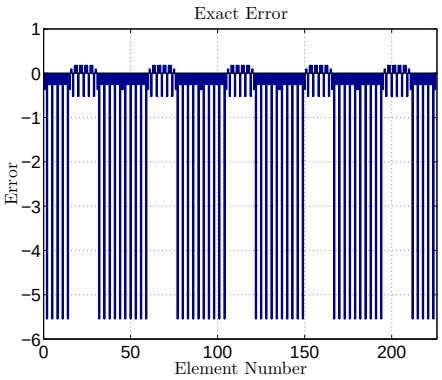

(c) Exact error over each element for 225 elements.

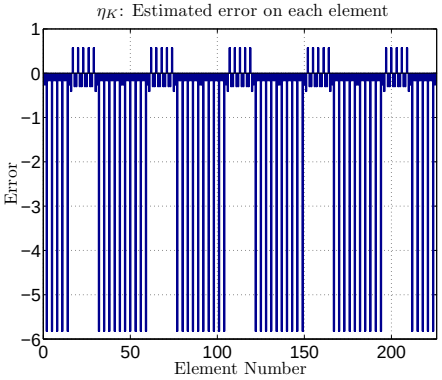

(d) Estimated error over each element for 225 elements.

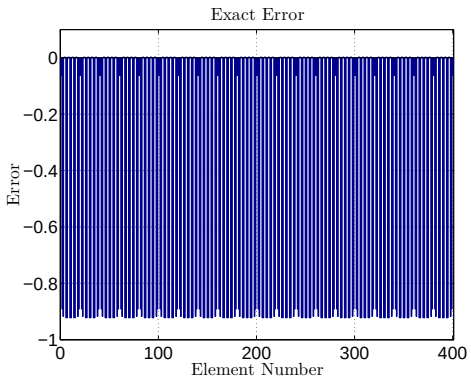

(e) Exact error over each element for 400 elements.

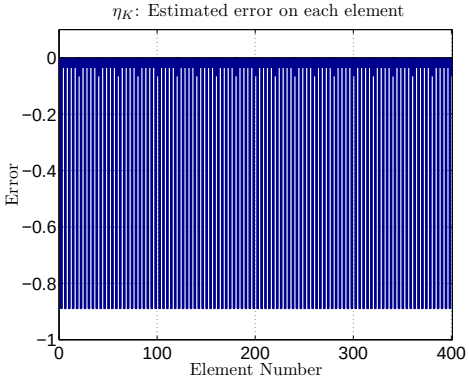

(f) Estimated error over each element for 400 elements.

Figure 4.27: Exact and estimated error for 100, 225, and 400 elements.

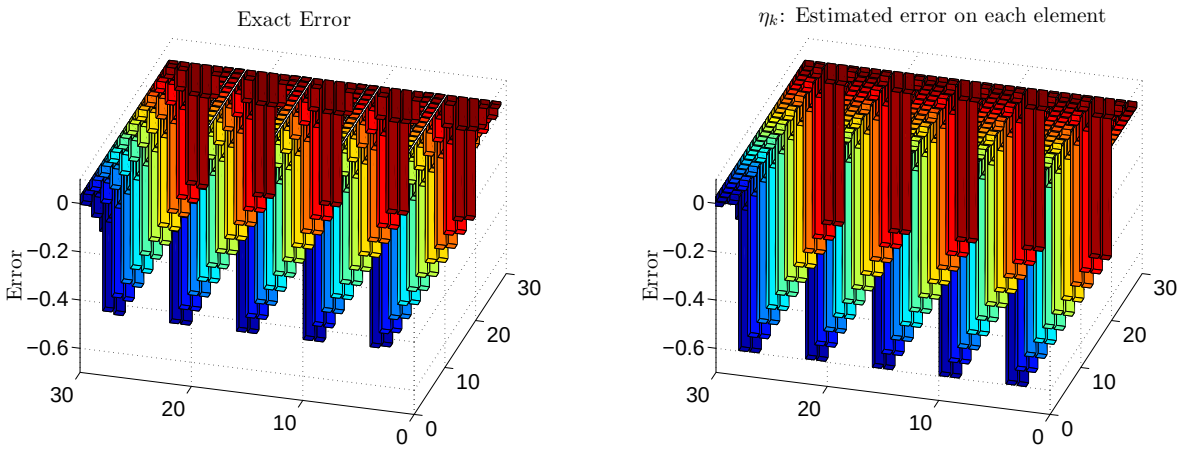

(a) (b)

Figure 4.28: Exact and estimated error over each element for 900 elements.

Trial Case 8:

The second example was first introduced in [36] and later reiterated in [31]. The primal and dual problems in this case read:

$$\begin{cases} \star \mathrm{d} \star \mathrm{d}\phi^0 = f^0, & x, y \in \Omega, \\ \phi^0 = 0, & x, y \in \partial\Omega. \end{cases} \tag{4.99}$$

$$\begin{cases} \star \mathrm{d} \star \mathrm{d}\psi^0 = g^0, & x, y \in \Omega, \\ \psi^0 = 0, & x, y \in \partial\Omega. \end{cases} \tag{4.100}$$

where,

$$\begin{aligned} f &= \left(-2\sin(t\pi x) - (4t\pi x)\cos(t\pi x) - (t\pi)^2(1-x^2)\sin(t\pi x)\right)(1-y^2)\sin(t\pi y) + \dots \\ \dots &+ \left(-2\sin(t\pi y) - (4t\pi y)\cos(t\pi y) - (t\pi)^2(1-y^2)\sin(t\pi y)\right)(1-x^2)\sin(t\pi x), \end{aligned} \tag{4.101}$$

and $t = 4$. g^0 in this case is chosen such that the functional of interest reads:

$$J(\phi^0) = \frac{1}{|S|}\int_S \phi^0 \wedge \star 1, \quad S = [-1/2, 0] \times [0, 1/2]\,. \tag{4.102}$$

The exact solution to the primal problem is:

$$\phi^0 = (1 - x^2)(1 - y^2)\sin(t\pi x)\sin(t\pi y). \tag{4.103}$$

Figure 4.29 depicts the right hand side and the exact solution.

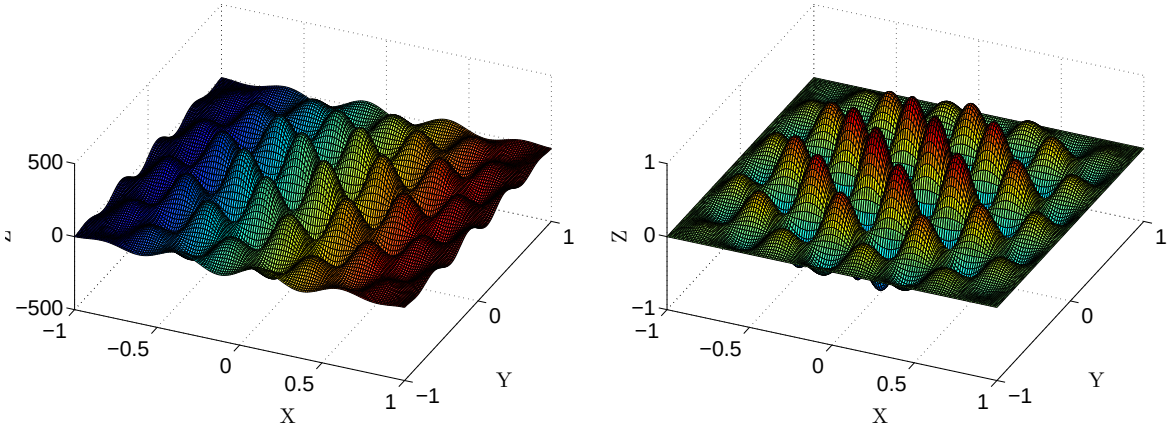

(a) Right hand side of the primal problem.

(b) Exact solution of the primal problem.

Figure 4.29: The right hand side and the exact solution of the primal problem.

The results are depicted in Figures 4.30, 4.31, and 4.32.
From Figure 4.30, it can be seen that after 400 elements λ_1 falls within 5% bound of 1 and converges to this value. It appears that λ_2 is diverging and for 900 elements it reaches the value 2.08. The error bounds correctly bound the estimated and exact error and converge towards zero. Again as in the previous case, if the error bounds continue to converge towards zero, one can come to the conclusion that λ_2 will eventually converge.
Figure 4.31 shows the estimated and exact error for 100, 225, and 400 elements. It can be seen that the largest contributions to the global error are made by the elements within the sub-domain S. This is depicted more vividly in Figure 4.32, where a 3D view of the estimated and exact error for 900 elements is given. An interesting point to notice here is that, among all the elements that are located on the corners of the sub-domain S, the one which is closest to the boundary of the domain contributes the most and the one which is the furthest from the boundaries of the domain contributes the least to the global error. The corners with the same distance to the boundaries contribute the same amount.
The results from [31] are given in Table 4.1. These results have been obtained on sequences of locally refined meshes based on an error indicator similar to (4.91). It can be seen that there is reasonable agreement between the values of λ_1 as presented in [31] and the results obtained from uniform refinement performed in this work. However, it can be seen that there is a large discrepancy between the values of the mean error, $J(\phi - \phi_h)$. This might be due to the differences in the numerical methods employed.

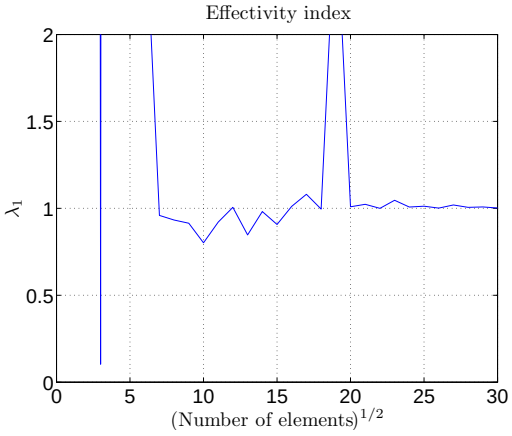

(a)

(b)

(c)

Figure 4.30: Effectivity indices and error bounds.

# Elements	$J(\phi - \phi_h)$	λ_1	# Elements	$J(\phi - \phi_h)$	λ_1	λ_2
81	$7.6 \cdot 10^{-2}$	1.01	81	$2.2 \cdot 10^{-3}$	0.91	1.27
151	$2.7 \cdot 10^{-2}$	1.00	144	$-8.1 \cdot 10^{-4}$	1.00	1.61
653	$3.6 \cdot 10^{-3}$	0.99	625	$-9.0 \cdot 10^{-5}$	1.01	2.02
1435	$1.4 \cdot 10^{-3}$	1.00	1369	$-5.3 \cdot 10^{-5}$	1.00	2.13

Table 4.1: Effectivity of error indicator for the mean error $J(\phi - \phi_h)$, as presented in [31], left, and, as obtained in the current work, right.

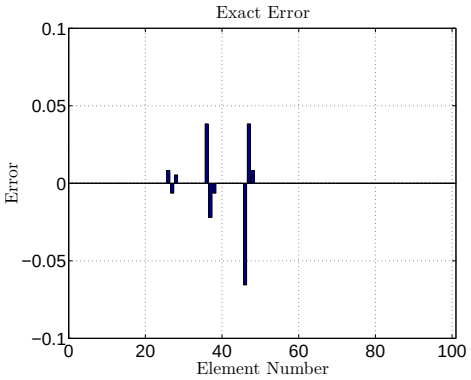

(a) Exact error over each element for 100 elements.

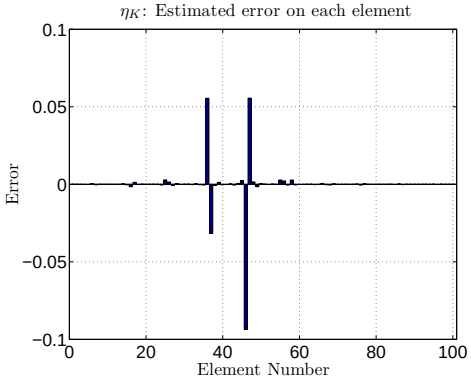

(b) Estimated error over each element for 100 elements.

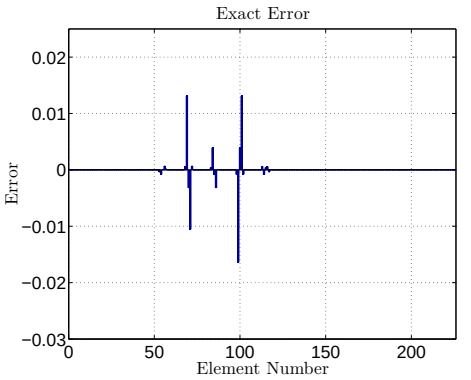

(c) Exact error over each element for 225 elements.

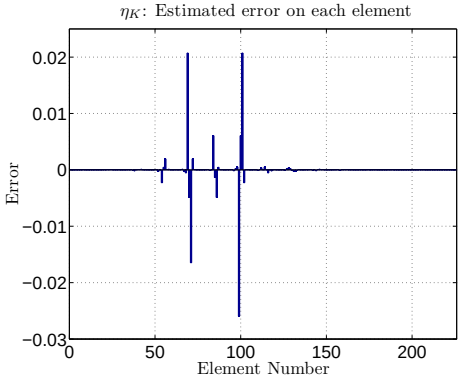

(d) Estimated error over each element for 225 elements.

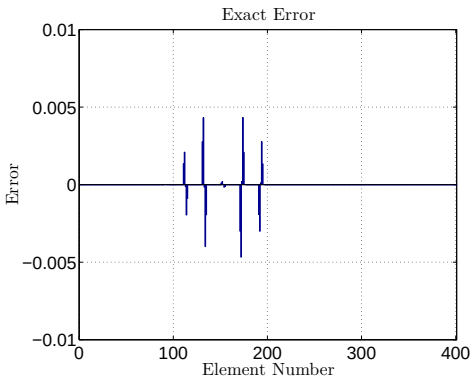

(e) Exact error over each element for 400 elements.

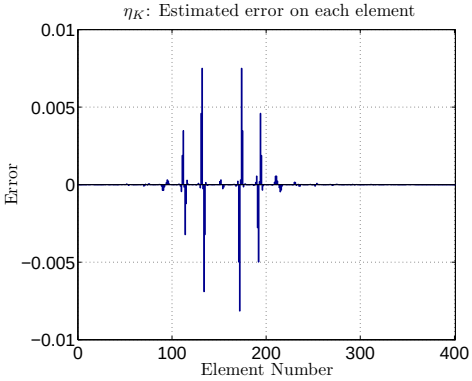

(f) Estimated error over each element for 400 elements.

Figure 4.31: Exact and estimated error for 100, 225, and 400 elements.

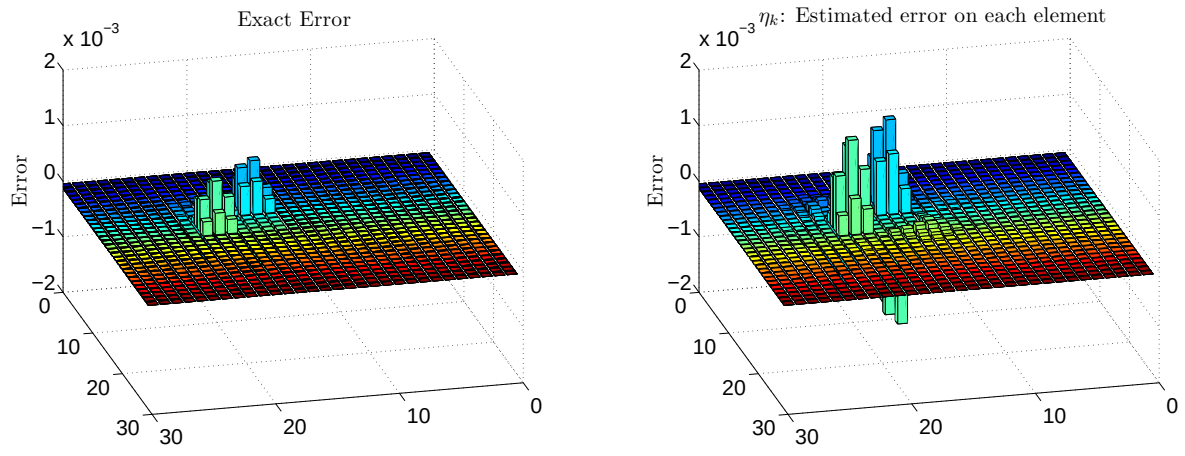

(a) (b)

Figure 4.32: Exact and estimated error over each element for 900 elements.

Trial Case 9:

The third and final example is also discussed in [36] and [31] and involves the same primal problem as in the previous example. The right hand side of the dual problem in this case is:

$$g^0 = \begin{cases} e^{\frac{-1}{|((x-x_0)^2+(y-y_0)^2-\epsilon^2)|}}/C, & \text{if } \sqrt{(x-x_0)^2+(y-y_0)^2} \leqslant \epsilon, \\ 0, & \text{otherwise.} \end{cases} \tag{4.104}$$

where, $\epsilon = 0.3$, $C = 3.256676118052263 \cdot 10^{-7}$ so that the integral of g^0 is equal to 1, and x, $y = 1/2$. g^0 is depicted in Figure 4.33.

The results are shown in Figures 4.34, 4.35, and 4.36.
From Figure 4.34, it can be seen that after 196 elements λ_1 falls within 6% bound of 1 and converges to this value. The behavior of λ_2 is more irregular and it is not clear whether it is converging or diverging. Furthermore, it can be seen that the error bounds correctly bound the exact and estimated error in the target functional and approach zero as these quantities converge. Again, it can be predicted that if the error bounds continue to converge towards zero, λ_2 will eventually converge.
Figure 4.35 shows the estimated and exact error for 100, 225, and 400 elements. It can be seen that the largest contributions to the global error are made by the elements that fall within an ϵ radius of the point x, $y = 1/2$. Figure 4.36 gives a 3D overview of the estimated and exact error for 900 elements.
The results from [31] are given in Table 4.2. These results have been obtained on sequences of locally refined meshes based on an error indicator similar to (4.91). It can be seen that there

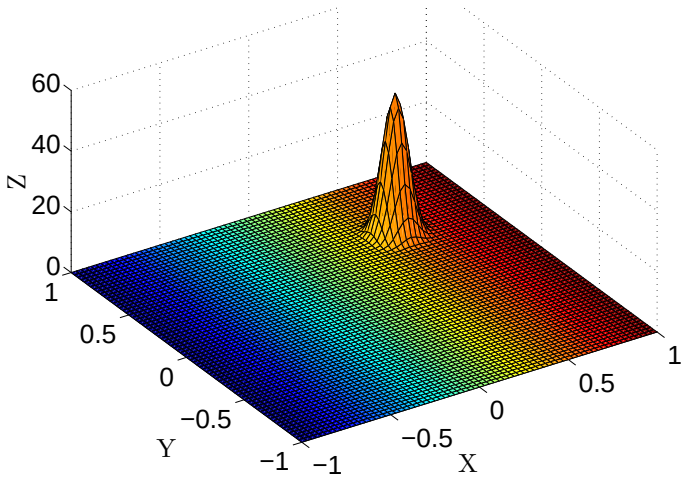

Figure 4.33: The right hand side of the dual problem.

are large disagreements between the values of λ_1 and $J(\phi - \phi_h)$ as presented in [31], and the results obtained from uniform refinement performed in this work. These discrepancies can be due to:

(1) Differences in the values of ϵ used in the two cases. Value of ϵ must be comparable to h otherwise detection of the point value will depend on the positioning of the nodes.

(2) Use of adaptive refinement as opposed to uniform refinement. However, it appears that this point would improve the results presented in [31] rather than deteriorate it.

(3) Differences in the construction of the error estimators. The error estimator presented in [31] is composed of element contributions which are made up of interior and element boundary terms. Therefore, this construction is slightly different from the error estimator given in (4.91).

(4) Fundamental differences in the numerical methods employed, ...

# Elements	$J(\phi - \phi_h)$	λ_1	# Elements	$J(\phi - \phi_h)$	λ_1	λ_2
81	$4.2 \cdot 10^{-1}$	0.17	81	$-1.7 \cdot 10^{-3}$	1.09	3.84
151	$1.4 \cdot 10^{-1}$	0.26	144	$-1.0 \cdot 10^{-3}$	0.71	2.01
635	$1.0 \cdot 10^{-2}$	0.30	625	$-8.8 \cdot 10^{-4}$	0.98	2.68
1443	$2.9 \cdot 10^{-3}$	0.39	1369	$-4.1 \cdot 10^{-4}$	0.99	2.86

Table 4.2: Effectivity of error indicator for the point error $J(\phi - \phi_h)$ as presented in [31], left, and, as obtained in the current work, right.

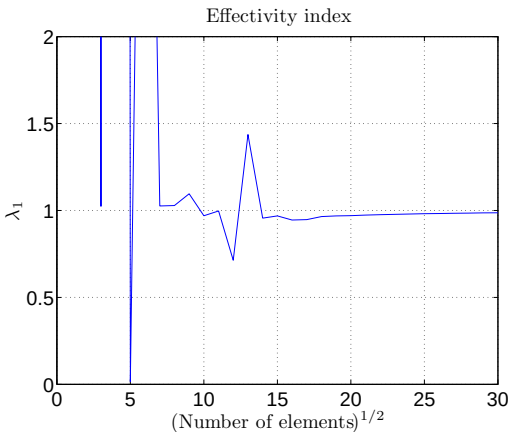

(a)

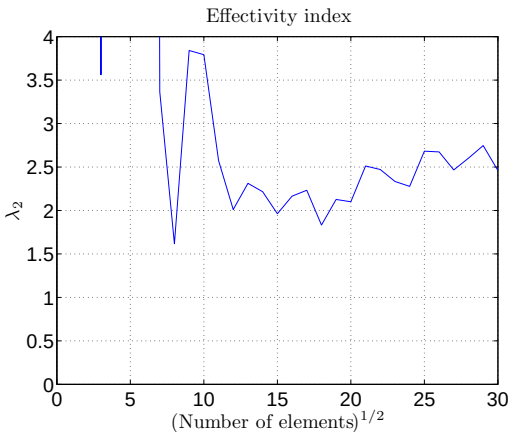

(b)

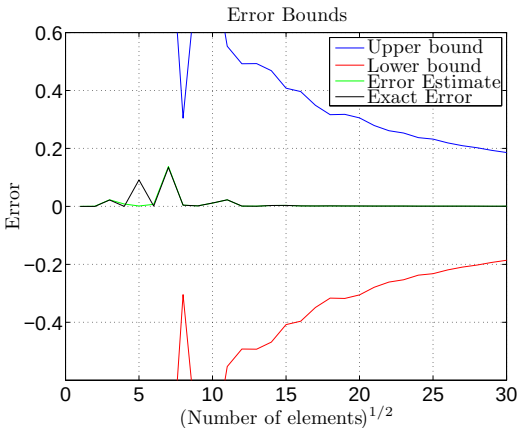

(c)

Figure 4.34: Effectivity indices and error bounds.

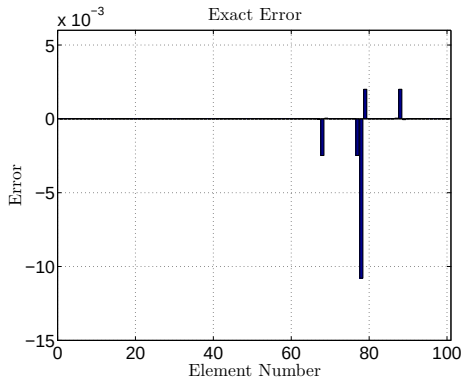

(a) Exact error over each element for 100 elements.

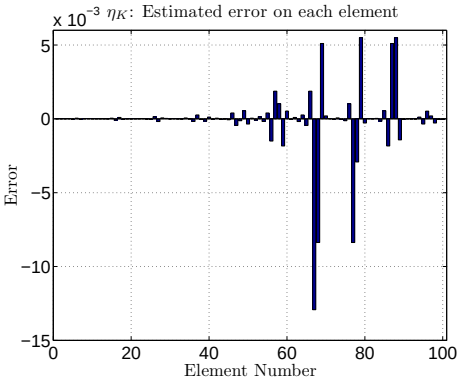

(b) Estimated error over each element for 100 elements.

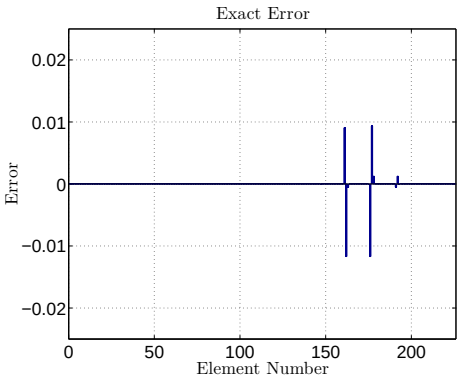

(c) Exact error over each element for 225 elements.

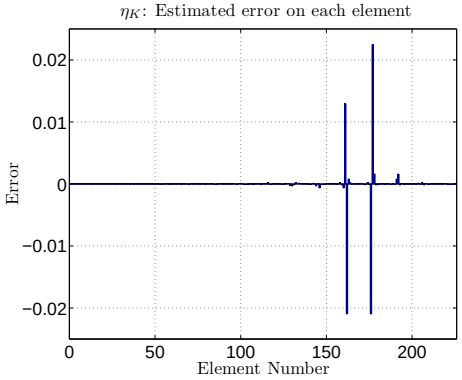

(d) Estimated error over each element for 225 elements.

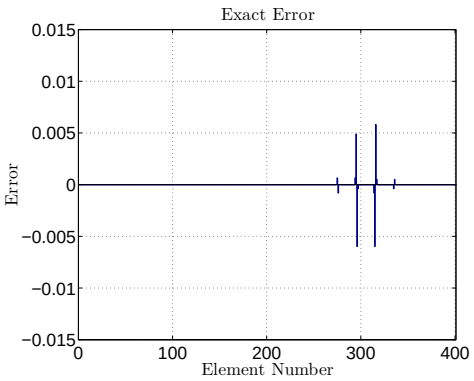

(e) Exact error over each element for 400 elements.

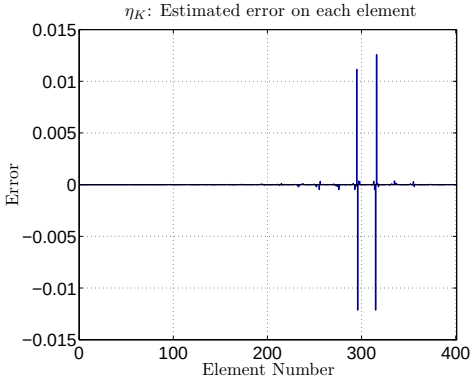

(f) Estimated error over each element for 400 elements.

Figure 4.35: Exact and estimated error for 100, 225, and 400 elements.

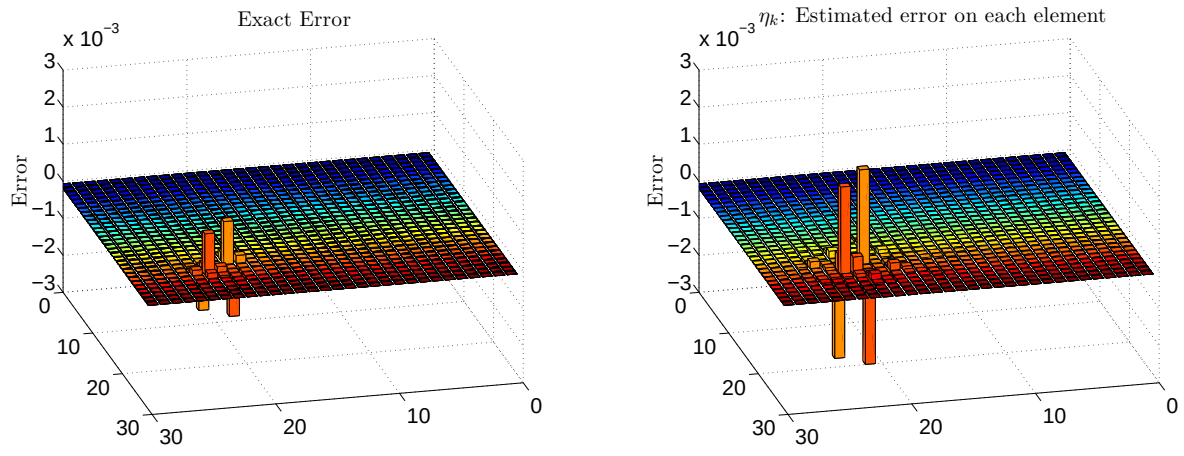

(a) (b)

Figure 4.36: Exact and estimated error over each element for 900 elements.

Chapter 5

Post-processing and Adjoint Recovery of Functionals

Until now, the focus of this work has been on the derivation of a dual weighted residual error estimator. This section is dedicated to a discussion on the improvements that can follow from the previous work if the estimated error on each element over the domain is taken into account. To this end, consider again the Poisson problem introduced in section 4.3.2:

$$\begin{cases} \star \mathrm{d} \star \mathrm{d}\phi^0 = f^0, & x \in \Omega, \\ \phi^0 = 0, & x \in \partial\Omega, \end{cases} \tag{5.1}$$

and the functional of interest,

$$J(\phi^0) = \int_\Omega g^0 \wedge \star\phi^0. \tag{5.2}$$

The dual problem to (5.1) is:

$$\begin{cases} \star \mathrm{d} \star \mathrm{d}\psi^0 = g^0, & x \in \Omega, \\ \psi^0 = 0, & x \in \partial\Omega. \end{cases} \tag{5.3}$$

Following the work of Niles and Pierce [37] the expression of the exact functional can be dissected as follows:

$$\left(g^0, \phi^0\right) = \left(g^0, \phi_h^0\right) - \left(\star \mathrm{d} \star \mathrm{d}\psi_h^0, \phi_h^0 - \phi^0\right) + \left(\star \mathrm{d} \star \mathrm{d}\psi_h^0 - g^0, \phi_h^0 - \phi^0\right). \tag{5.4}$$

Using integration by parts in the second expression on the right hand side yields:

$$\left(g^0, \phi^0\right) = \left(g^0, \phi_h^0\right) - \left(\psi_h^0, \star \mathrm{d} \star \mathrm{d}\phi_h^0 - f^0\right) + \left(\star \mathrm{d} \star \mathrm{d}\psi_h^0 - g^0, \phi_h^0 - \phi^0\right), \tag{5.5}$$

or yet,

$$\left(g^0, \phi^0\right) = \left(g^0, \phi_h^0\right) + \left(\mathrm{d}\psi_h^0, \mathrm{d}\phi_h^0\right) + \left(\psi_h^0, f^0\right) + \left(\star \mathrm{d} \star \mathrm{d}\psi_h^0 - g^0, \phi_h^0 - \phi^0\right). \tag{5.6}$$

The second and third expressions on the right hand side are the expressions of the familiar Poisson problem and can be written as:

$$\left(\mathrm{d}\psi_h^0, \mathrm{d}\phi_h^0\right) + \left(\psi_h^0, f^0\right) = \left(\mathrm{d}\psi_h^0, \mathrm{d}\phi_h^0 - \mathrm{d}\phi^0\right). \tag{5.7}$$

In order to construct a bound for (5.7), let $B(a^p, b^p)$ be a continuous and coercive bilinear form corresponding to the Poisson problem with $a^p, b^p \in H_0\Lambda^p(\Omega)$. Then:

$$|B(a^p, b^p)| \leqslant M \|a^p\|_{H_0\Lambda^p(\Omega)} \|b^p\|_{H_0\Lambda^p(\Omega)} \;\; \forall\, a^p, b^p \in H_0\Lambda^p(\Omega), \tag{5.8}$$

and,

$$B(a^p, a^p) \geqslant \alpha \|a^p\|^2_{H_0\Lambda^p(\Omega)} \;\; \forall\, a^p \in H_0\Lambda^p(\Omega), \tag{5.9}$$

where, M and α are constants independent of a^p. (5.8), and, (5.9) can then be used to write [38]:

$$C_1 \|a^p\|_{H_0\Lambda^p(\Omega)} \leqslant B(a^p, a^p)^{1/2} \leqslant C_2 \|a^p\|_{H_0\Lambda^p(\Omega)}, \tag{5.10}$$

where, C_1 and C_2 are constants independent of a^p, interpolation order, and discretization, and $B(a^p, a^p)^{1/2} = \|\mathrm{d}a^p\|_{L^2\Lambda^p(\Omega)}$. Therefore, the seminorm is equivalent to the $H_0\Lambda^p(\Omega)$-norm [38] [1].
The functional form of problem (5.1) can be written as:

$$-\left(\mathrm{d}\psi_h^0, \mathrm{d}\phi_h^0\right) = \left(\psi_h^0, f^0\right), \;\; \forall \psi_h^0 \in \Lambda_h^0(\Omega). \tag{5.11}$$

[1] This result could also be derived from Poincaré inequality, see [4].

Following Cea's Lemma, the interpolation error bounds the solution of the weak formulation and one has:

$$\|\phi^0 - \phi_h^0\|_{H_0\Lambda^0(\Omega)} \leqslant Ch^{l-1}|\phi^0|_{H_0^m\Lambda^0(\Omega)}, \quad \text{where, } l = \min(P+1, m), \tag{5.12}$$

where, C is a stability and interpolation constant and P is the number of interpolation points [4]. A similar result can be written for the dual solution. Moreover, following the equivalence of the seminorm and $H_0\Lambda^p(\Omega)$-norm one has:

$$\|\mathrm{d}(\phi^0 - \phi_h^0)\|_{L^2\Lambda^0(\Omega)} \leqslant Ch^{l-1}|\phi^0|_{H_0^m\Lambda^0(\Omega)}, \quad \text{where, } l = \min(P+1, m). \tag{5.13}$$

Returning to (5.7) and employing Cauchy-Schwarz inequality yields:

$$|\left(\mathrm{d}\psi_h^0, \mathrm{d}\phi_h^0 - \mathrm{d}\phi^0\right)| \leqslant \|\mathrm{d}\psi_h^0\|_{L^2\Lambda^0(\Omega)}\|\mathrm{d}\phi_h^0 - \mathrm{d}\phi^0\|_{L^2\Lambda^0(\Omega)}. \tag{5.14}$$

Inserting (5.13) in (5.14) yields:

$$|\left(\mathrm{d}\psi_h^0, \mathrm{d}\phi_h^0 - \mathrm{d}\phi^0\right)| \leqslant Ch^{l-1}\|\mathrm{d}\psi_h^0\|_{L^2\Lambda^0(\Omega)}|\phi^0|_{H_0^m\Lambda^0(\Omega)}, \quad \text{where, } l = \min(P+1, m). \tag{5.15}$$

(5.15) states that if the solution of the primal problem is analytic, then (5.7) has an exponential convergence towards zero.

Once again returning to (5.6) and employing Galerkin orthogonality yields:

$$\left(g^0, \phi^0\right) = \left(g^0, \phi_h^0\right) + \left(\mathrm{d}\psi_h^0 - \mathrm{d}\Pi_h\psi^0, \mathrm{d}\phi_h^0\right) + \left(\psi_h^0 - \Pi_h\psi^0, f^0\right) + \left(\star\mathrm{d}\star\,\mathrm{d}\psi_h^0 - g^0, \phi_h^0 - \phi^0\right). \tag{5.16}$$

The second and third expressions on the right hand side can now be recognized as the error estimate for the target functional introduced in section 4.3.2. Note that in order to obtain (5.16) one can add the expression for the error estimate,

$$\begin{aligned} J(\phi^0) - J(\phi_h^0) &= \left(\mathrm{d}\psi_h^0 - \mathrm{d}\Pi_h\psi^0, \mathrm{d}\phi_h^0\right) + \left(\psi_h^0 - \Pi_h\psi^0, f^0\right) = \dots \\ \dots &= \left(\mathrm{d}\psi_h^0 - \mathrm{d}\Pi_h\psi^0, \mathrm{d}\phi_h^0 - \mathrm{d}\phi^0\right), \end{aligned} \tag{5.17}$$

to the both sides of equation (5.6), reformulated in the following form:

$$\left(g^0, \phi_h^0\right) = \left(g^0, \phi^0\right) - \left(\mathrm{d}\psi_h^0, \mathrm{d}\phi_h^0\right) - \left(\psi_h^0, f^0\right) - \left(\star\mathrm{d}\star\,\mathrm{d}\psi_h^0 - g^0, \phi_h^0 - \phi^0\right). \tag{5.18}$$

This operation yields:

$$\left(g^0, \phi_h^0\right) = \left(g^0, \phi^0\right) - \left(\mathrm{d}(\psi_h^0 - \Pi_h\psi^0), \mathrm{d}\phi_h^0\right) - \left(\psi_h^0 - \Pi_h\psi^0, f^0\right) - \left(\star\mathrm{d}\star\,\mathrm{d}\psi_h^0 - g^0, \phi_h^0 - \phi^0\right). \tag{5.19}$$

In other words, addition of the error estimate to the approximate target functional in (5.18) results in a new approximation for the target functional which is given in (5.19).
In order to obtain a bound on (5.17), again Cauchy-Schwarz inequality can be used to write:

$$\left|\left(\mathrm{d}\psi_h^0 - \mathrm{d}\Pi_h\psi^0, \mathrm{d}\phi_h^0 - \mathrm{d}\phi^0\right)\right| \leqslant \|\mathrm{d}\psi_h^0 - \mathrm{d}\Pi_h\psi^0\|_{L^2\Lambda^0(\Omega)}\|\mathrm{d}\phi_h^0 - \mathrm{d}\phi^0\|_{L^2\Lambda^0(\Omega)}. \tag{5.20}$$

Moreover, employing triangle inequality on the first term on the right hand side yields:

$$\|\mathrm{d}\psi_h^0 - \mathrm{d}\Pi_h\psi^0\|_{L^2\Lambda^0(\Omega)} \leqslant \|\mathrm{d}(\psi_h^0 - \psi^0)\|_{L^2\Lambda^0(\Omega)} + \|\mathrm{d}(\psi^0 - \Pi_h\psi^0)\|_{L^2\Lambda^0(\Omega)}. \tag{5.21}$$

Inserting (5.21) in (5.20) gives:

$$\begin{aligned}\left|\left(\mathrm{d}\psi_h^0 - \mathrm{d}\Pi_h\psi^0, \mathrm{d}\phi_h^0 - \mathrm{d}\phi^0\right)\right| \;&\leqslant\; \left(\|\mathrm{d}(\psi_h^0 - \psi^0)\|_{L^2\Lambda^0(\Omega)} + \ldots\right.\\ &\ldots \;+\; \left.\|\mathrm{d}(\psi^0 - \Pi_h\psi^0)\|_{L^2\Lambda^0(\Omega)}\right)\|\mathrm{d}\phi_h^0 - \mathrm{d}\phi^0\|_{L^2\Lambda^0(\Omega)}.\end{aligned} \tag{5.22}$$

Assuming $\mathrm{d}(\phi_h^0 - \phi^0)$ and $\mathrm{d}(\psi^0 - \Pi_h\psi^0)$ are of the same orders of magnitude yields:

$$\begin{aligned}\left|\left(\mathrm{d}\psi_h^0 - \mathrm{d}\Pi_h\psi^0, \mathrm{d}\phi_h^0 - \mathrm{d}\phi^0\right)\right| \;&\leqslant\; Ch^{2(l-1)}\left(|\psi^0|_{H_0^m\Lambda^0(\Omega)} + \ldots\right.\\ &\ldots \;+\; \left.h|\psi^0|_{H_0^{m+1}\Lambda^0(\Omega)}\right)|\phi^0|_{H_0^m\Lambda^0(\Omega)},\end{aligned} \tag{5.23}$$

where, $l = \min(P+1, m)$.
Comparing (5.15) and (5.23) shows that the bound on (5.17) is tighter than the bound on (5.7). However, this says nothing about whether or not (5.17) is smaller than (5.7). To prove this, consider again expressions (5.17) and (5.7) repeated below,

$$| \left(\mathrm{d}\psi_h^0, \mathrm{d}\phi_h^0 - \mathrm{d}\phi^0\right) |, \tag{5.24}$$

$$| \left(\mathrm{d}\psi_h^0 - \mathrm{d}\Pi_h\psi^0, \mathrm{d}\phi_h^0 - \mathrm{d}\phi^0\right) |. \tag{5.25}$$

It can be seen that the term $\mathrm{d}\phi_h^0 - \mathrm{d}\phi^0$ is repeated in both expressions. Therefore, for (5.25) to be smaller than (5.24), a sufficient condition is to have $\Pi_h\psi^0$ as the orthogonal projection of ψ_h^0 on each element. This condition is not necessary. The overall contribution of the term $\left(\mathrm{d}\Pi_h\psi^0, \mathrm{d}\phi_h^0 - \mathrm{d}\phi^0\right)$ is zero due to Galerkin orthogonality. However, over each element this term is not zero. If $\Pi_h\psi^0$ is an orthogonal projection of ψ_h^0 on each element then it is ensured that:

$$| \left(\mathrm{d}\psi_h^0 - \mathrm{d}\Pi_h\psi^0, \mathrm{d}\phi_h^0 - \mathrm{d}\phi^0\right)_K | \leqslant | \left(\mathrm{d}\psi_h^0, \mathrm{d}\phi_h^0 - \mathrm{d}\phi^0\right)_K |. \tag{5.26}$$

where, K is the element number.
If orthogonality condition is not imposed and one chooses mimetic projection of ψ_h^0 instead, then, triangle inequality gives:

$$| \left(\mathrm{d}\psi_h^0 - \mathrm{d}\pi_h\psi^0, \mathrm{d}\phi_h^0 - \mathrm{d}\phi^0\right) | \leqslant | \left(\mathrm{d}\psi_h^0, \mathrm{d}\phi_h^0 - \mathrm{d}\phi^0\right) | + | \left(\mathrm{d}\pi\psi_h^0, \mathrm{d}\phi^0 - \mathrm{d}\phi_h^0\right) |, \tag{5.27}$$

where, the last term on the right hand side vanishes due to Galerkin orthogonality. This yields:

$$| \left(\mathrm{d}\psi_h^0 - \mathrm{d}\pi_h\psi^0, \mathrm{d}\phi_h^0 - \mathrm{d}\phi^0\right) | \leqslant | \left(\mathrm{d}\psi_h^0, \mathrm{d}\phi_h^0 - \mathrm{d}\phi^0\right) |. \tag{5.28}$$

(5.28) ensures faster convergence over the whole domain, but not over each element. It might be the case that good convergence rates can be obtained if Galerkin orthogonality holds on each individual element as well as over the whole domain.
Finally, to show that (5.19) is a better approximation for the target functional than (5.18), (5.24) and (5.25) must be the dominant terms in these expressions.

Following the same procedure as before, the following bound can be constructed for $\left(\star \mathrm{d} \star \mathrm{d}\psi_h^0 - g^0, \phi_h^0 - \phi^0\right)$.

$$\begin{aligned} & | \left(\star \mathrm{d} \star \mathrm{d}\psi_h^0 - g^0, \phi_h^0 - \phi^0\right) | = | \left(\mathrm{d}\psi^0 - \mathrm{d}\psi_h^0, \mathrm{d}\phi_h^0 - \mathrm{d}\phi^0\right) | \leqslant \dots \\ \dots \quad \leqslant \quad & C h^{(2l-1)} |\psi^0|_{H_0^{m+1}\Lambda^0(\Omega)} |\phi^0|_{H_0^m \Lambda^0(\Omega)}, \quad \text{where, } l = \min(P+1, m). \end{aligned} \tag{5.29}$$

Assuming $\left(\star \mathrm{d} \star \mathrm{d}\psi_h^0 - g^0, \phi_h^0 - \phi^0\right)$ is not the dominant term in either (5.24) or (5.25), (5.19) is a better approximation for the target functional than (5.18).
It is important to note that if the approximated value of the target functional is improved by adding the calculated value of the error estimator, the estimated error can no longer provide a quantitative approximation for the error in the value of the target functional.
To illustrate these results consider the following primal and dual problems:

$$\text{Primal problem} \quad \begin{cases} \star \mathrm{d} \star \mathrm{d}\phi^0 = \cos(2\pi x), & x \in \Omega, \\ \phi^0 = 0, & x \in \partial\Omega. \end{cases} \tag{5.30}$$

$$\text{Dual problem} \quad \begin{cases} \star \mathrm{d} \star \mathrm{d}\psi^0 = \cos(2\pi x), & x \in \Omega, \\ \psi^0 = 0, & x \in \partial\Omega. \end{cases} \tag{5.31}$$

Following what has been discussed thus far, in order to acquire a better approximation for the target functional (5.2), the error estimate as obtained in section 4.3.2 is used. Moreover, quadratic polynomials are considered for the reconstruction of the solution. The result is shown in Figure 5.1.
It can be seen that the error bound (5.23) correctly predicts the slope of the corrected functional. (5.15) on the other hand is not a tight bound and under predicts the convergence slope of the uncorrected functional. Moreover, it can be seen that (5.19) is indeed a better approximation for the target functional than (5.18).

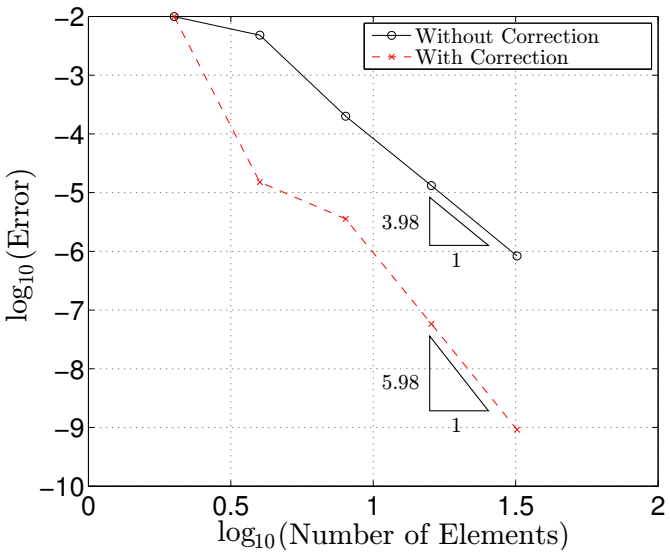

Figure 5.1: Error in the target functional with and without correction.

Chapter 6

Conclusions and Recommendations

In this chapter some concluding remarks regarding the work presented will be given. This will be followed by some recommendations for future work on this topic.

6.1 Conclusion

Accurate *a posteriori* error estimates are highly important in todays competitive world and are a major focus of research. The information provided by these estimates can be used for the construction of efficient adaptive mesh refinement algorithms. These algorithms can in turn be used to minimize the cost of reaching a given accuracy or to produce the most accurate solution for a given cost.
In this area, dual weighted residual error estimators offer reliable and accurate estimates for the error in the specific functionals of interest. There is a great body of knowledge on this topic which encompasses different numerical methods. As part of the on going research, the current work investigated the implementation, applicability, and advantages of dual weighted residual technique from the perspective of mimetic spectral element methods. In so doing, the already established foundation of DWR has been adopted from finite element methods and introduced into the mimetic framework.
In the current work a theoretical basis for the dual weighted residual technique was established in the language of differential geometry. It was shown that an error estimate based on DWR comprises of two parts, namely, the residual, and a weight. Derivation of the correct weight is achieved by solving an inhomogeneous adjoint p.d.e with certain boundary conditions relative to the functional of interest. Construction of this adjoint p.d.e is straight forward and was discussed for standard as well as mixed formulation of sample Poisson problems. A variety of test cases in 1D and 2D were investigated and it was shown that even for low numbers of elements, highly accurate estimates can be obtained. However, since these accurate estimates are acquired at the cost of solving a dual problem, they can be costly from the industry point of view. This can specially be the case if the dual solution is solved on a globally refined

mesh or using a higher order scheme with respect to the primal equation. A better way of addressing this problem is by approximation through higher order interpolation, where, the dual problem is solve on a coarser grid as the primal one but with higher order interpolants. Another limiting feature of DWR in the context of the current work is its incapability in dealing with discontinuities. This shortcoming is a result of employing Lagrange polynomials as the main reconstruction and integration tool and can perhaps be rectified by employing Splines.
Finally, it was shown that the estimated error obtained from the DWR method can be used to greatly improve the approximated values of the functionals of interest. However, if this improvement is made, the estimated error can no longer provide a quantitative approximation of the error in the value of the target functional.

6.2 Recommendations

Due to the novelty of the mimetic methods there is a lot to be done in this field. It is clear that many of the future endevours in this field will directly or indirectly affect the current work. Yet, it might be beneficial to list some of the most important improvements that can be made from the perspective of the current work. These ideas are listed below:

(1) The matrix corresponding to the discrete hodge can be a full matrix. This is due to the fact that Lagrange polynomials do not decay to zero in the region of their corresponding nodes (do not have finite support). Therefore, functions which possess this attribute can reduce the computational resources and hence be beneficial from industry point of view.

(2) Whenever a discontinuous function is interpolated with smooth functions, Gibb's phenomenon makes an appearance. Due to the local nature of this phenomenon, using low order polynomials in the regions of discontinuity is recommended. When the region of discontinuity is known, this can be achieved by employing a mortar method. Moreover, due to their piecewise definition, splines might be a better choice for controlling Gibb's phenomenon than Lagrange polynomials. More research on this area can shed new light on the Gibb's phenomenon and extend the current work to the discontinuous realm.

(3) The framework introduced in this thesis can be expanded to encompass nonlinear problems. This can be done by linearizing the bilinear form and the functional of interest.

(4) Since a refinement strategy using mortar method has already been developed for mimetic spectral element methods, in order to guide and automate the procedure of reducing the error in a functional of interest, a mesh adaptation strategy must be developed. This strategy consists of a choice for the enrichment (h/p-refinement) and a stopping criterion and can be viewed as an optimization problem. Following the "Principle of Equidistribution" if the element contributions to the global error are roughly equal over the whole domain, the optimal mesh has been achieved. These ideas can be used to construct an automated mesh refinement strategy.

(5) In chapter 5 it was shown that good convergence over each element can be achieved by using orthogonal projection. As was discussed in section 4.3.4, the following equality seems to hold in 1D: $\mathrm{d}\pi_h\psi_h^0 = \Pi_h\mathrm{d}\psi_h^0$. However, this appears to not be the case in 2D. Therefore, more investigation concerning the nature of the projections used in 1D and 2D can be beneficial.

Bibliography

[1] H. Flanders. *Differential Forms with Applications to the Physical Sciences*. Dover Books on Mathematics. Dover Publications, 1989.

[2] Marc Gerritsma. An introduction to a compatible spectral discretization method. *Mechanics of Advanced Materials and Structures*, 19(1-3):48–67, 2012.

[3] T. Frankel. *The Geometry of Physics: An Introduction*. Cambridge University Press, 2003.

[4] J. Kreeft, A. Palha, and M. Gerritsma. Mimetic framework on curvilinear quadrilaterals of arbitrary order. *ArXiv e-prints*, nov 2011.

[5] Claudio Mattiussi. The finite volume, finite element, and finite difference methods as numerical methods for physical field problems, 2000.

[6] E. Tonti and Gruppo nazionale per la fisica matematica. *On the formal structure of physical theories*. Istituto de matematica, Politecnico, 1975.

[7] H. Satō. *Algebraic Topology: An Intuitive Approach*. Translations of Mathematical Monographs. American Mathematical Society, 1999.

[8] W. Fulton. *Algebraic Topology: A First Course*. Graduate Texts in Mathematics. Springer-Verlag, 1995.

[9] P. B. Bochev and J. M. Hyman. Principles of mimetic discretizations of differential operators. *IMA Volumes In Mathematics and its Applications*, 142:89, 2006.

[10] G. E. Karniadakis and S. J. Sherwin. *Spectral/hp Element Methods for CFD*. Numerical Mathematics and Scientific Computation. Oxford University Press, USA, 1999.

[11] Bouman M.P. Mimetic spectral element method for elliptic problems. Master's thesis, Delft University of Technology, Netherlands, February 2010.

[12] Marc Gerritsma. Edge functions for spectral element methods. In Jan S. Hesthaven and Einar M. Rønquist, editors, *Spectral and High Order Methods for Partial Differential Equations*, volume 76, chapter Lecture Notes in Computational Science and Engineering, pages 199–207. Springer Berlin Heidelberg, 2011.

[13] P. Hansbo K. Eriksson, D. Estep and C. Johnson. Introduction to adaptive methods for differential equations. *Acta Numerica*, 4:105–158, 1995.

[14] J. T. Oden and S. Prudhomme. Goal-oriented error estimation and adaptivity for the finite element method. *Computers & Mathematics with Applications*, 41(5–6):735–756, 2001.

[15] Roland Becker and Rolf Rannacher. A feed-back approach to error control in finite element methods: Basic analysis and examples. *East-West J. Numer. Math*, 4:237–264, 1996.

[16] Roland Becker and Rolf Rannacher. An optimal control approach to a posteriori error estimation in finite element methods. *Acta Numerica*, 10:1–102, 2001.

[17] Michael B. Giles and Endre Süli. Adjoint methods for pdes: a posteriori error analysis and postprocessing by duality. *Acta Numerica*, 11:145–236, 2002.

[18] M. B. Giles and N. A. Pierce. Adjoint equations in cfd: duality, boundary conditions and solution behaviour, 1997.

[19] I. Babuška and W. C. Rheinboldt. Error estimates for adaptive finite element computations. *SIAM Journal on Numerical Analysis*, 15(4):736–754, 1978.

[20] R. Verfürth. *A review of a posteriori error estimation and adaptive mesh-refinement techniques*. Advances in numerical mathematics. Wiley-Teubner, 1996.

[21] M. Ainsworth and J. T. Oden. *A Posteriori Error Estimation in Finite Element Analysis*. Pure and Applied Mathematics. John Wiley, 2000.

[22] Thomas Grätsch and Klaus-Jürgen Bathe. A posteriori error estimation techniques in practical finite element analysis. *Computers & Structures*, 83(4–5):235–265, 2005.

[23] I. Babuška and W. C. Rheinboldt. A-posteriori error estimates for the finite element method. *International Journal for Numerical Methods in Engineering*, 12(10):1597–1615, 1978.

[24] I. Babuska and W. C. Rheinboldt. Analysis of optimal finite-element meshes in r^1. *Mathematics of Computation*, 33(146):–435, 1979.

[25] Randolph E. Bank and ALAN WEISER. Some a posteriori error estimators for elliptic partial differential equations. *MATHEMATICS OF COMPUTATION*, 44:283–301, 1985.

[26] S. Prudhomme, F. Nobile, L. Chamoin, and J. T. Oden. Analysis of a subdomain-based error estimator for finite element approximations of elliptic problems. *Numerical Methods for Partial Differential Equations*, 20(2):165–192, 2004.

[27] O. C. Zienkiewicz and J. Z. Zhu. A simple error estimator and adaptive procedure for practical engineerng analysis. *International Journal for Numerical Methods in Engineering*, 24(2):337–357, 1987.

[28] I. Babuška and A. Miller. The post-processing approach in the finite element method–part 1: Calculation of displacements, stresses and other higher derivatives of the displacements. *International Journal for Numerical Methods in Engineering*, 20(6):1085–1109, 1984.

[29] Slimane Adjerid and Mohamed Salim. Even–odd goal-oriented a posteriori error estimation for elliptic problems. *Appl. Numer. Math.*, 55(4):384–402, dec 2005.

[30] S. Prudhomme and J. T. Oden. On goal-oriented error estimation for elliptic problems: application to the control of pointwise errors. *Computer Methods in Applied Mechanics and Engineering*, 176(1–4):313–331, 1999.

[31] W. Bangerth and R. Rannacher. *Adaptive Finite Element Methods for Differential Equations*. Lectures in Mathematics. Birkhäuser Verlag, 2003.

[32] Douglas N. Arnold, Richard S. Falk, and Ragnar Winther. Finite element exterior calculus: from hodge theory to numerical stability. *Bull. Amer. Math. Soc. (N.S.)*, 47:281–354, 2010. DOI 10.1090/S0273-0979-10-01278-4.

[33] Jasper J. Kreeft and Marc I. Gerritsma. A priori error estimates for compatible spectral discretization of the stokes problem for all admissible boundary conditions. *CoRR*, abs/1206.2812, 2012.

[34] A. Demlow and A. N. Hirani. A posteriori error estimates for finite element exterior calculus: The de rham complex. *ArXiv e-prints*, mar 2012.

[35] R. Haberman. *Applied Partial Differential Equations: With Fourier Series and Boundary Value Problems*. Pearson Prentice Hall, 2004.

[36] T. Richter. *Funktionalorientierte Gitteroptimierung bei der Finite-Element-Approximation elliptischer Differentialgleichungen.* PhD thesis, University of Heidelberg, Institute of Applied Mathematics, 2001.

[37] Niles A. Pierce and Michael B. Giles. Adjoint recovery of superconvergent functionals from pde approximations. *SIAM Rev*, 42:247–264, 1998.

[38] Klaus-Jurgen Bathe. *Finite Element Procedures*. Prentice Hall, 1st edition, jun 1995.

Appendix A

Consider the following pointwise inner product on a Riemanian n-manifold Ω,

$$\langle a^p, b^p \rangle = \sum_{i_1,j_1}^{i_p,j_p} g^{IJ} a_I b_J = a \underset{\rightarrow}{}_I b^I, \tag{A.1}$$

where, $g^{IJ} = \langle \mathrm{d}x^I, \mathrm{d}x^J \rangle$, is the inverse of the metric tensor, $g_{IJ} = \langle \frac{\partial}{\partial x^I}, \frac{\partial}{\partial x^J} \rangle$. $\frac{\partial}{\partial x^I}$ and $\mathrm{d}x^I$ are the basis vectors of the space tangent to Ω and its corresponding dual space, respectively. $I = (i_1, ..., i_p)$, and $J = (j_1, ..., j_p)$, and $\underset{\rightarrow}{}$ signifies that $i_1 < i_2 < ... < i_p$. The repeated lower-upper indices imply Einstein summation convention:

$$a^i_i = \sum_i a^i_i. \tag{A.2}$$

Moreover, consider the space of square integrable p-forms equipped with inner product,

$$(a^p, b^p) = \int_\Omega \langle a^p, b^p \rangle \, \omega^n, \tag{A.3}$$

and norm,

$$\|a^p\|_{L^2\Lambda^p(\Omega)} = \left(\int_\Omega \langle a^p, a^p \rangle \, \omega^n \right)^{1/2}, \tag{A.4}$$

where ω^n is the volume form. It is required from the Hodge-$\star$ operator to associate an (n-p)-form to the contravariant version of a p-form. This is done through contraction or interior

product of the volume form with the contravariant version of a p-form.
For a zero-form, $a^0 = 1$, this operation yields:

$$\star 1 = \sqrt{|g|}\epsilon_{12..n}\mathrm{d}x^1 \wedge \mathrm{d}x^1 ... \wedge \mathrm{d}x^n = \omega^n. \tag{A.5}$$

where $|g|$ is the Jacobian of the metric tensor and $\epsilon_{12..n}$ signifies the permutation of $\mathrm{d}x^1 \wedge \mathrm{d}x^1 ... \wedge \mathrm{d}x^n$. For odd permutations $\epsilon = -1$, for even permutations $\epsilon = 1$, and otherwise $\epsilon = 0$. The action of the Hodge-$\star$ on a p-form can be defined as:

$$\star a^p := a^*_{\underset{\rightarrow}{J}}\mathrm{d}x^J, \tag{A.6}$$

where,

$$a^*_{\underset{\rightarrow}{J}} := \sqrt{|g|}\, a^K\, \epsilon_{\underset{\rightarrow}{K}\,\underset{\rightarrow}{J}}. \tag{A.7}$$

with $\{J = (j_1, ..., j_{n-p}) : j_1 < j_2 < ... < j_{n-p}\}$, and $\{K = (k_1, ..., k_p) : k_1 < k_2 < ... < k_p\}$.
Following the definition of wedge product and the determinant of a matrix one has:

$$a^p \wedge \star b^p = (a \wedge \star b)_{1,2,...,n}\mathrm{d}x^1 \wedge \cdots \wedge \mathrm{d}x^n, \tag{A.8}$$

where,

$$(a \wedge \star b)_{1,2,...,n} = \epsilon^{JK} a_{\underset{\rightarrow}{J}} (\star b)_{\underset{\rightarrow}{K}} = \epsilon^{JK} a_{\underset{\rightarrow}{J}} \sqrt{|g|}\, b^L\, \epsilon_{\underset{\rightarrow}{L}\,\underset{\rightarrow}{K}} = \sqrt{|g|}\, a_{\underset{\rightarrow}{J}} b^J. \tag{A.9}$$

Using (A.1) yields:

$$a^p \wedge \star b^p = \langle a^p, b^p \rangle \omega^n \quad \Rightarrow \quad \int_\Omega a^p \wedge \star b^p = \int_\Omega \langle a^p, b^p \rangle \omega^n = (a^p, b^p)\,. \tag{A.10}$$

For a more thorough treatment of these concepts see [3]. In the following example, (A.6) and (A.7) will be used to perform Hodge-$\star$ on a one-form in $\mathbb{R}^2$.

Example: Let a^1 be a one-form in $\mathbb{R}^2$. Then:

$$a^1 = a\ \mathrm{d}x + b\ \mathrm{d}y \tag{A.11}$$

and,

$$\star a^1 = a\ \star \mathrm{d}x + b\ \star \mathrm{d}y = \sqrt{|g|}\ a\ \epsilon_{1,2}\ \mathrm{d}y + \sqrt{|g|}\ b\ \epsilon_{2,1}\ \mathrm{d}x, \tag{A.12}$$

where, $\sqrt{|g|} = 1$, $\epsilon_{1,2} = 1$, and $\epsilon_{2,1} = -1$, which yields:

$$\star a^1 = a\ \mathrm{d}y - b\ \mathrm{d}x. \tag{A.13}$$

Appendix B

Let f and g be smooth functions in Ω and let a^p and $b^p \in \Lambda^p(\Omega)$. Then the Hodge-$\star$ operator satisfies the following relations [4]:

$$\begin{aligned}
\star\left(fa^p + gb^p\right) &= f\star a^p + g\star b^p, && \text{(B.1)}\\
\star\star a^p &= (-1)^{p(n-p)}a^p, && \text{(B.2)}\\
a^p \wedge \star b^p &= b^p \wedge \star a^p = \langle a^p, b^p\rangle\omega^n, && \text{(B.3)}\\
\star\left(a^p \wedge \star b^p\right) &= \star\left(b^p \wedge \star a^p\right) = \langle a^p, b^p\rangle, && \text{(B.4)}\\
(\star a^p, \star b^p) &= (a^p, b^p)\,. && \text{(B.5)}
\end{aligned}$$

The three last relations are proven as follows:

Proof 1:

$$\begin{aligned}
a^p \wedge \star b^p \overset{(A.10)}{=} \langle a^p, b^p\rangle\omega^n \quad &\Rightarrow \quad \int_\Omega a^p \wedge \star b^p = \int_\Omega \langle a^p, b^p\rangle\omega^n \overset{(A.3)}{=} (a^p, b^p) = (b^p, a^p) = \dots\\
\cdots = \int_\Omega \langle b^p, a^p\rangle\omega^n \quad &= \quad \int_\Omega b^p \wedge \star a^p \Rightarrow \int_\Omega a^p \wedge \star b^p = \int_\Omega b^p \wedge \star a^p. \qquad \text{(B.6)}
\end{aligned}$$

Since the domain, Ω, is chosen arbitrarily, one has:

$$\int_\Omega a^p \wedge \star b^p = \int_\Omega b^p \wedge \star a^p \quad \Rightarrow \quad a^p \wedge \star b^p = b^p \wedge \star a^p. \qquad \text{(B.7)}$$

Proof 2: Proof of relation (B.4) follows directly from the previous result. Note that in the last expression in (B.3), performing Hodge-$\star$ on the volume form results in 1.

Proof 3:

$$(\star a^p, \star b^p) \overset{(A.10)}{=} \int_\Omega \star a^p \wedge \star\star\, b^p \overset{(B.2)}{=} (-1)^{p(n-p)} \int_\Omega \star a^p \wedge b^p = (-1)^{2p(n-p)} \int_\Omega b^p \wedge \star a^p \tag{B.8}$$

Since $2p(n-p)$ is always an even number, one has:

$$(\star a^p, \star b^p) = (a^p, b^p)\,. \tag{B.9}$$

Appendix C

Consider the following formulation of Poisson equation:

$$\begin{cases} \mathrm{d}^\star \mathrm{d}\phi^0 = f^0, & x \in \Omega, \\ \phi^0 = 0, & x \in \partial\Omega. \end{cases} \tag{C.1}$$

Using integration by parts, this problem can be posed in the variational form as: Find $\phi^0 \in H\Lambda^0(\Omega)$, where,

$$\begin{cases} -\langle \mathrm{d}\phi^0, \mathrm{d}h^0 \rangle = \langle f^0, h^0 \rangle, & x \in \Omega, \quad \forall \ h^0 \in H\Lambda^0(\Omega) \\ \phi^0 = 0, & x \in \partial\Omega, \end{cases} \tag{C.2}$$

It can be seen that integration by parts has transformed the metric dependent codifferential operator, $\mathrm{d}^\star$, into the metric free exterior derivative, d. This is the main purpose of performing integration by parts.
Now consider the following formulation of the Poisson equation:

$$\begin{cases} \mathrm{d}\mathrm{d}^\star \phi^1 = f^1, & x \in \Omega, \\ \star\phi^1 = 0, & x \in \partial\Omega. \end{cases} \tag{C.3}$$

Once again using integration by parts yields: Find $\phi^1 \in H\Lambda^1(\Omega)$, where,

$$\begin{cases} -\langle \star\mathrm{d}\star\phi^1, \star\mathrm{d}\star e^1 \rangle = \langle f^1, e^1 \rangle, & x \in \Omega, \quad \forall \ e^1 \in H\Lambda^1(\Omega) \\ \star\phi^1 = 0, & x \in \partial\Omega, \end{cases} \tag{C.4}$$

In this case it can be seen that not only the metric dependent codifferential operator does not vanish, the metric free exterior derivative is transformed into a codifferential operator.

Therefore, even more metric has been introduced into the equation. This renders equation (C.4) unsolvable.
The way to deal with this problem is to introduce an auxiliary variable, q^0, and pose problem (C.4) in the following format:

$$\begin{cases} \star \mathrm{d} \star \phi^1 = q^0, & x \in \Omega, \\ \mathrm{d}q^0 = f^1, & x \in \Omega, \\ \star \phi^1 = 0, & x \in \partial\Omega. \end{cases} \tag{C.5}$$

(C.5) can now be solved. However, unlike (C.3), (C.5) is no longer the dual of (C.1).
An important point to notice here is that one is not free to choose between a direct weak formulation or a mixed formulation. This choice is dictated by the geometry. A principle consequence of respecting the geometry for problems that are posed in mixed form is the stability that is obtained when solving these problems.

Appendix D

let,

$$\lambda_1 = \frac{|\sum_K \eta_K|}{|\sum_K \{\int_K (\star\phi^0 \wedge g^0) - (\star\phi_h^0 \wedge g^0)\}|}. \tag{D.1}$$

and,

$$\lambda_2 = \frac{\sum_K |\eta_K|}{\sum_K |\int_K (\star\phi^0 \wedge g^0) - (\star\phi_h^0 \wedge g^0)|}, \tag{D.2}$$

be effectivity indices. Following tables present some of the results obtained for the 1D trial cases discussed in sections (4.3) and (4.4).

Number of Elements	$J(\phi - \phi_h)$	$\lvert\sum \eta_K\rvert$	$\sum \lvert\eta_K\rvert$	λ_1	λ_2
4	-5.427e-003	5.266e-003	5.266e-003	9.704e-001	9.704e-001
9	-1.276e-004	1.270e-004	1.270e-004	9.953e-001	9.949e-001
13	-3.003e-005	2.997e-005	2.997e-005	9.977e-001	9.976e-001
18	-8.260e-006	8.251e-006	8.251e-006	9.988e-001	9.987e-001
23	-3.112e-006	3.110e-006	3.110e-006	9.992e-001	9.992e-001

Table D.1: Results for the case where $g^0 = f^0 = \cos(2\pi x)$.

Number of Elements	$J(\phi - \phi_h)$	$\lvert\sum \eta_K\rvert$	$\sum \lvert\eta_K\rvert$	λ_1	λ_2
4	-6.953e-008	1.150e-007	1.150e-007	1.654e+000	1.654e+000
9	-5.098e-008	5.549e-008	5.549e-008	1.088e+000	1.088e+000
13	-2.034e-008	2.070e-008	2.070e-008	1.017e+000	1.017e+000
18	-7.837e-009	7.847e-009	7.847e-009	1.001e+000	1.001e+000
23	-3.691e-009	3.690e-009	3.690e-009	9.995e-001	9.995e-001

Table D.2: Results of Trial Case 1.

Number of Elements	$J(\phi - \phi_h)$	$\lvert\sum \eta_K\rvert$	$\sum \lvert\eta_K\rvert$	λ_1	λ_2
4	1.646e-001	1.646e-001	1.673e-001	1.000e+000	1.000e+000
9	6.411e-003	6.254e-003	6.750e-003	9.755e-001	9.845e-001
13	1.175e-003	1.169e-003	1.696e-003	9.953e-001	9.900e-001
18	3.095e-004	3.095e-004	4.400e-004	1.000e+000	9.984e-001
23	1.158e-004	1.157e-004	1.624e-004	9.989e-001	9.949e-001

Table D.3: Results of Trial Case 2.

Number of Elements	$J(\phi - \phi_h)$	$\lvert\sum \eta_K\rvert$	$\sum \lvert\eta_K\rvert$	λ_1	λ_2
4	-3.377e-017	2.219e-018	6.938e-018	6.570e-002	4.116e-002
9	-1.367e-002	1.181e-002	2.189e-002	8.634e-001	9.655e-001
13	-1.090e-003	9.035e-004	1.148e-002	8.285e-001	9.636e-001
18	-1.559e-016	4.672e-017	6.246e-003	2.997e-001	9.811e-001
23	-7.958e-005	6.447e-005	4.018e-003	8.101e-001	9.636e-001

Table D.4: Results of Trial Case 3.

Number of Elements	$J(\phi - \phi_h)$	$\lvert\sum \eta_K\rvert$	$\sum \lvert\eta_K\rvert$	λ_2	λ_1
4	5.666e-003	5.648e-003	6.308e-003	9.969e-001	9.972e-001
9	1.802e-005	1.735e-005	3.709e-005	9.626e-001	1.015e+000
13	2.416e-006	2.378e-006	5.166e-006	9.845e-001	1.005e+000
18	3.731e-007	3.703e-007	6.959e-007	9.924e-001	1.001e+000
23	8.872e-008	8.832e-008	1.496e-007	9.955e-001	1.000e+000

Table D.5: Results of Trial Case 4.

Number of Elements	$J(\phi - \phi_h)$	$\lvert\sum \eta_K\rvert$	$\sum \lvert\eta_K\rvert$	λ_1	λ_2
4	1.435e-005	7.650e-006	7.650e-006	5.330e-001	5.330e-001
9	5.744e-007	6.284e-007	6.284e-007	1.094e+000	1.094e+000
13	1.305e-007	1.480e-007	1.480e-007	1.134e+000	1.134e+000
18	3.433e-008	3.900e-008	3.900e-008	1.136e+000	1.136e+000
23	1.229e-008	1.391e-008	1.391e-008	1.131e+000	1.131e+000

Table D.6: Results of Trial Case 5.

Number of Elements	$J(\phi - \phi_h)$	$\lvert\sum \eta_K\rvert$	$\sum \lvert\eta_K\rvert$	λ_1	λ_2
4	-6.762e-017	8.803e-017	1.574e-016	1.301e+000	7.840e-013
9	-6.587e-003	6.782e-003	6.782e-003	1.029e+000	1.001e+000
13	-6.889e-004	6.914e-004	2.186e-003	1.003e+000	1.001e+000
18	-1.992e-017	5.269e-017	5.168e-004	2.644e+000	1.002e+000
23	-5.754e-005	5.751e-005	2.649e-004	9.995e-001	1.001e+000

Table D.7: Results of Trial Case 6.